

ABSTRACT

HALBUR, SIMON. Assessment of Cooling Microelectronics using Piezoelectric Bimorphs.
(under the direction of Dr. Paul I. Ro)

As the heat generation of processors for notebook computers continues to increase, so does the need for smaller, more efficient cooling systems. The cooling capabilities of the piezoelectric bimorph were assessed to determine if it could fulfill this need. This was accomplished by first analyzing the current methods used to cool notebook computers using heat transfer theory. Using this data and the known properties of the cooling system, two techniques were applied to try and predict the temperature profile of a processor. By predicting this profile it would be possible to determine the amount of convective cooling required to dissipate the heat for a specific processor.

The cooling capabilities of the piezoelectric bimorph were assessed by looking at the theoretical volumetric flow rates and flow velocities it was able to produce through bulk air flow. It was found that the flow rate increases while the flow velocity decreases as the length of the bimorph increases. This was further supported by experimental testing with a heat source that could be regulated to output a specified amount of power. Testing also showed that there exists an optimal bimorph length and optimal gap between the bimorph and heat source, where maximum cooling is obtained.

By comparing the cooling requirements of a processor and the cooling capabilities of a piezoelectric bimorph it was found that the bimorph's capabilities are not sufficient for current high power microelectronics. Instead the bimorph was found to be comparable to a heat sink for an older Pentium® processor, which means the bimorph could be viable for low power devices.

**ASSESSMENT OF COOLING MICROELECTRONICS USING PIEZOELECTRIC
BIMORPHS**

by
SIMON GILBERT HALBUR

A thesis submitted to the Graduate Faculty of
North Carolina State University
in partial fulfillment of the
requirements for the Degree of
Master of Science

MECHANICAL ENGINEERING

Raleigh

2004

APPROVED BY:

Chair of Advisory Committee

To my parents

and a friend

BIOGRAPHY

Simon Halbur was born in Wisconsin in the summer of 1981. In May of 2003, he received his B.S. in Electromechanical Engineering at Loras College in Dubuque, Iowa. While at Loras, he performed research at the University of Texas at Arlington's Automation and Robotics Research Institute during the summer of 2002. In the fall of 2003, Simon began his studies towards a M.S. in Mechanical Engineering at North Carolina State University. Not long after, he began to work on his thesis under the advisement of Dr. Paul I. Ro.

ACKNOWLEDGEMENTS

I would like to thank first and foremost my advisor Dr. Paul I. Ro for his guidance and patience while I worked on my thesis. He was always open-minded when I presented new ideas even if they weren't the best.

I would also like to thank the members of the Precision Engineering Center whom had always been available and receptive to any questions I had.

Finally, I would like to thank my parents and a close friend for their support in all that I have done and will hopefully do.

TABLE OF CONTENTS

LIST OF TABLES	vii
LIST OF FIGURES	viii
1 INTRODUCTION	1
1.1 Motivation of Research.....	1
1.2 Current Notebook Cooling Methods.....	2
1.2.1 Remote Heat Exchanger (RHE).....	2
1.2.2 Metal-core Printed Circuit Boards and Stamped Plates.....	6
1.3 Acoustic Streaming.....	6
1.3.1 Convective Heat Transfer.....	8
1.4 Research Objectives.....	9
2 THEORETICAL ANALYSES	11
2.1 Heat Analysis of Dell® Inspiron™ Cooling System.....	11
2.1.1 System Identification.....	11
2.1.2 Analytical Heat Transfer Analysis.....	20
2.1.3 Ansys® Simulation.....	32
2.1.4 Intel® Thermal Dissipation Power (TDP) Ratings.....	35
2.1.5 Rate of Heat Transfer Comparison.....	36
2.2 Cooling Capabilities of Piezoelectric Bimorph.....	37
2.2.1 Physical Characteristics of Bimorphs.....	37
2.2.2 Bimorph Dynamic Response.....	40
2.2.3 Ansys® Verification of Response.....	46
2.2.4 Volumetric Flow Rate.....	53
2.2.5 Flow Velocity.....	56
3 TEMPERATURE PROFILE PREDICTION	61
3.1 Power Resistor System.....	61
3.2 Least Squares Approach.....	64
3.3 First Law of Thermodynamics.....	66
3.3.1 Conservation of Energy Theory.....	66
3.3.2 Temperature Profile Prediction of Power Resistor.....	69
3.3.3 Temperature Profile Prediction of Celeron® Processor.....	74
4 EXPERIMENTAL RESULTS	76
4.1 Power Resistor Cooling Experiments.....	76
4.1.1 Experimental Setup.....	76
4.1.2 Defining Optimal Gap.....	77
4.1.3 Defining Optimal Length.....	78

4.1.4 Flow Rate Comparison.....	81
4.2 Processor Cooling Experiments.....	82
4.2.1 Bimorph and Aluminum Plate.....	82
4.2.2 Bimorph and Inspiron™ Cooling System without Fan.....	85
4.3 Heat Sink vs. Bimorph Cooling Capabilities.....	86
4.3.1 Ansys® Simulation.....	86
4.3.2 Cooling Comparison between Heat Sink and Bimorph Results.....	90
5 CONCLUSIONS	92
5.1 Heat Analysis of Notebook Computer.....	92
5.2 Cooling Capabilities of Piezoelectric Bimorph.....	93
5.3 Future Work.....	94
REFERENCES	95

LIST OF TABLES

Table 2.1: Properties of Copper Plate	21
Table 2.2: Characteristics of Heat Sink	27
Table 2.3: Properties of Heat Pipe	33
Table 2.4: Ansys® vs. Analytical Rate of Heat Transfer	36
Table 2.5: Piezoelectric Bimorphs	38
Table 2.6: Properties of 5H4E Piezoceramic	38
Table 2.7: Properties of 5A4E Piezoceramic	39
Table 2.8: Properties of Composite Shim	39
Table 2.9: Properties of Stainless Steel Shim	39
Table 2.10: Properties of Bonding Layer	40
Table 3.1: Properties of Aluminum Plate	62
Table 3.2: Properties of Power Resistor	62
Table 3.3: Least Squares Constants	64

LIST OF FIGURES

Figure 1.1: Moore's Law	1
Figure 1.2: Remote Heat Exchanger Cooling System	2
Figure 1.3: Compaq Notebook Cooling System	3
Figure 1.4: Extruded Heat Sink	4
Figure 1.5: Folded Fin Heat Sink	4
Figure 1.6: Bonded/Fabricated Heat Sink	5
Figure 1.7: Heat Pipe	6
Figure 1.8: Rayleigh Streaming	7
Figure 1.9: Convective Cooling using Piezoelectric Bimorph	9
Figure 1.10: Convective Cooling using Slotted Piezoelectric Bimorph	9
Figure 2.1: Overall Layout of Inspiron™ Notebook	12
Figure 2.2: Dell® Inspiron™ Cooling System Closeup	13
Figure 2.3: Dell® Inspiron™ Cooling System Overview	13
Figure 2.4: Location of Temperature Thermocouples on Processor	14
Figure 2.5: Layout of Pentium® Processor	16
Figure 2.6: Flow Chart of 'Full Load' Program	16
Figure 2.7: Temperature of Celeron® Processor w/o Fan	17
Figure 2.8: Temperature of Celeron® Processor w/ Fan	18
Figure 2.9: Temperature of Copper Plate and Heat Sink w/o Fan	19
Figure 2.10: Temperature of Copper Plate and Heat Sink w/ Fan	19
Figure 2.11: Convection Coefficient for Copper Plate w/o Fan	24

Figure 2.12: Rate of Heat Transfer from Copper Plate w/o Fan	24
Figure 2.13: Convection Coefficient for Copper Plate w/ Fan	25
Figure 2.14: Rate of Heat Transfer from Copper Plate w/ Fan	25
Figure 2.15: Fin Efficiency Profile Plot	27
Figure 2.16: Reynold's Number for Forced Convection through Heat Sink	29
Figure 2.17: Rate of Heat Transfer from Heat Sink w/o Fan	29
Figure 2.18: Rate of Heat Transfer from Heat Sink w/ Fan	30
Figure 2.19: Rate of Heat Transfer during Processor Heating	31
Figure 2.20: Rate of Heat Transfer during Processor Cooling	31
Figure 2.21: Steady-state Temperature of Cooling System	33
Figure 2.22: Heat Flux through Copper Plate	34
Figure 2.23: Heat Flux through Heat Sink	34
Figure 2.24: Mobile Celeron® Thermal Dissipation Power Ratings	35
Figure 2.25: Layout of X-Poled Bimorph	38
Figure 2.26: Analytical First Modal Frequencies	41
Figure 2.27: Analytical Second Modal Frequencies	42
Figure 2.28: Frequency Response of Mechanical System	44
Figure 2.29: Dynamic Tip Deflection Flow Chart	44
Figure 2.30: Analytical First Mode Bimorph Tip Deflection	45
Figure 2.31: Analytical Second Mode Bimorph Amplitude	46
Figure 2.32: Ansys® Harmonic Response of Bimorph	47
Figure 2.33: Ansys® First Modal Frequency	48
Figure 2.34: Ansys® Second Modal Frequency	48

Figure 2.35: First Mode Bimorph Tip Deflection (+/-1V)	49
Figure 2.36: Second Mode Bimorph Amplitude (+/-1V)	50
Figure 2.37: Ansys® vs. Equation 2.2 First Mode Frequency Comparison	50
Figure 2.38: Ansys® vs. Equation 2.2 Second Mode Frequency Comparison	51
Figure 2.39: First Mode 5H Tip Deflection Comparison (+/- 1V)	52
Figure 2.40: Second Mode 5H Amplitude Comparison (+/-1V)	52
Figure 2.41: First Mode Shape of Free End Beam	54
Figure 2.42: Second Mode Shape of Free End Beam	54
Figure 2.43: First Mode Volumetric Flow Rate (+/-1V)	55
Figure 2.44: Second Mode Volumetric Flow Rate (+/-1V)	56
Figure 2.45: Minimum Exit Area for First Mode	57
Figure 2.46: Maximum Exit Area for First Mode	57
Figure 2.47: Minimum Exit Area for Second Mode	57
Figure 2.48: Maximum Exit Area for Second Mode	58
Figure 2.49: Flow Velocity Profile of Bimorphs	59
Figure 2.50: Maximum Flow Velocity for First Mode	60
Figure 2.51: Maximum Flow Velocity for Second Mode	60
Figure 3.1: Power Resistor Cooling Physical Setup	61
Figure 3.2: Power Resistor Setup Heat Source	62
Figure 3.3: Temperature Profile of Heat Source with Various Power Inputs	63
Figure 3.4: Least Squares Fit of Temperature Profile at 6.05 Watts	65
Figure 3.5: Temperature Profile Plot during Heating (13W)	68
Figure 3.6: Temperature Profile Plot during Cooling (13W)	69

Figure 3.7: Conservation of Energy Method (6.05W)	70
Figure 3.8: Convection Coefficient for 6.05W Input	71
Figure 3.9: Conservation of Energy Approach with Dynamic Convection (6.05W)	72
Figure 3.10: Conservation of Energy Fit to determine β	73
Figure 3.11: Conservation of Energy Fit to determine W_{res}	74
Figure 3.12: Conservation of Energy Prediction of Processor Temperature w/ Natural Cooling	75
Figure 3.13: Conservation of Energy Prediction of Processor Temperature w/o Fan	75
Figure 4.1: Power Resistor Cooling using Bimorph Setup	76
Figure 4.2: 5H Bimorph Cooling at Various Gaps and Amplitude	78
Figure 4.3: Power Resistor Cooling using 5A Bimorph	79
Figure 4.4: Steady-state Temperature of Power Resistor System	79
Figure 4.5: Power Resistor Cooling using SS Bimorph	81
Figure 4.6: Volumetric Flow Rate vs. Steady-state Temperature	82
Figure 4.7: Bimorph Cooling Setup	83
Figure 4.8: Aluminum Plate Cooling Setup	84
Figure 4.9: Temperature of Processor w/ 5A Bimorph and Aluminum Plate Cooling	84
Figure 4.10: Temperature of Celeron® Processor w/ 5A Bimorph Cooling	85
Figure 4.11: Copper Folded-Fin Heat Sink	87
Figure 4.12: Aluminum Extruded Heat Sink	88
Figure 4.13: Convection Coefficient for Extruded and Folded-Fin Heat Sinks	89
Figure 4.14: Steady-State Ansys® Analysis of Copper Folded-Fin Heat Sink	89
Figure 4.15: Steady-State Ansys® Analysis of Aluminum Extruded Heat Sink	90

CHAPTER 1

INTRODUCTION

1.1 MOTIVATION OF RESEARCH

As the number of transistors in an integrated circuit doubles every couple of years according to “Moore's Law” (figure 1.1), the heat generation from that circuit also increases. This increase results in the need for larger and more powerful cooling systems. Larger cooling systems is a serious problem for notebook computers whose main objective is to become smaller and lighter. Research has been performed which has tried to address this problem with different approaches [1-2]. One solution to this problem is to replace the fan with a device that is able to produce the same amount of heat dissipation, but require less space to do so.

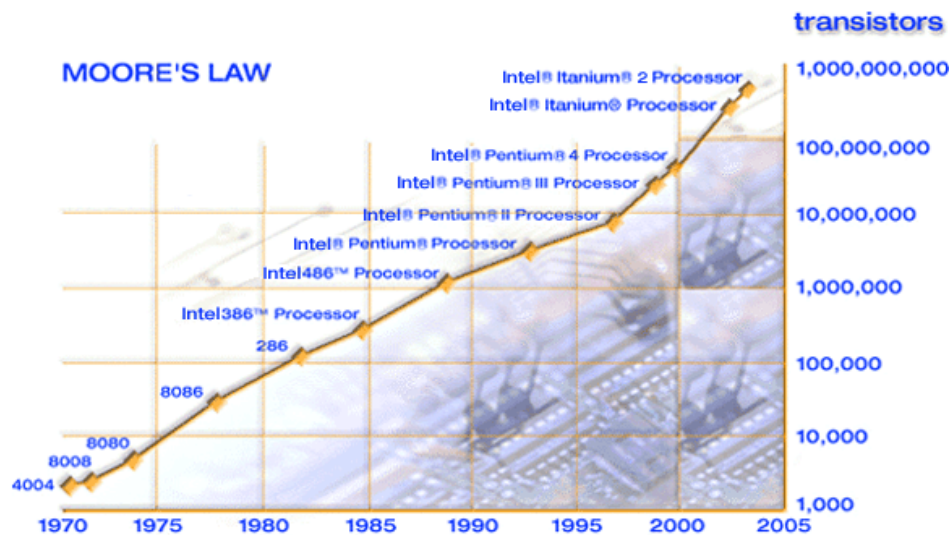


Figure 1.1: Moore's Law

1.2 Current Notebook Cooling Methods

There are several different methods by which current computer manufacturers are able to successfully cool the latest processors for notebook computers.

1.2.1 Remote Heat Exchanger (RHE)

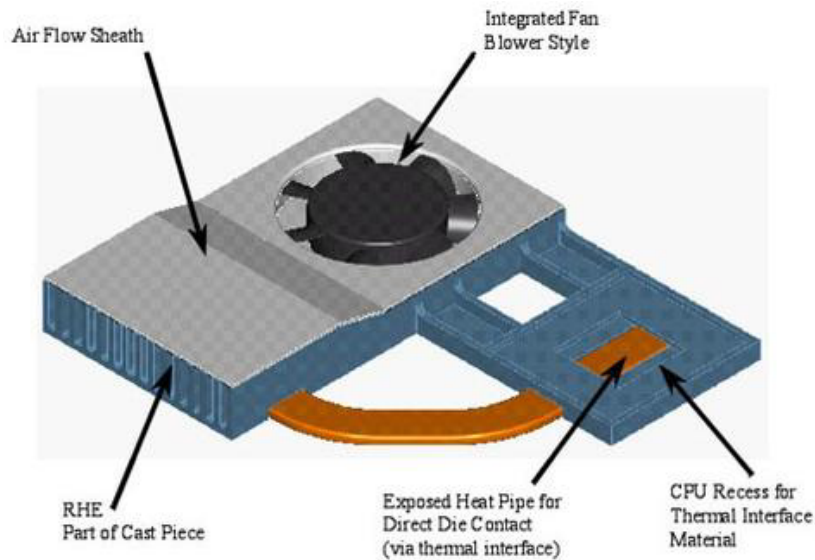


Figure 1.2: Remote Heat Exchanger Cooling System

The main source of cooling for current notebook computers is what is known as the Remote Heat Exchanger system (Figure 1.2) [3]. The system basically consists of three main components. They are a heat pipe, heat sink and fan. The number of these components in a typical notebook computer depends on the power output of the processor. Figure 1.3 provides an example of a cooling system meant for current high power processors, which can emit over 70W of heat [4].

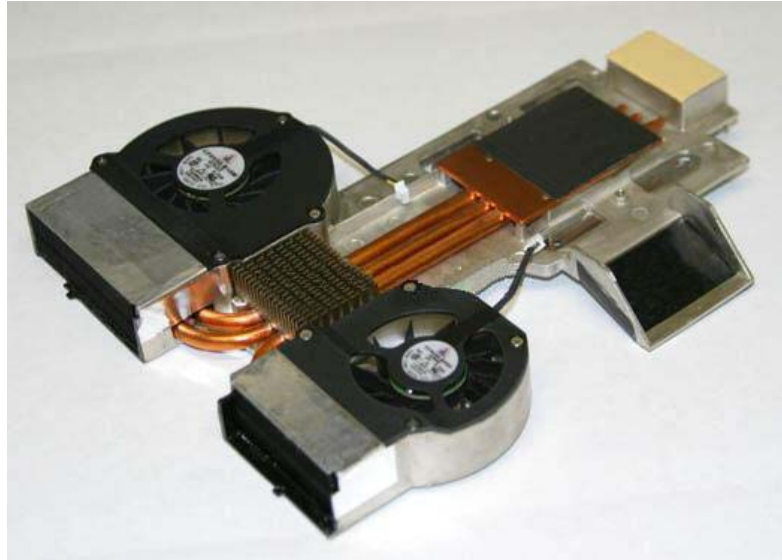


Figure 1.3: Compaq Notebook Cooling System

The Heat Sink

The heat sink and fan make up the primary components of the RHE. It is through these two devices that remote heat exchange occurs.

There are several different methods in which a heat sink is manufactured [5]. There are extruded, folded-fin, cold-forged, bonded/fabricated fin, and skived fin heat sinks. Of the five types the extruded, folded fin and bonded/fabricated fin are most commonly used in notebook computers. The extruded heat sink is the least expensive and easiest to manufacture (figure 1.4) [6]. This type of heat sink, which is usually made of aluminum, can be formed into a variety of fin orientations using the extrusion process.



Figure 1.4: Extruded Heat Sink

Another type of heat sink is the folded fin (figure 1.5) [7]. This heat sink is formed by taking a single sheet of metal and bending it to form several fins. The folded structure is then attached to a base plate. Using this method a sink can be formed from either aluminum or copper.



Figure 1.5: Folded Fin Heat Sink

The bonded/fabricated fin heat sink (figure 1.6) is very similar to the folded fin except that each of the fins is individually bonded to the base plate. As long as the manufacturing process is well-controlled, this type can have the highest thermal conductivity of the three.

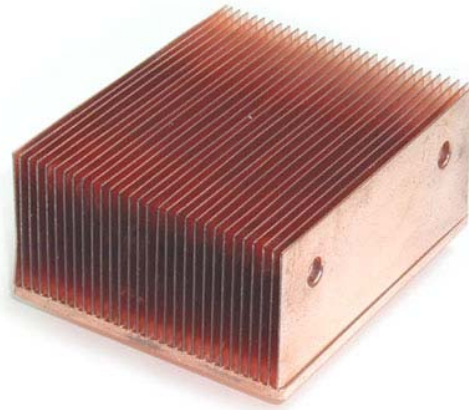


Figure 1.6: Bonded/Fabricated Heat Sink

The Fan

While the DC fan was a common device to use to cool Pentium® type processors, higher power processors are usually cooled by blower type fans as seen in figure 1.3.

The Heat Pipe

The heat pipe is the first device in the RHE (Figure 1.3). It is the conduit through which heat is transferred from the processor to the heat sink. A heat pipe is a specially designed copper pipe that transfers heat through the evaporation and condensation of a liquid inside the pipe (figure 1.7) [8]. Basically, the heat from the processor will evaporate the liquid. The evaporated liquid will then move down the pipe to the heat sink where it will condense. The liquid will then be drawn back to the processor through the use of a wicking material or capillary channels inscribed into the wall of the pipe. Through this process a heat pipe can transfer approximately 20W of heat with very little losses [9]. In fact the thermal

conductivity of a heat pipe can be several hundred of times better than just plain copper.

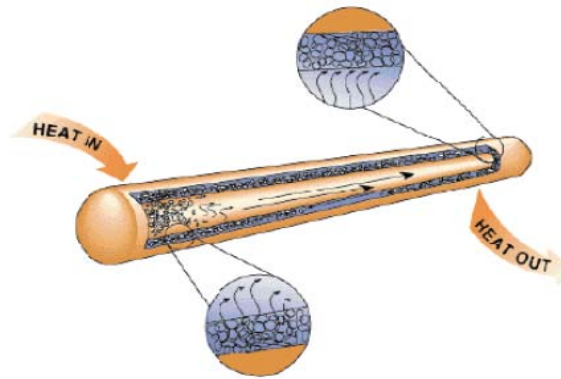


Figure 1.7: Heat Pipe

1.2.2 Metal-core Printed Circuit Boards and Stamped Plates

Another method which is used to remove heat from the processor is using metal-core printed circuit boards. These basically act like one large heat sink [5]. The drawback of using such a design is that all of the components in the circuit board cannot be heat sensitive. Another component commonly used in notebook computers is a stamped aluminum plate attached to the bottom of the keyboard. Just as the printed circuit boards the stamped plate acts as a large heat sink. Again the drawback with this system is that the components near this plate cannot be very heat sensitive.

1.3 Acoustic Streaming

In general, acoustic streaming is considered to be circular flow in a fluid induced by a vibrating object. There has been a considerable amount of research performed concerning acoustic streaming [10-26]. There is considered to be two main types of acoustic streaming.

They are Raleigh streaming and quartz wind. Raleigh streaming is due to standing sound waves that develop between a stationary and vibrating object [27-28]. The most typical example is streaming that develops between an undulating beam and a fixed plate (figure 1.8). Near boundary acoustic streaming can be defined by equation 1.1 [29].

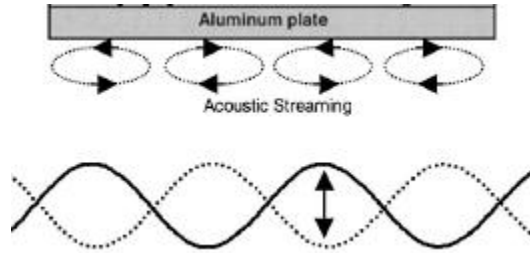


Figure 1.8: Rayleigh Streaming

$$\begin{aligned} \mu \nabla^2 u_2 - \nabla P_2 + F &= 0 \\ F &\equiv -\rho_0 \langle (u_1 \cdot \nabla) u_1 + u_1 (\nabla \cdot u_1) \rangle \end{aligned} \quad (1.1)$$

where:

μ : kinematic viscosity

ρ_0 : constant equilibrium density

u_1 : oscillatory particle velocity

u_2 : acoustic streaming velocity

P_2 : steady-state “dc” pressure

F : nonlinear driving forcing term

$\langle \rangle$: time average over many cycles

From equation 1.1, the streaming velocity at the surface of the stationary plate can be defined as

$$U_L = -\frac{3}{8} f \lambda_b \left(\frac{A}{h} \right)^2 \sin 2k_b x \quad (1.2)$$

where:

f : excitation frequency (Hz)

λ_b : wavelength of the beam

A : amplitude of the vibrating beam

h : gap between vibrating and stationary beam

k_b : bending wave number of the beam ($2\pi/\lambda_b$)

The quartz wind is a more recently discovered type of acoustic streaming [30]. This type of streaming occurs when any ultrasonically excited object emits a high intensity sound wave in a fluid. Unlike the Raleigh streaming the quartz wind can occur with or without a stationary object.

1.3.1 Convective Heat Transfer

Research has been performed which looked at convective heat transfer induced by acoustic streaming [31-38]. It has been found that streaming created between an ultrasonically excited beam and a stationary heat source creates forced convection across the surface of the heat source [39]. One method for creating a vibrating beam is through the used of a piezoelectric bimorph [40]. It has been shown as seen in figure 1.9 that using a bimorph is able to provide cooling to a 3.12W heat source [41]. Adding slots to the bimorph further enhances the convective cooling induced by the bimorph with the optimal slots being two as seen in figure 1.10.

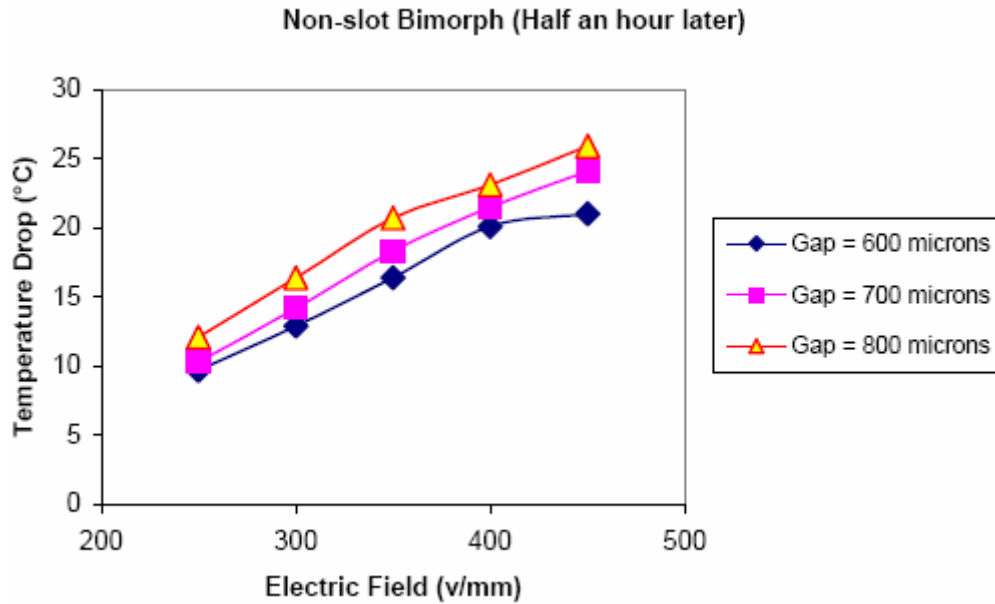


Figure 1.9: Convective Cooling using Piezoelectric Bimorph

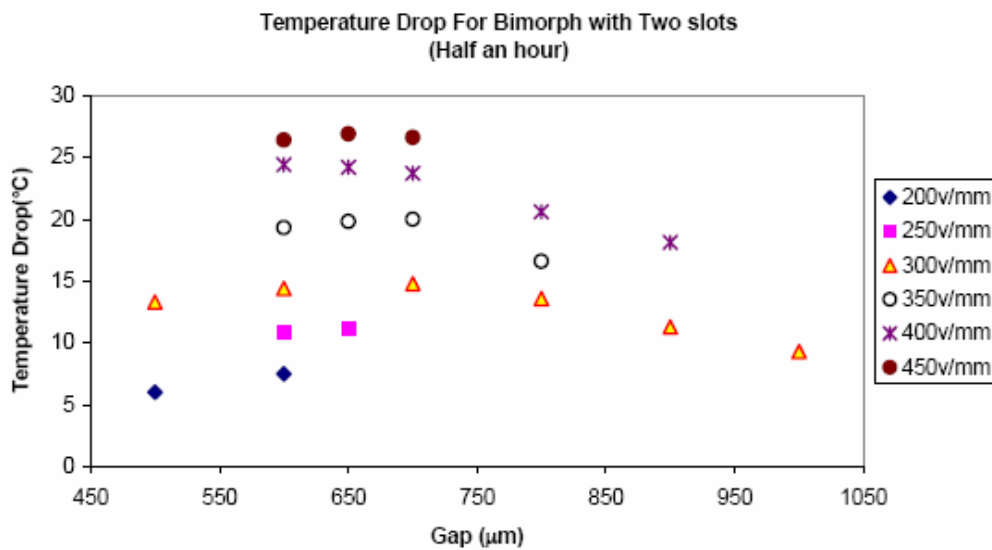


Figure 1.10: Convective Cooling using Slotted Piezoelectric Bimorph

1.4 Research Objectives

This paper will look at the heat dissipation requirements of current portable computers and

the applicability of using PZT bimorphs to fulfill these requirements. This will be done by assessing the cooling capabilities of a bimorph for forced convective flow. Unlike previous research which has focused on convective heat transfer using acoustic streaming, this paper will look at the ability of a bimorph to obtain this same cooling using bulk airflow.

CHAPTER 2

THEORETICAL ANALYSES

2.1 HEAT ANALYSIS OF DELL® INSPIRON™ COOLING SYSTEM

2.1.1 System Identification

The computer system that was analyzed is a Dell® Inspiron™ 3800 series notebook. The notebook was running the Windows 98® operating system on an Intel® Celeron® processor. This processor was operating at 600 MHz with a core voltage of 1.6V.

Cooling System

Even though this is an older computer system, its cooling system still utilizes the same techniques as current systems. The position of the cooling system and processor with respect to the other computer components can be seen in figure 2.1. From this figure it can be seen that the components which are the most heat sensitive, such as the hard drive, are furthest away from the processor.

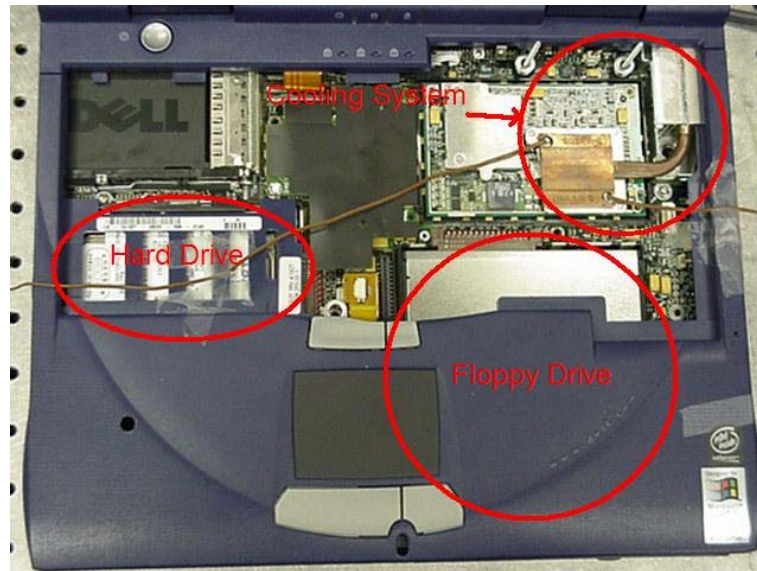


Figure 2.1: Overall Layout of Inspiron™ Notebook

The cooling system itself (figure 2.2 and 2.3) consists of four main components which make up a Remote Heat Exchanger. Directly above the processor exists a copper contact plate, which draws away the processor's emitted heat. The next component is the copper heat pipe. Its purpose is to transport the heat from the copper plate to the next component, the heat sink. The aluminum heat sink is a simple extruded design with ten fins. The final component is a 5V SUNON KDE0503PEBX-8 DC Fan rated to move 5.3 CFM of air. The overall cooling system works by moving heat from the processor to the heat sink using the copper plate and heat pipe. The heat sink is then cooled through forced convection by the fan. The fan draws in air from slots in the side of the computer and ejects it out the back.

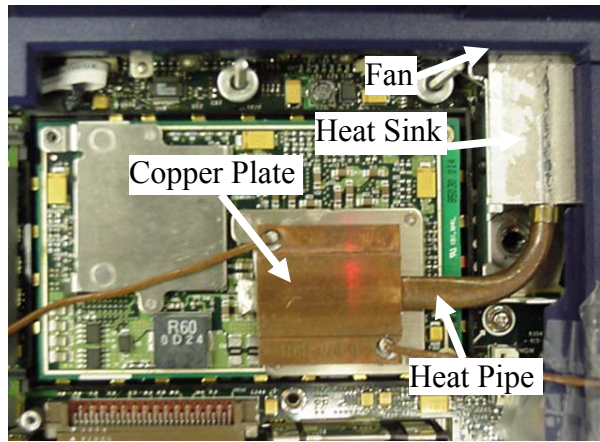


Figure 2.2: Dell® Inspiron™ Cooling System Closeup

There is one more component that plays a part in the cooling of the processor. It is an aluminum stamped plate on the bottom of the keyboard. This plate was set up to be in contact with the top of the copper contact plate and thus act as a heat spreader. However, temperature data of the other cooling components could not be obtained with the keyboard in its operating position. Therefore, the cooling due to conduction through the stamped plate was replaced by natural convection at the top of the copper plate. Whether this is a viable substitution will be shown later.

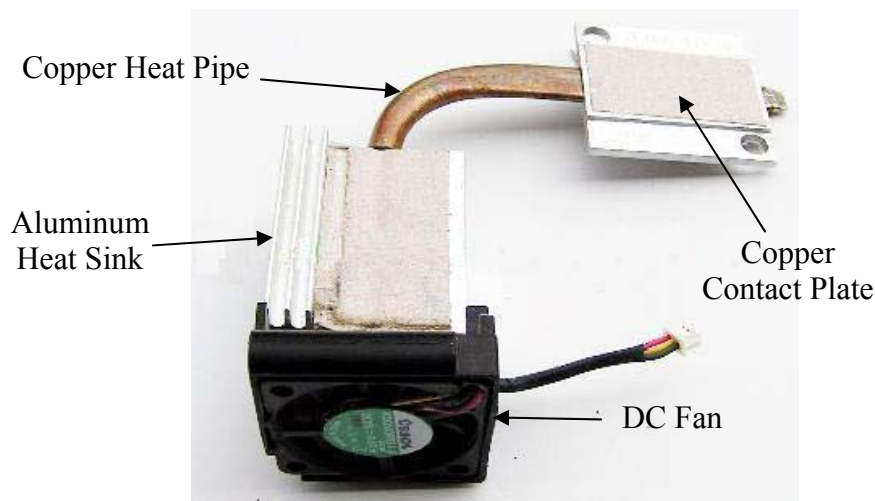


Figure 2.3: Dell® Inspiron™ Cooling System Overview

Temperature Profile Test Setup

The temperature of most processors is monitored by the computer itself through the use of a thermal diode. This diode is usually located directly in the center of the processor [42].

Access to the diode's readings for the Inspiron™ system could not be obtained. Therefore, two thermocouples were placed on opposite corners of the processor. Their specific locations can be seen in figure 2.4.

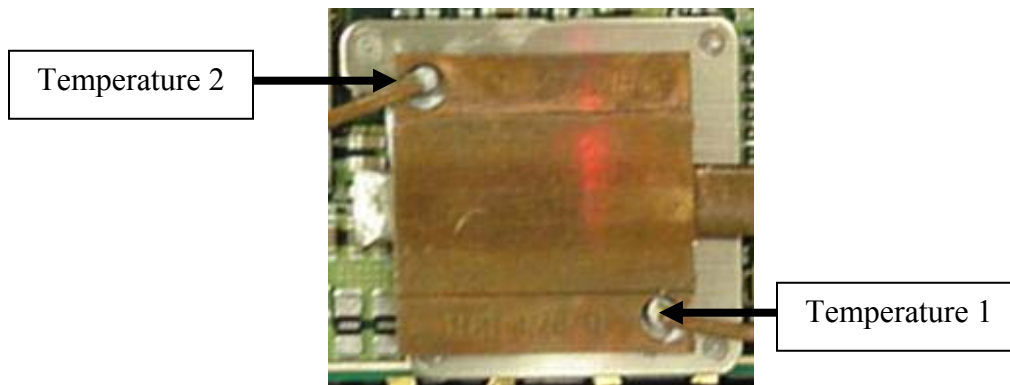


Figure 2.4: Location of Temperature Thermocouples on Processor

Temperature readings were taken with FLUKE® 80PK-1 bead thermocouples using a FLUKE® 54II series thermometer. The thermometer displays digital readings of the temperature from a maximum of two thermocouples. It also contains a logging feature that allows temperature readings to be stored at desired time intervals. The thermocouples themselves have an accuracy of ± 1.1 °C for temperatures between 0 and 260 °C.

In order to get an idea of the cooling capabilities of the Inspiron™ system, thermocouples were also placed on the top of the copper plate in the middle and at the base of the aluminum heat sink.

Software Setup

When a task is performed by a processor such as adding two integers, the entire processor is not used. Instead, a processor is divided up into different sections which by themselves only perform certain tasks [43]. Figure 2.5 shows the typical layout for a Pentium® processor. While current processors have many more division than this, most processors can still be divided into two main portions, which are datapath and control. All of the other sections perform tasks that are in some way or another related to these two main portions. The purpose of the datapath is to perform the arithmetic operations (integer and floating point sections in figure 2.5) while control is the watchdog of all operations. It tells the datapath, memory and I/O devices such as a hard drive what they should be doing based upon the current program running on the computer.

Therefore, in order to have the processor put out the maximum amount of heat, all of the regions of the processor have to be operating simultaneously. This was accomplished by writing a C++ program that has the processor perform a floating point and integer operation continuously as seen by the flow chart in figure 2.6. This program will cause the floating point and integer datapaths to be operating continuously. The control portion of the processor should always be operating as long as an instruction is being performed. The caches on the processor should also be active because the control and datapath sections are performing work.

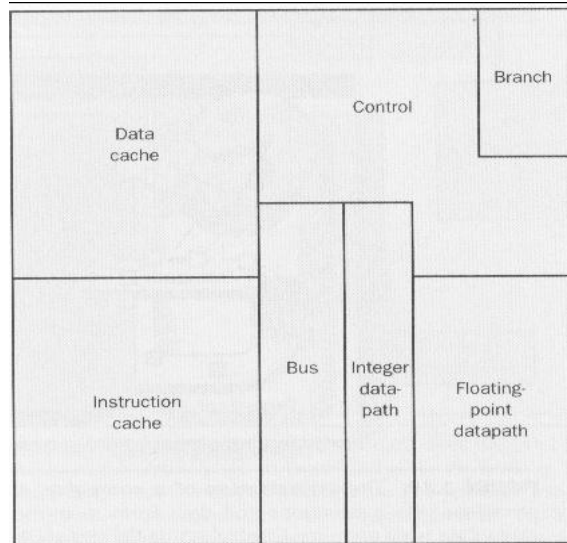


Figure 2.5: Layout of Pentium® Processor

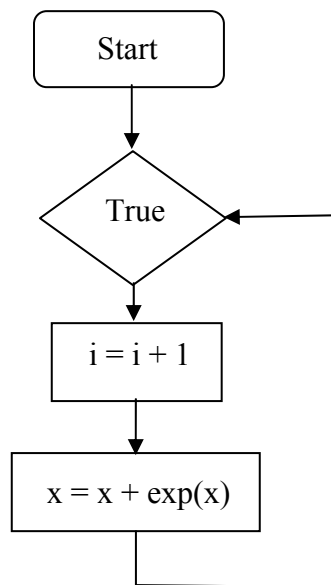


Figure 2.6: Flow Chart of 'Full Load' Program

Temperature Profile of System Results

Temperature data of the Celeron® processor was recorded while the processor was under what is considered a full load (i.e. program mentioned above was running). Figure 2.7 displays the temperature of the processor as it starts out from room temperature (20.6 °C) and increases until the fan in the notebook computer turns on. During the beginning of this process the computer is booting up and once started the C++ program begins running for the remainder of the test. The boot up process takes approximately 25 seconds.

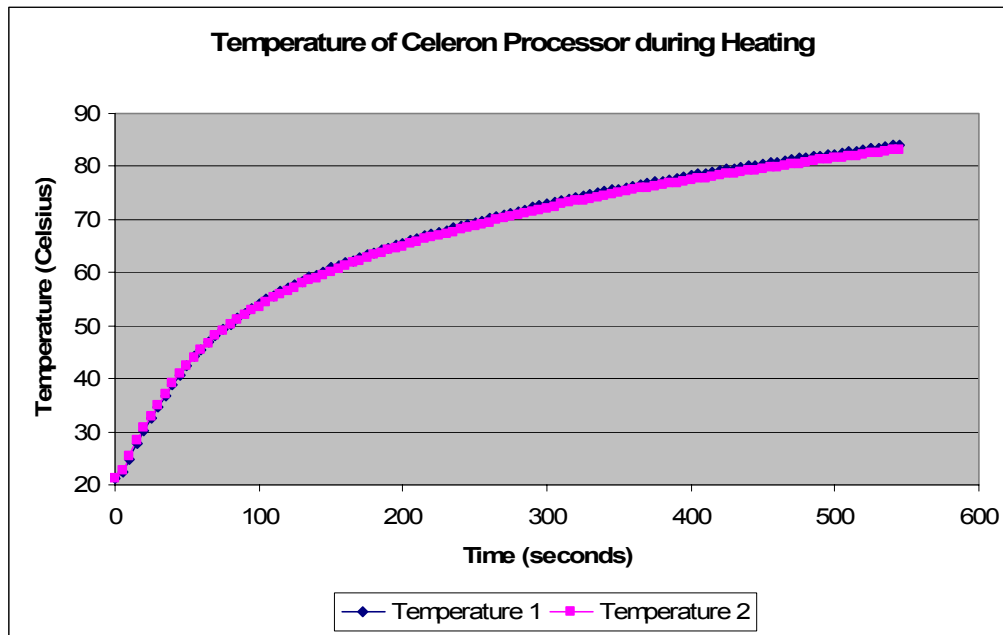


Figure 2.7: Temperature of Celeron® Processor w/o Fan

Figure 2.8 shows the temperature of the processor once the fan of the cooling system turns on. The test data continues until the temperature of the processor gets below a critical level and the fan turns off.

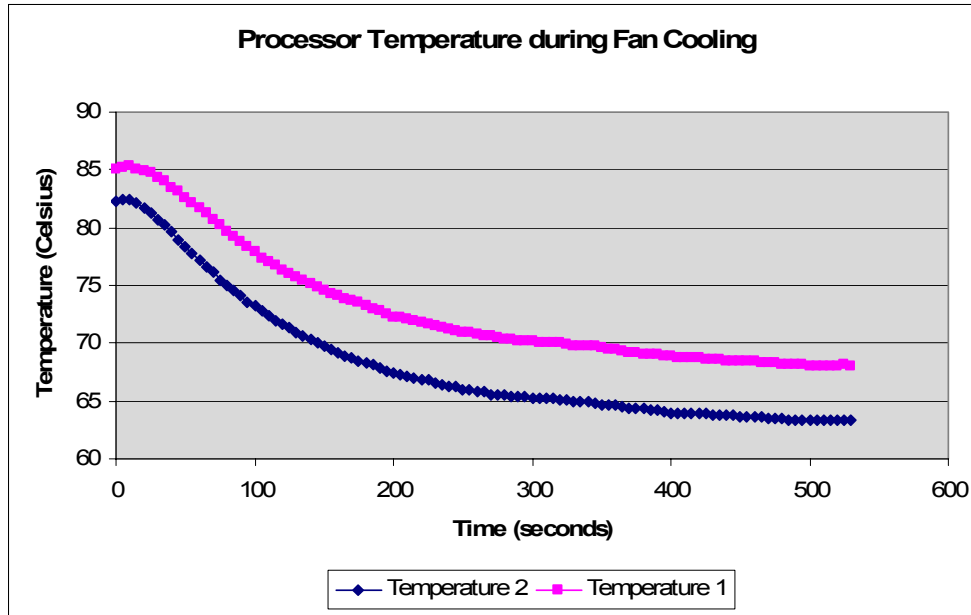


Figure 2.8: Temperature of Celeron® Processor w/ Fan

From the two figures above it can be seen that the temperature of the processor at the ‘Temperature 1’ position is higher than at the ‘Temperature 2’ position. One likely possibility for this is that the processor is still not being put under a full load even with the C++ program. Another reason could be due to the location of the thermocouples in relation to the cooling system. The ‘Temperature 2’ thermocouple is further away from the main part of the cooling system compared to the ‘Temperature 1’ thermocouple (figure 2.4). This reasoning could be supported further by the fact that the difference between the two temperatures is larger during the cooling phase than in the heating phase.

Temperature profiles were found for the top of the copper plate and the base of the heat sink as seen in figures 2.9 and 2.10. When the fan is not on during the heating of the system, the temperatures of both components is very close to being the same. This reinforces the fact, as was mentioned in the introduction, that there is very little heat loss from a heat pipe. When the fan introduces forced convection resulting in the cooling of the system, the two

temperatures separate from each other with a distinct difference between them. This is expected since the heat sink is now being cooled and should be at a lower temperature than the rest of the system.

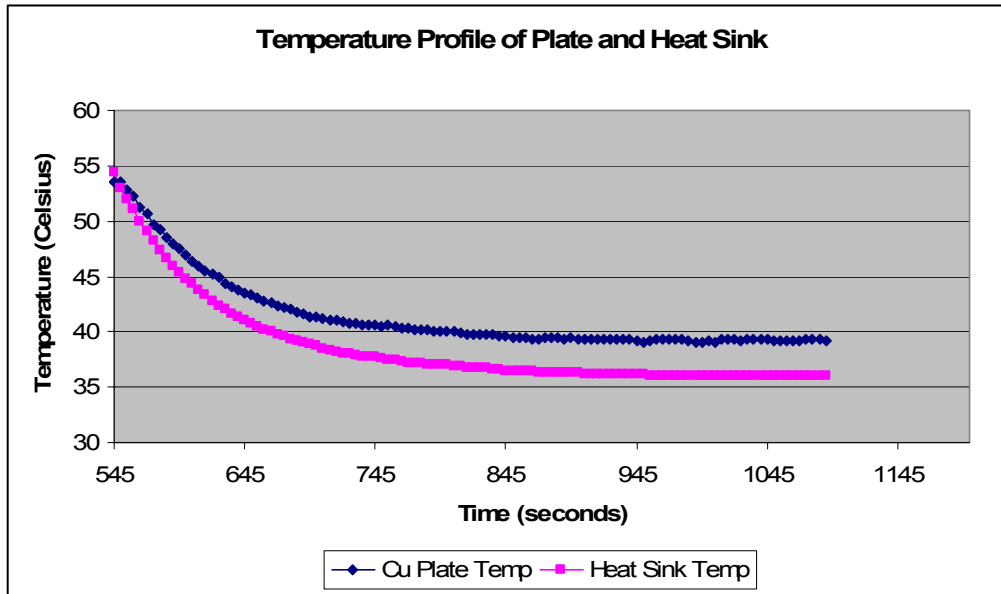


Figure 2.9: Temperature of Copper Plate and Heat Sink w/o Fan

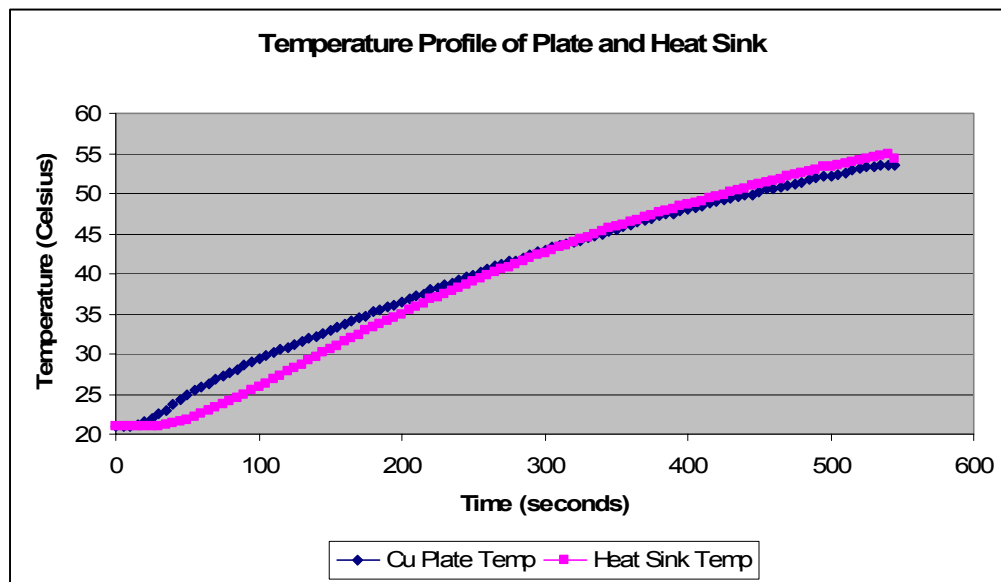


Figure 2.10: Temperature of Copper Plate and Heat Sink w/ Fan

2.1.2 Analytical Heat Transfer Analysis

In order to determine the rate of heat transfer (or heat dissipation) of the computer's existing cooling system, heat transfer analysis was performed. The analysis looked at the conductive (equation 2.1) and convective (equation 2.2) mechanisms of heat transfer [44]. Radiation transfer was ignored in order to simplify the computations.

$$\dot{Q} = kA \frac{\Delta T}{L} \quad (2.1)$$

where:

k : thermal conductivity of material

A : surface area

L : thickness of material

$$\dot{Q} = hA(T_s - T_\infty) \quad (2.2)$$

where:

h : convection heat transfer coefficient

T_s : surface temperature

T_∞ : ambient temperature

Rate of Heat Transfer from Copper Plate

The rate of heat transfer through the copper plate was found by using both equations 2.1 and 2.2. There would be conduction through the thickness of the copper and natural convection

from the surface of the plate. The total heat transfer was then found by combining equations 2.1 and 2.2 such that

$$\dot{Q} = \frac{T_p - T_\infty}{\frac{1}{hA} + \frac{L}{kA}} \quad (2.3)$$

where T_p is the temperature of the processor. The values needed to solve for the heat transfer can be seen in the following table.

Length	34mm
Width	34mm
Thermal Conductivity	401 W/m °C
T_∞	20.6 °C

Table 2.1: Properties of Copper Plate

The convection heat transfer coefficient for the copper plate is due to natural convection from the surface of the plate. The coefficient can be determined from the Nusselt number (Nu) as seen in the following equation.

$$h = \frac{Nu \cdot k}{\delta} \quad (2.4)$$

In this equation, k is the thermal conductivity of air and δ is the characteristic length of the plate. For a horizontal plate, the characteristic length is the surface area of the plate divided by its perimeter ($\delta = A/p$). The thermal conductivity of air is dependent on the film temperature of the plate, which is the average of the plate's surface temperature and the ambient air temperature. The Nusselt number can be derived from equation 2.5 for a horizontal plate that is face up.

$$Nu = 0.54Ra^{1/4} \quad (2.5)$$

Ra is the Rayleigh number. This number can be derived from equation 2.6.

$$Ra = \frac{g\beta(T_s - T_\infty)\delta^3}{\nu^2} Pr \quad (2.6)$$

where:

g = gravitational acceleration, m/s^2

β = coefficient of volume expansion, $1/T_{film}$

T_s = temperature of the surface, °C

T_∞ = ambient temperature, °C

δ = characteristic length of plate

ν = kinematic viscosity of air, m^2/s

Pr = Prandtl number

The kinematic viscosity, Prandtl number and thermal conductivity of air are dependent on the film temperature of the plate. As the temperature of the plate increases these three values change. There exist tables which list each of the three values for air at different temperatures. In order to obtain values in between those mentioned in the tables linear interpolation was performed which results in equations 2.7, 2.8 and 2.9 for each of the three properties.

$$Pr = 0.712 + (26.85^\circ C - T_{film}) \left(\frac{Pr_{26.85^\circ C} - Pr_{76.85^\circ C}}{50^\circ C} \right) \quad (2.7)$$

where:

T_{film} : film temperature

$Pr_{76.85^\circ C}$: Prandtl number of air at $76.85^\circ C$, 0.706

$Pr_{26.85^\circ C}$: Prandtl number of air at $26.85^\circ C$, 0.712

$$v = 1.57 \times 10^{-5} \text{ m}^2/\text{s} - (26.85^\circ\text{C} - T_{film}) \left(\frac{v_{76.85^\circ\text{C}} - v_{26.85^\circ\text{C}}}{50^\circ\text{C}} \right) \quad (2.8)$$

where:

$v_{26.85^\circ\text{C}}$: kinematic viscosity of air at 26.85°C, 1.57x10-5 m²/s

$v_{76.85^\circ\text{C}}$: kinematic viscosity of air at 76.85°C, 2.06x10-5 m²/s

$$k = 0.0261 \text{ W}/\text{m} \cdot ^\circ\text{C} - (26.85^\circ\text{C} - T_{film}) \left(\frac{k_{76.85^\circ\text{C}} - k_{26.85^\circ\text{C}}}{50^\circ\text{C}} \right) \quad (2.9)$$

where:

$k_{26.85^\circ\text{C}}$: thermal conductivity of air at 26.85°C, 0.0261 W/m · °C

$k_{76.85^\circ\text{C}}$: thermal conductivity of air at 76.85°C, 0.0297 W/m · °C

The changing convection coefficient is shown in figure 2.11 when the fan is off and 2.13 when the fan is on. Using these convection heat transfer coefficients the total heat transfer through the copper plate can be found from the temperature of the processor (figures 2.7 and 2.8) and equation 2.3. The heat transfer through the copper plate over time can be seen in figures 2.12 and 2.14. During the time when the system is heating and the fan is off, the convection coefficient and rate of heat transfer both follow a logarithmic curve. The convection coefficient is increasing because the plate's temperature is increasing. A higher coefficient means more heat is being dissipated and hence the rate of heat transfer increases.

During the time the fan is on in figures 2.13 and 2.14, the convection coefficient and the rate of heat transfer goes down. Both factors decrease when the fan is on because the system is cooling and more heat is being routed to the cooler heat sink (figure 2.10) than to the surface

of the copper plate. From these results it should be expected that since the rate of heat transfer is decreases in this part of the cooling system, it should be increasing else where such as the heat sink.

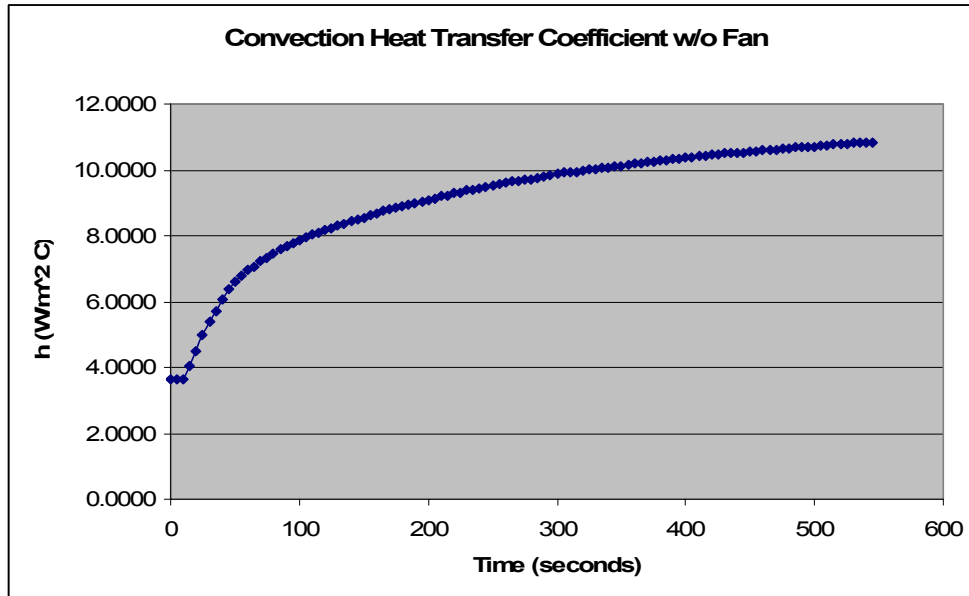


Figure 2.11: Convection Coefficient for Copper Plate w/o Fan

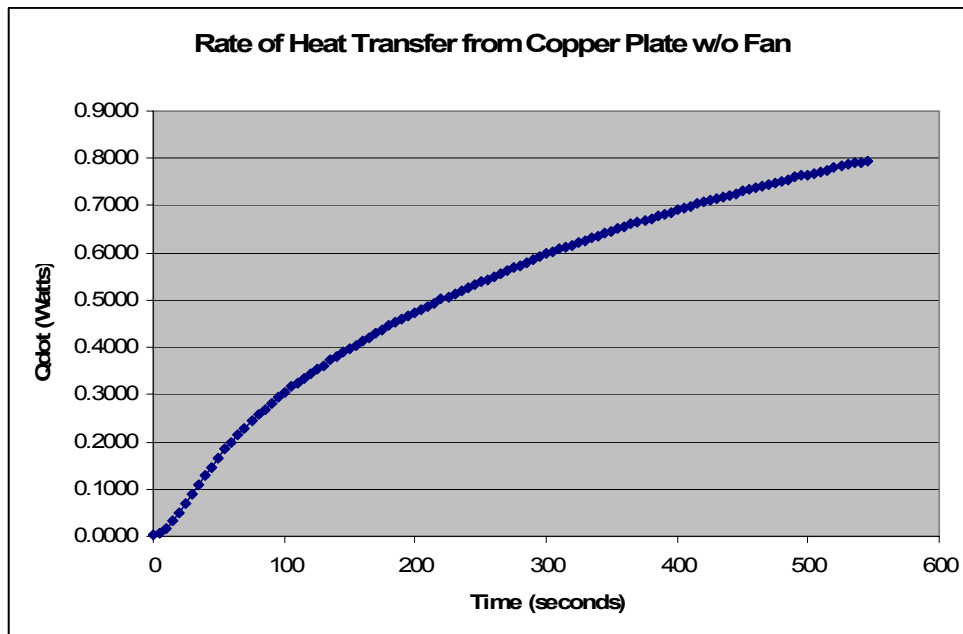


Figure 2.12: Rate of Heat Transfer from Copper Plate w/o Fan

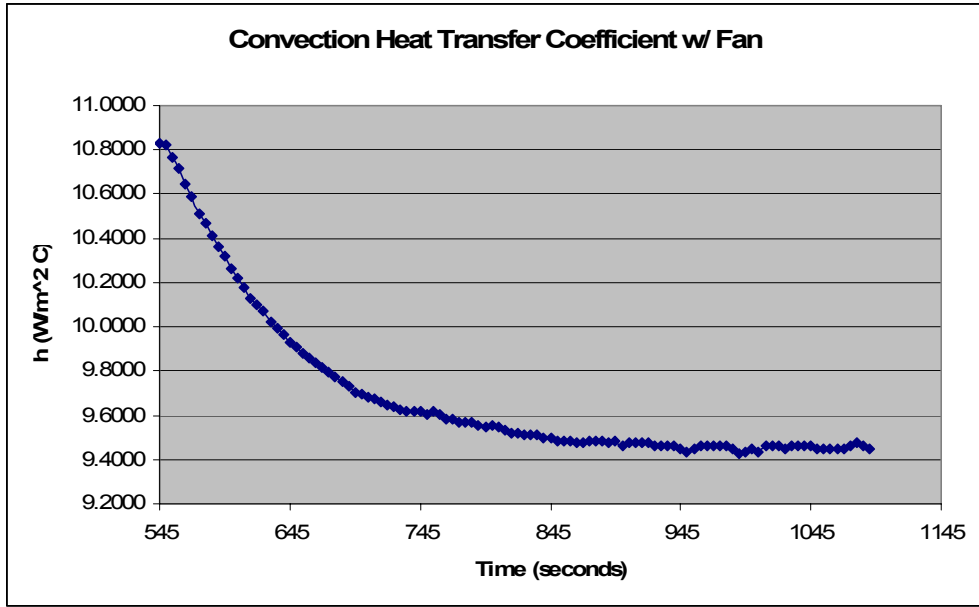


Figure 2.13: Convection Coefficient for Copper Plate w/ Fan

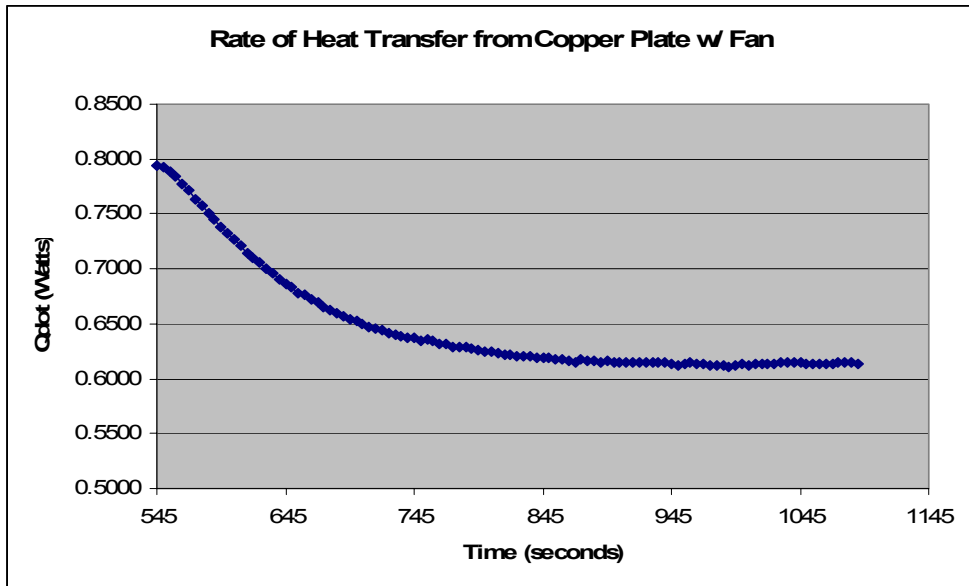


Figure 2.14: Rate of Heat Transfer from Copper Plate w/ Fan

Rate of Heat Transfer from Heat Pipe

The next part in the computer's cooling system is the heat pipe. The heat pipe is a specially

developed component that is designed to have a very high thermal conductivity through an internal capillary action [8-9]. Because of the high thermal conductivity, it is assumed that there is negligible heat loss through the pipe, which as mentioned earlier is shown in figure 2.9.

Rate of Heat Transfer from Heat Sink and Fan

The final piece of the computer's cooling system is the heat sink and fan. The rate of heat transfer from a finned surface can be found from equation 2.10 [44].

$$\dot{Q} = h(A_{unfin} + \eta A_{fin})(T_b - T_\infty) \quad (2.10)$$

where:

A_{unfin} : the surface area not covered by a fin

η : fin efficiency

A_{fin} : surface area of the fin

T_b : temperature at the base of the fin

As can be seen from equation 2.10, the rate of heat transfer from a finned surface is mainly due to convection from that surface. The only place where conduction comes into play is in the fin efficiency, which is found from a fin efficiency profile plot (figure 2.15) for a rectangular fin using

$$\xi = (L + \frac{1}{2}t)\sqrt{\frac{h}{kt}} \quad (2.11)$$

where:

L : length of fin

t : thickness of fin

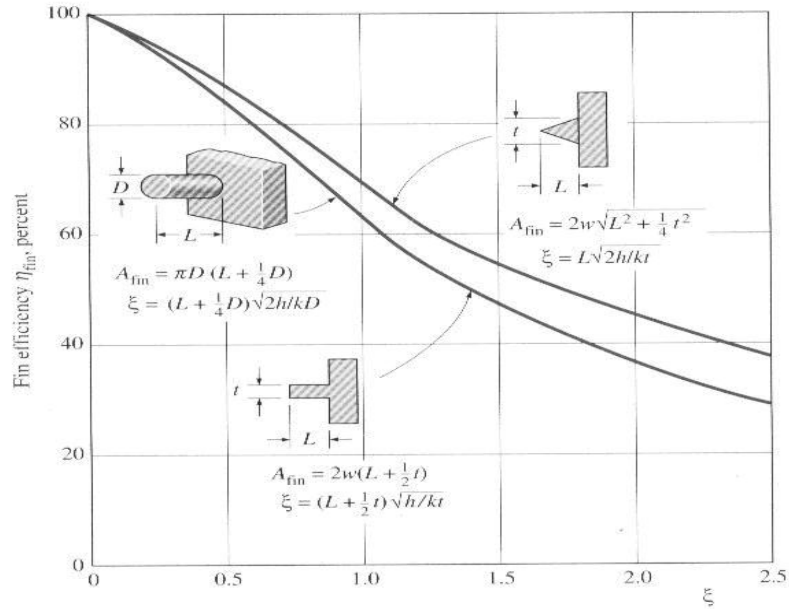


Figure 2.15: Fin Efficiency Profile Plot

Using the above figure, the efficiency for the particular heat sink used in this computer can be approximated as 90%. The dimensions of the heat sink can be seen in Table 2.2.

A_{unfin}	$8.73 \cdot 10^{-2} \text{ m}^2$
η	90.00%
A_{fin}	$6.66 \cdot 10^{-4} \text{ m}^2$

Table 2.2: Characteristics of Heat Sink

The convection heat transfer coefficient is different for the heating and cooling of the processor. During heating the coefficient is determined based only on natural convection whereas during cooling there is forced convection provided by the fan.

For natural convection the convection heat transfer coefficient is found in the same manner as for the copper plate, using equations 2.4, 2.6, 2.7, 2.8 and 2.9. The Nusselt number (equation 2.12), however, is slightly different because the heat sink fins are actually vertical plates. Also, the characteristic length (δ) of a vertical plate is the height of the plate, which is

on average 0.0108m for the heat sink.

$$Nu = \left\{ 0.825 + \frac{0.387Ra^{1/6}}{(1 + (0.492/Pr)^{9/16})^{8/27}} \right\}^2 \quad (2.12)$$

For forced convection over a flat plate, the convection heat transfer coefficient is still determined from equation 2.4, but the Nusselt number is now dependent on the Reynold's number and whether the air flow is laminar or turbulent. The Reynold's number (Re) is determined from equation 2.13.

$$Re = \frac{VL}{\nu} \quad (2.13)$$

where:

V : upstream air velocity

L : characteristic length

ν : kinematic viscosity of air

In forced convection the characteristic length is the length in the direction of air flow, which would be 0.037m for the heat sink. The upstream air velocity produced by the fan is approx. 12.76 m/s. Since the kinematic viscosity of air is variable with temperature (equation 2.8), the Reynold's Number will also change depending on the temperature of the heat sink.

Figure 2.16 shows the Reynold's Number still remains in the laminar region (i.e. $Re < 5 \times 10^5$) throughout the entire cooling process. For laminar flow the Nusselt number is

$$Nu = 0.664 Re^{0.5} Pr^{1/3} \quad (2.14)$$

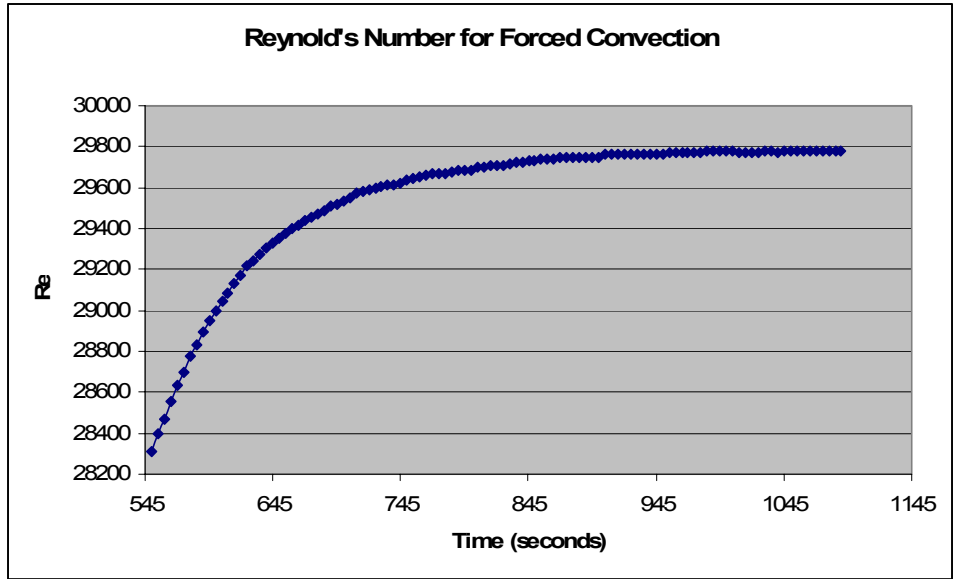


Figure 2.16: Reynold's Number for Forced Convection through Heat Sink

The rate of heat transfer can now be found using equation 2.10 along with the temperature at the base of the heat sink for both natural and forced convection (figure 2.9 and 2.10). The rate of heat transfer from the heat sink can be seen in figure 2.17 without the fan and figure 2.18 with the fan.

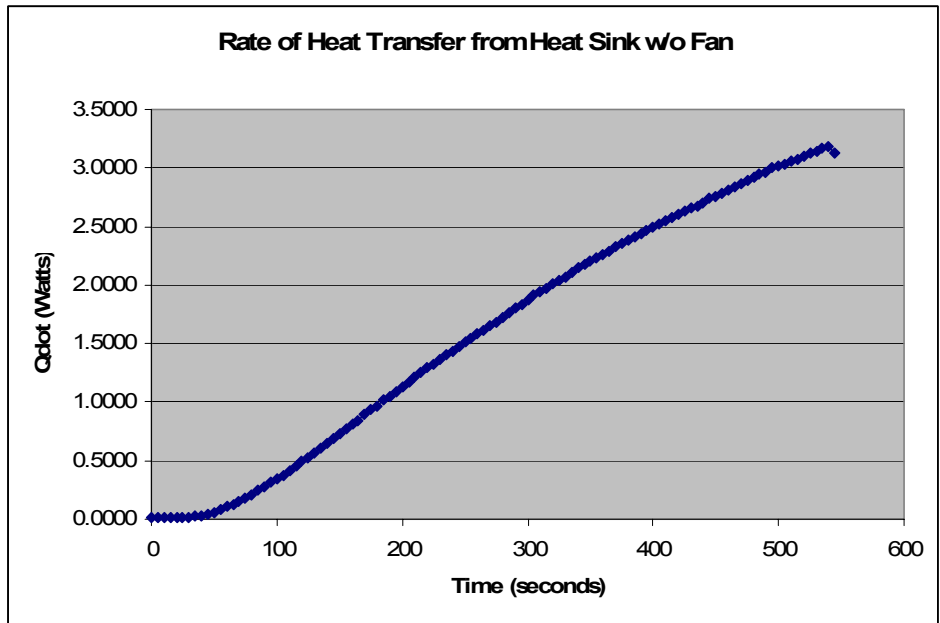


Figure 2.17: Rate of Heat Transfer from Heat Sink w/o Fan

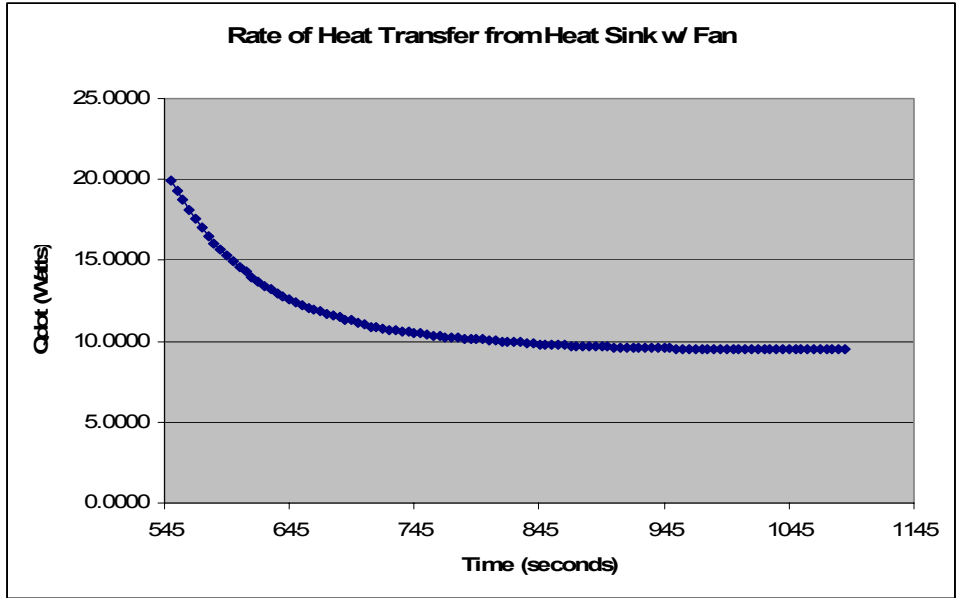


Figure 2.18: Rate of Heat Transfer from Heat Sink w/ Fan

Figure 2.17 shows that the heat sink dissipates a little over 3 Watts of heat through natural convection before the fan turns on. Once the fan is on, the rate of heat transfer surges to over six times that amount. The rate of heat transfer then decreases until the system reaches equilibrium. At that point, the heat sink and fan together are dissipating about 10 Watts.

Rate of Heat Transfer from Entire Cooling System

The total rate of heat transfer from the entire cooling system is determined by adding the transfer from the copper plate (figures 2.12 and 2.14) and the transfer from the heat sink (figure 2.17 and 2.18). Plots of the total heat transfer during heating can be seen in figure 2.19 and cooling in figure 2.20.

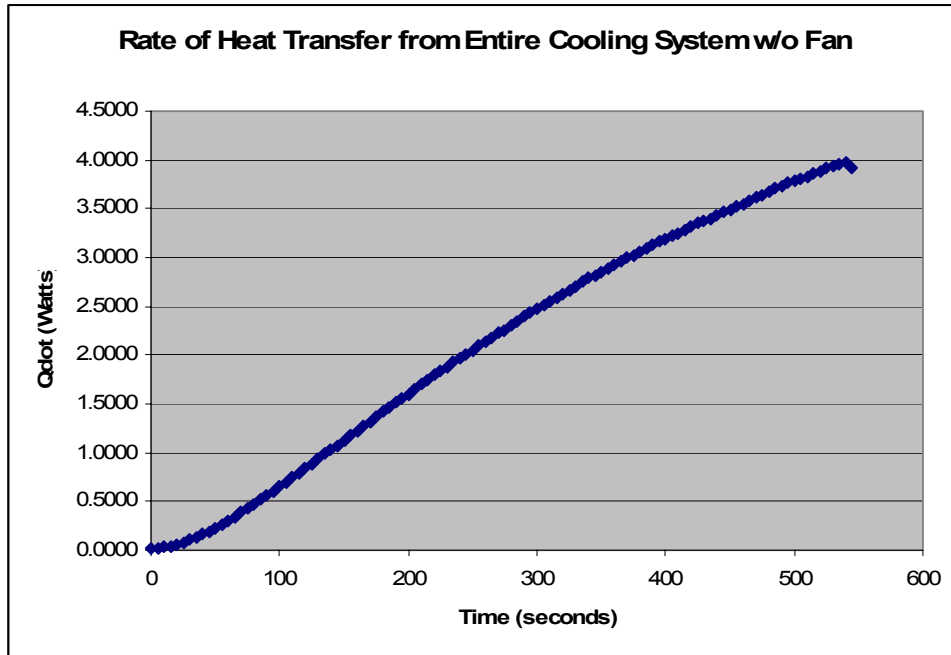


Figure 2.19: Rate of Heat Transfer during Processor Heating

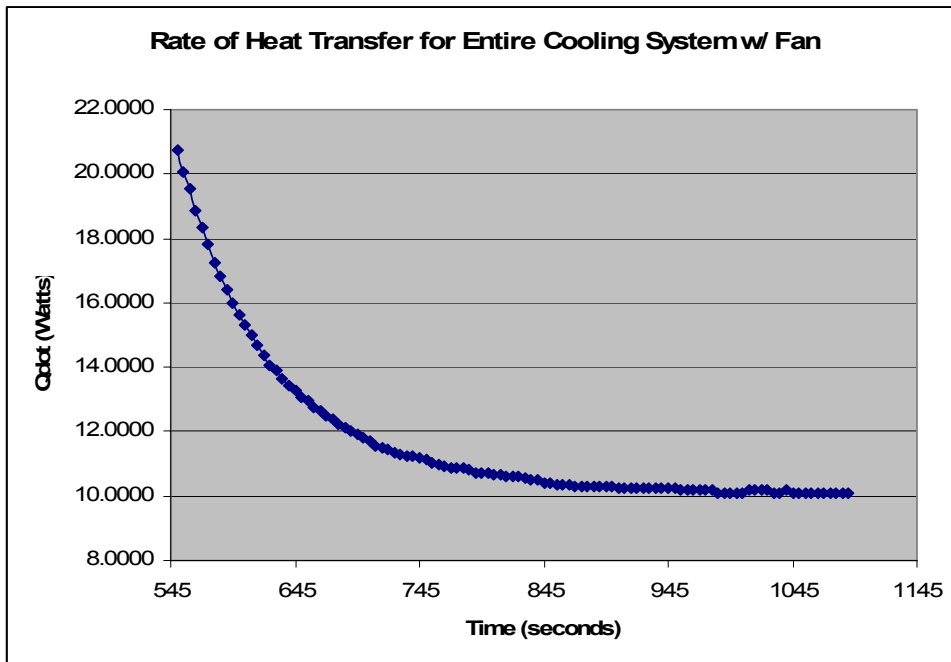


Figure 2.20: Rate of Heat Transfer during Processor Cooling

It can be seen from Figure 2.19 that the rate of heat transfer is steadily increasing as the processor reaches the maximum temperature before the fan goes on. While the rate of heat

transfer appears to be almost linear it does in fact have a slight curvature. This is expected because the system should increase asymptotically to a steady state rate when the system reaches thermal equilibrium. Since this equilibrium is higher than the processor can handle, a fan is used.

Figure 2.20 shows that once the forced convection begins the rate of heat transfer increases 5 times. As the processor begins to cool the transfer rate begins to decrease asymptotically until it reaches a steady state value of approx. 10 Watts. This shows that the system now reaches thermal equilibrium within the limits of the processor. Accordingly it appears that the processor outputs about 10 Watts performing a full load of operations.

2.1.3 Ansys® Simulation

An Ansys® heat transfer analysis of the Dell® Inspiron's™ cooling system was performed. The analysis looked at the steady-state rate of heat transfer from the copper plate, heat sink and overall system. The copper plate, heat pipe and heat sink were modeled using SOLID70 elements with the element length determined based on the Ansys® 'smart size' feature (figure 2.21).

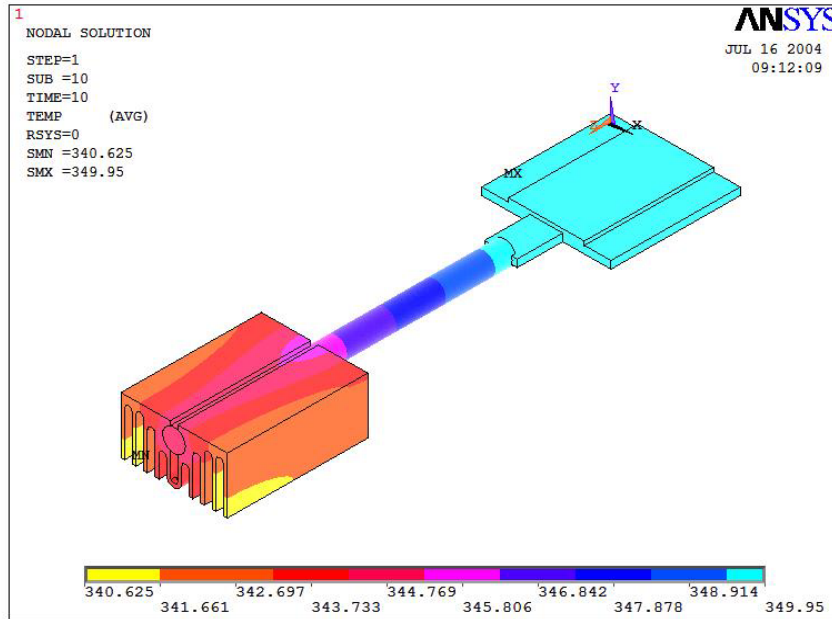


Figure 2.21: Steady-state Temperature of Cooling System

Three DOF constraints were applied to the system. They are the natural convection from the surface of the copper plate, the forced convection through the heat sink, and a constant temperature of applied to the bottom of the copper plate. The material characteristics of the heat pipe can be seen in Table 2.3. The thermal conductivities of the copper plate and aluminum heat sink were considered to be 401 W/m °C and 237 W/m °C respectively.

Thermal conductivity (k)	11960 W/m°C
Density	3395 kg/m ³

Table 2.3: Properties of Heat Pipe

The constant applied temperature (76.8°C) and the convection coefficients for the natural ($h = 9.45 \text{ W/m}^2 \text{ °C}$) and forced ($h = 72.32 \text{ W/m}^2 \text{ °C}$) convections were obtained from the analytical analysis where the rate of heat transfer reached steady state (figure 2.8 and 2.13). Figures 2.22 and 2.23 display the steady-state results for the heat flux through the copper plate and heat sink. The rate of heat transfer can be determined from $\dot{Q} = \dot{q}_s A$ where \dot{q}_s is

the heat flux and A is the cross-sectional area. For the copper plate, A is the top surface area (0.001156 m^2) and for the heat sink, the cross-sectional area of a fin ($3.7 \times 10^{-5} \text{ m}^2$). Since the heat flux through both the copper plate and heat sink is variable, as seen in the below figures, an average was obtained for each component. The heat flux for the copper plate and heat sink is 536 W/m^2 and 29540 W/m^2 respectively.

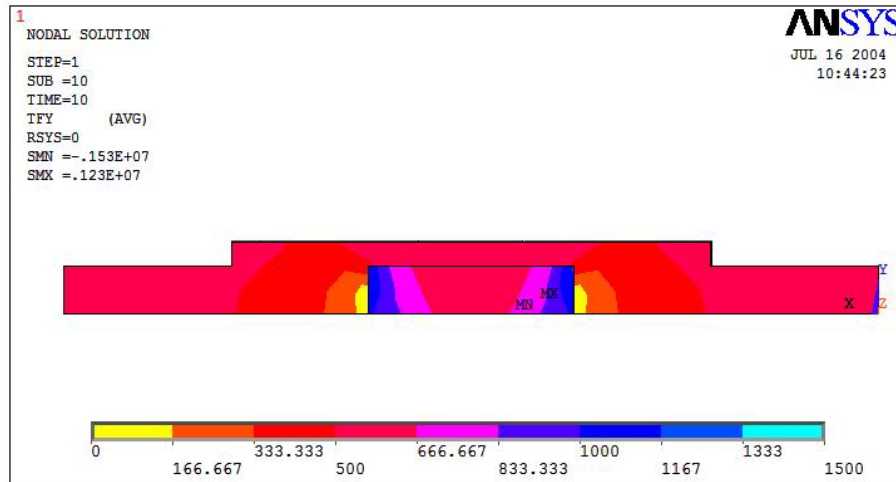


Figure 2.22: Heat Flux through Copper Plate

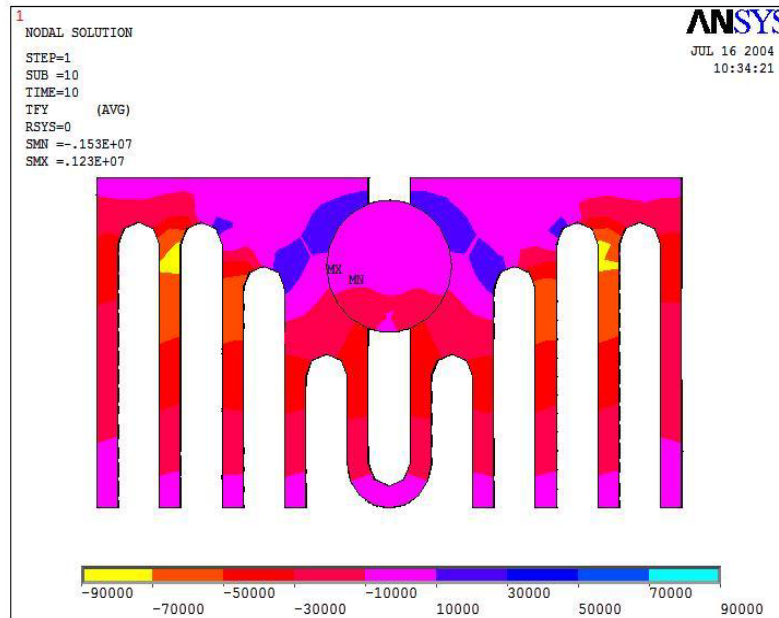


Figure 2.23: Heat Flux through Heat Sink

2.1.4 Intel® Thermal Dissipation Power (TDP) Ratings

Intel® publishes Thermal Dissipation Power (TDP) ratings for each of the processors that it produces. This rating is the amount of power that a cooling or heat removal system must dissipate from the processor for safe operation. Figure 2.24 displays typical ratings for several of Intel's® Mobile Celeron® processors. The TDP for typical operation of the Mobile Celeron® 600MHz processor is 13 Watts [6]. It can be noticed that the TDP of the processor currently being studied is significantly less than the processors that are now being used in notebook computers.

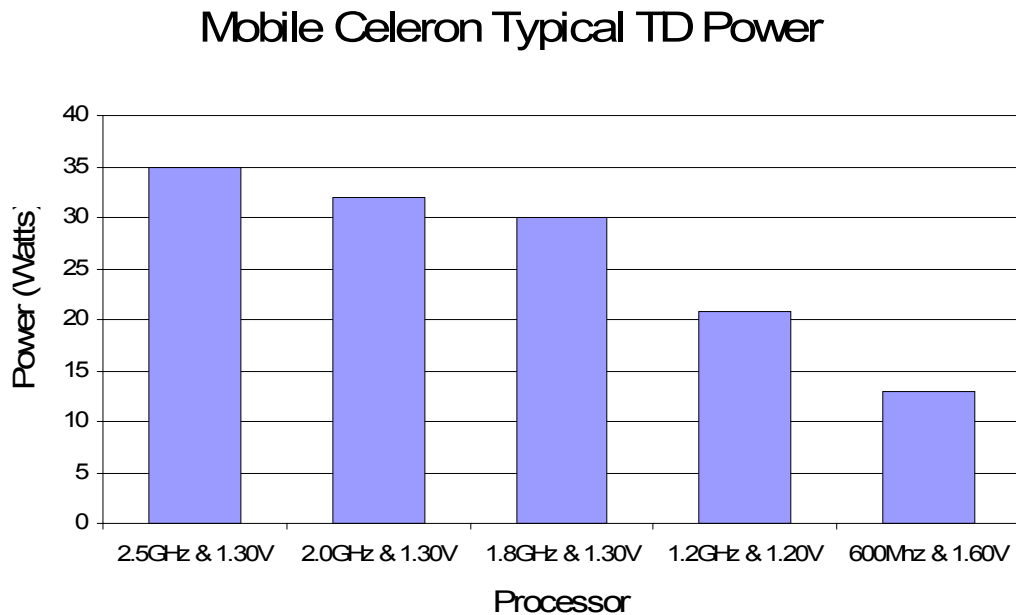


Figure 2.24: Mobile Celeron® Thermal Dissipation Power Ratings

2.1.5 Rate of Heat Transfer Comparison

The Ansys® steady-state results (figures 2.22 and 2.23) are compared to the steady-state analytical results (figures 2.19 and 2.20) in Table 2.4 with the resulting error.

	<i>Ansys® Heat Transfer</i>	<i>Analytical Heat Transfer</i>	<i>Error</i>
<i>Copper Plate</i>	0.62 W	0.61 W	1.6%
<i>Heat Sink</i>	10.93 W	9.49 W	13.2%
<i>Total</i>	11.55 W	10.1 W	12.5%

Table 2.4: Ansys® vs. Analytical Rate of Heat Transfer

From the above table it can be seen that the error in the copper plate analysis is very low mainly due to its simplicity. The error that exists is most likely do to the fact that in the analytical analysis the plate was assumed to be a constant thickness of 3mm whereas in reality and in the Ansys® analysis half of the thickness in the middle of the plate is actually taken up by the heat pipe which has a much higher thermal conductivity.

Since a heat sink is a more complex system, the error came out to be larger. The error in the heat sink analysis is a result of the assumptions made about the heat coming into the heat sink. The analytical analysis assumed that there was a uniform temperature across the base of the heat sink that was measured with a thermocouple (figures 2.9 and 2.10). In the actual cooling system, however, the temperature is concentrated along the cylindrical surface of the heat pipe that goes through the center of the heat sink (figure 2.21). In the end the two errors when combined together produce a slightly lower overall error for the entire cooling system. The remaining error in the entire system could be due to ignoring the effects of the heat pipe on the system.

When comparing the Thermal Dissipation Power rating given by Intel® with the analytical and Ansys® analyses, there is a 22.3% and 11.1% error in each of the analyses respectively. The difference between the analyses and the TDP value is most likely due to ignoring the contribution that radiation heat transfer provides to the system. While in most systems radiation is not a large contributor, it is more prevalent in a tightly packed computer system. This large error might also display the assumption that was made in section 2.1.1 concerning the aluminum plate on the bottom of the keyboard. Natural convection from the top of the copper plate does not appear to be an accurate replacement for the aluminum plate. One final possible source of error could be that the processor was not being put under a ‘typical’ full load using the program mentioned in section 2.1.1 during testing.

2.2 COOLING CAPABILITIES OF PIEZOELECTRIC BIMORPH

The cooling capabilities of a bimorph were analyzed for the first and second modes of vibration. The capabilities were looked at in terms of the volumetric flow rate and flow velocity that the bimorph could produce. The properties that need to be determined in order to find the flow rate are the bimorph’s tip deflection or amplitude and its corresponding modal frequency.

2.2.1 Physical Characteristics of Bimorphs

There were three different bimorphs which were analyzed for their cooling capabilities. The

layout of a typical bimorph can be seen in figure 2.25. Each of the bimorphs is 63.5mm long and 31.75mm wide with varying thicknesses. The three bimorphs, which are labeled 5A, 5H and SS, are X-poled and have sputtered nickel electrodes. The bimorphs contain the following piezoceramic layers and middle shim.

Bimorph	Piezoceramic Material	Middle Shim
5A	5A4E	High Performance Composite
5H	5H4E	High Performance Composite
SS	5H4E	430 Stainless Steel

Table 2.5: Piezoelectric Bimorphs

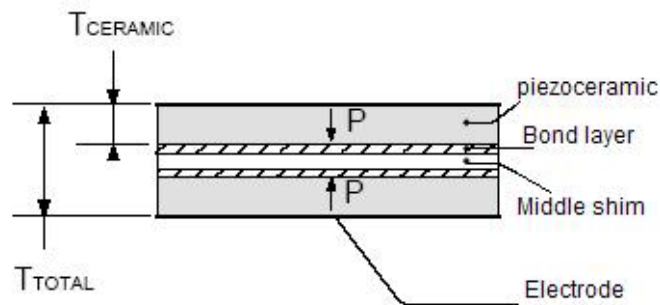


Figure 2.25: Layout of X-Poled Bimorph

The properties of the piezoceramic material, middle shims and bonding layer can be seen in the following tables [45].

Young's Modulus	$6.2 \times 10^{10} \text{ N/m}^2$
Density	7800 kg/m^3
Thickness	$1.27 \times 10^{-4} \text{ m}$

d_{31}	$3.2 \times 10^{-12} \text{ m/V}$
----------	-----------------------------------

Table 2.6: Properties of 5H4E Piezoceramic

Young's Modulus	$6.6 \times 10^{10} \text{ N/m}^2$
Density	7800 kg/m^3
Thickness	$1.27 \times 10^{-4} \text{ m}$
d_{31}	$1.9 \times 10^{-12} \text{ m/V}$

Table 2.7: Properties of 5A4E Piezoceramic

Young's Modulus	$1.9 \times 10^7 \text{ N/m}^2$
Density	1500 kg/m^3
Thickness	$1.01 \times 10^{-4} \text{ m}$

Table 2.8: Properties of Composite Shim

Young's Modulus	$2.0 \times 10^{11} \text{ N/m}^2$
Density	7750 kg/m^3
Thickness	$1.27 \times 10^{-5} \text{ m}$

Table 2.9: Properties of Stainless Steel Shim

Young's Modulus	$5.17 \times 10^9 \text{ N/m}^2$
Density	1150 kg/m^3
Thickness	$1.27 \times 10^{-5} \text{ m}$

Table 2.10: Properties of Bonding Layer

2.2.2 Bimorph Dynamic Response

Modal Frequencies

The modal frequencies of the bimorphs were determined based on an analytical model defined by equation 2.1 [46].

$$f_r = \frac{(\beta l)^2 t}{4\pi L^2} \sqrt{\left(\frac{E_p}{3\rho_p}\right) \left[\frac{1 + 3(1 + 2B)^2 + 4AB^3}{4(1 + B)^2 (BC + 1)} \right]^{1/2}} \quad (2.1)$$

where:

$$A: \frac{E_m}{E_p}$$

$$B: \frac{t_m}{2t_p}$$

$$C: \frac{\rho_m}{\rho_p}$$

$$t: t_m + 2t_p$$

E_m : Young's Modulus of middle shim

E_p : Young's Modulus of piezoceramic

t_p : thickness of piezoceramic layers

t_m : thickness of the middle shim

ρ_p : density of the piezoceramic

ρ_m : density of the middle shim

βl : from beam theory (2nd mode: 4.694091)

L : free length of bimorph

The material properties for the three bimorphs that were analyzed can be found in tables 2.5-2.10. The modal frequencies for the first and second modes can be seen in figures 2.26 and 2.27 respectively.

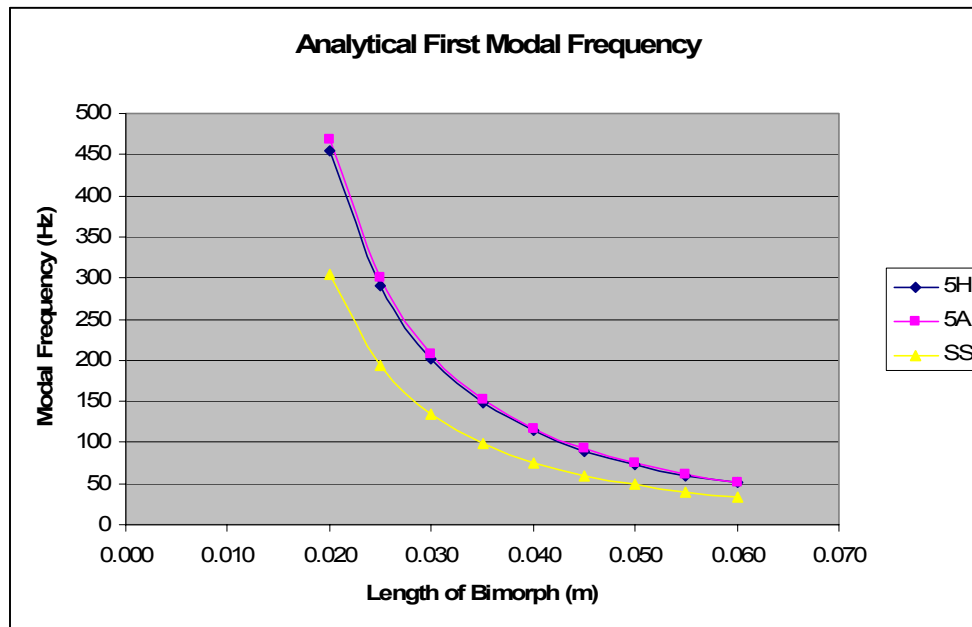


Figure 2.26: Analytical First Modal Frequencies

From the modal frequency plots, it can be seen that since the SS bimorph is thinner than the

5A and 5H bimorphs, its modal frequencies are lower. There is also a slight difference between the 5H and 5A bimorphs, which is likely due to the small difference between the Young's Modulus of their respective piezoceramic materials.

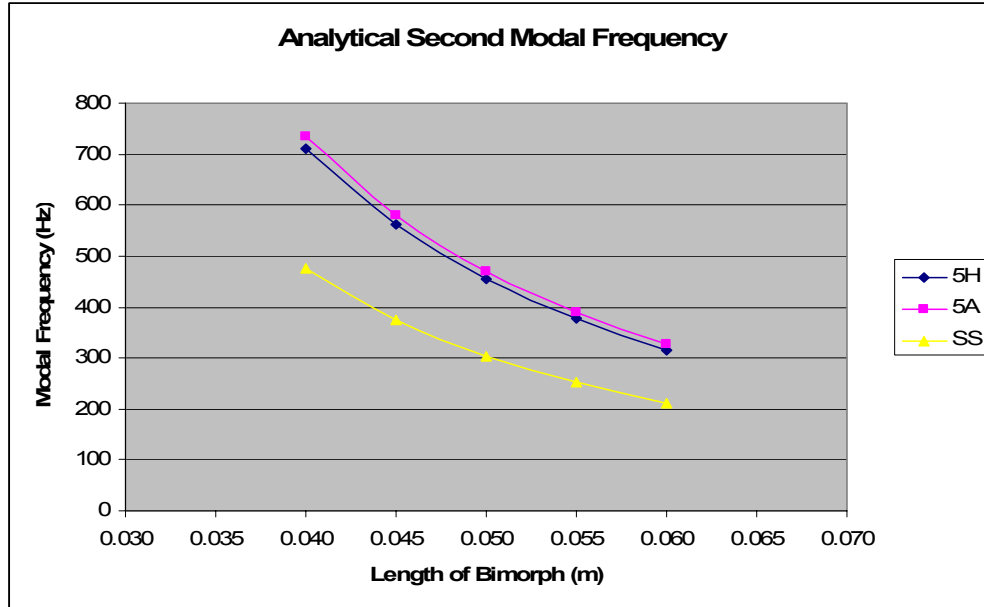


Figure 2.27: Analytical Second Modal Frequencies

Dynamic Amplitude and Tip Deflection

Since there was not available any instrumentation to measure the amplitude and tip deflection of the piezoelectric bimorphs, methods were researched to obtain this information analytically. One method to get the dynamic tip deflection is by using the following equation [47].

$$\delta = \frac{3d_{31}V \sin \Omega L \sinh \Omega L}{4t_p^2 \Omega^2 (1 + \cos \Omega L \cosh \Omega L)} \quad (2.2)$$

where:

d_{31} : piezoelectric constant

V : applied voltage

t_p : thickness of piezoceramic layer

L : length of the bimorph

$$\Omega = \sqrt{\frac{\omega}{a}} ; \text{normalized frequency}$$

ω : excitation frequency

$$a = \sqrt{\frac{EI_{eff}}{\rho A_{eff}}}$$

$$\rho A_{eff} = 2\rho_p w_b t_p + \rho_m w_b t_m$$

ρ_p : density of piezoceramic layer

ρ_m : density of shim layer

w_b : width of bimorph

t_m : thickness of shim layer

$$EI_{eff} = 2E_p I_p + E_m I_m$$

E_m : Young's Modulus of shim layer

E_p : Young's Modulus of piezoceramic layer

$$I_p = \frac{1}{12} w_b t_p^3 + w_b t_p \left(\frac{t_p}{2} - \bar{y} \right)^2 ; \text{moment of inertia of piezoceramic layer}$$

\bar{y} : centroid position of bimorph

$$I_m = \frac{1}{12} \frac{E_m}{E_p} w_b t_m^3 ; \text{moment of inertia of shim layer}$$

The tip deflection from equation 2.2 goes to infinity at resonance. There exists a method to obtain an approximate of the resonance deflection through the use of a quality factor, Q,

which is defined as

$$Q = \frac{f_r}{f_2 - f_1} = \frac{1}{2\xi} \quad (2.3)$$

In this equation f_r , f_1 and f_2 are defined by figure 2.28, where δ_r is the tip deflection at resonance, and ζ is the damping ratio of the system. The bimorph was assumed to have a damping ratio of 2%.

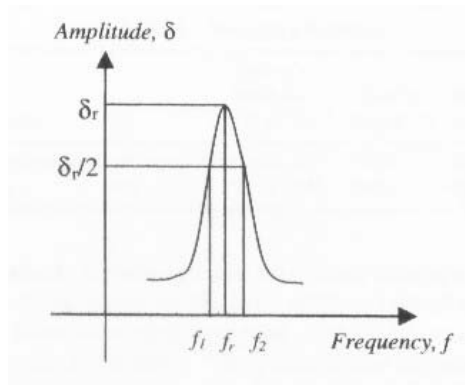


Figure 2.28: Frequency Response of Mechanical System

The dynamic tip deflection is now obtained by following the flow chart shown in figure 2.29.

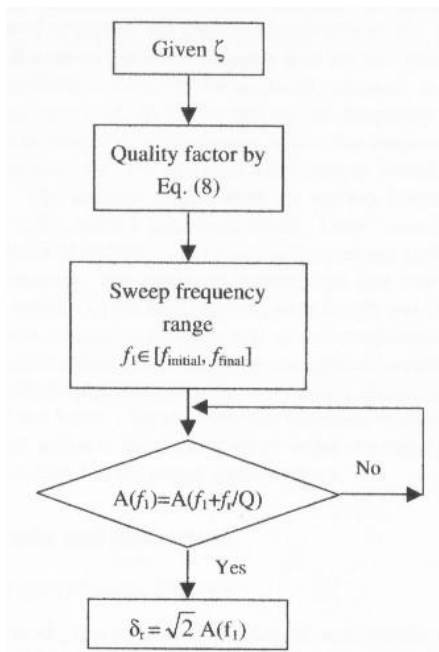


Figure 2.29: Dynamic Tip Deflection Flow Chart

Using the above method and the material properties for three bimorphs in tables 2.5-2.10, the tip deflections and amplitudes in figure 2.30 and 2.31 were obtained. In order to obtain the amplitude between the two nodes for the second mode from the tip deflection, the ratio between the two was used. The deflections shown are with an applied voltage of +/- 1V. In order to obtain the deflection at any other voltage, the amplitudes shown in Figures 2.30 and 2.31 are multiplied by the desired voltage.

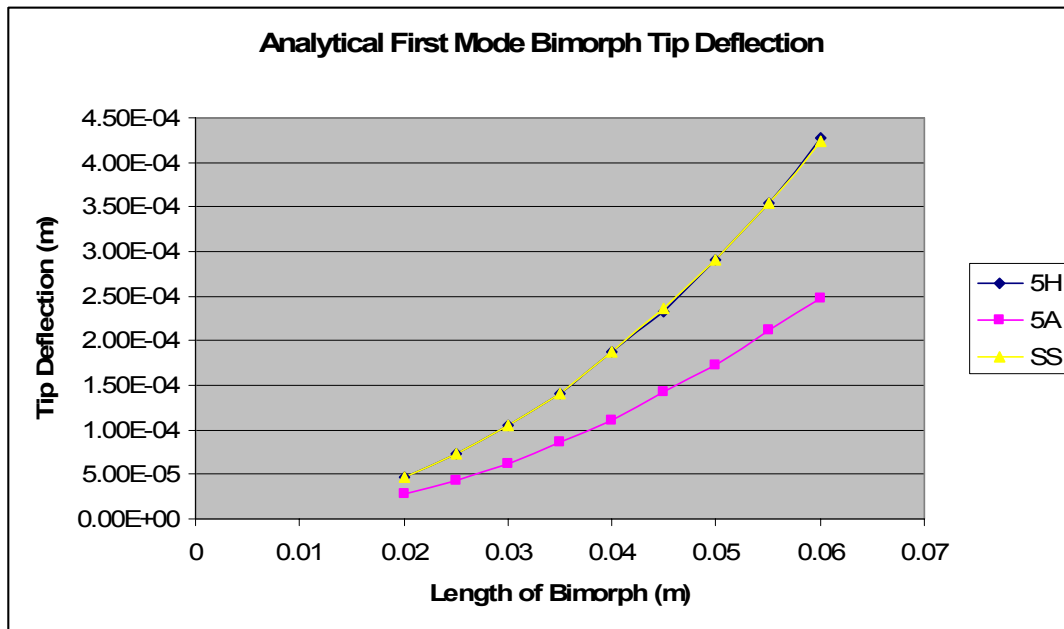


Figure 2.30: Analytical First Mode Bimorph Tip Deflection

From Figures 2.30 and 2.31 it can be seen that the 5H and SS bimorphs have exactly the same tip deflections and amplitudes. This does not appear to be an accurate representation because the bimorph have a smaller moment of inertia should have a larger deflection. However, the stainless steel shim has a higher Young's Modulus than the high performance composite shim. This could be counteracting the difference in moment of inertia. The 5A bimorph's deflections are as expected. Since the bimorph's piezoceramic material has a lower d_{31} constant than the other bimorphs, it should have a smaller deflection.

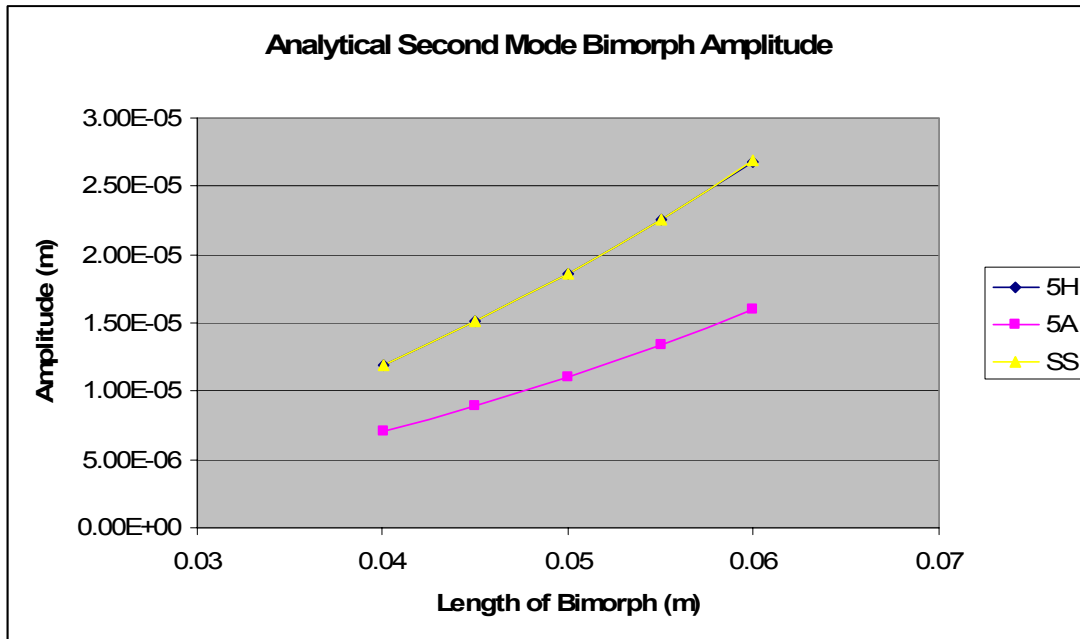


Figure 2.31: Analytical Second Mode Bimorph Amplitude

2.2.3 Ansys® Verification of Response

In order to verify the accuracy of the amplitude and modal frequency information obtained above, Ansys® simulations were performed. The bimorph was modeled as a five-layer beam consisting of two piezoelectric layers, two bonding layers and the middle shim using SOLID45 and SOLID5 elements (figure 2.25). Only one quarter of the bimorph was modeled through symmetry. Asymmetric loading was applied through the thickness of the bimorph and symmetric loads applied through its width (figure 2.32). The element size was constrained to 0.0002 meters in order to obtain accurate results and yet limit the processing time. Harmonic analysis was then performed using a 2% damping ratio, which was chosen based on previous work [47]. The three bimorphs in table 2.5 were simulated. The

properties of the materials used that make up these bimorphs can be seen in tables 2.6-2.10.

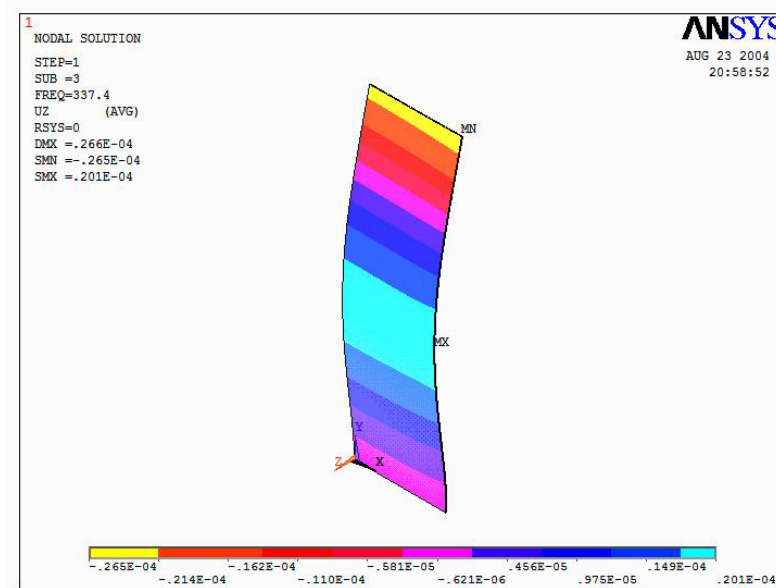


Figure 2.32: Ansys® Harmonic Response of Bimorph

Modal Frequencies

The modal frequencies of the bimorphs were found for various lengths with an excitation voltage of +/- 1V.

Figures 2.33 and 2.34 display the modal frequencies of the first and second modes of vibration. From the two figures, it is easily recognizable that the modal frequency of the 5A and 5H bimorph are essentially the same. As was previously noted this is due to the similar material properties of the two bimorphs, except for their piezoelectric constants, which have negligible effect on the modal frequency (tables 2.5-2.9). The SS bimorph has a slightly lower modal frequency because of its smaller thickness (table 2.9).

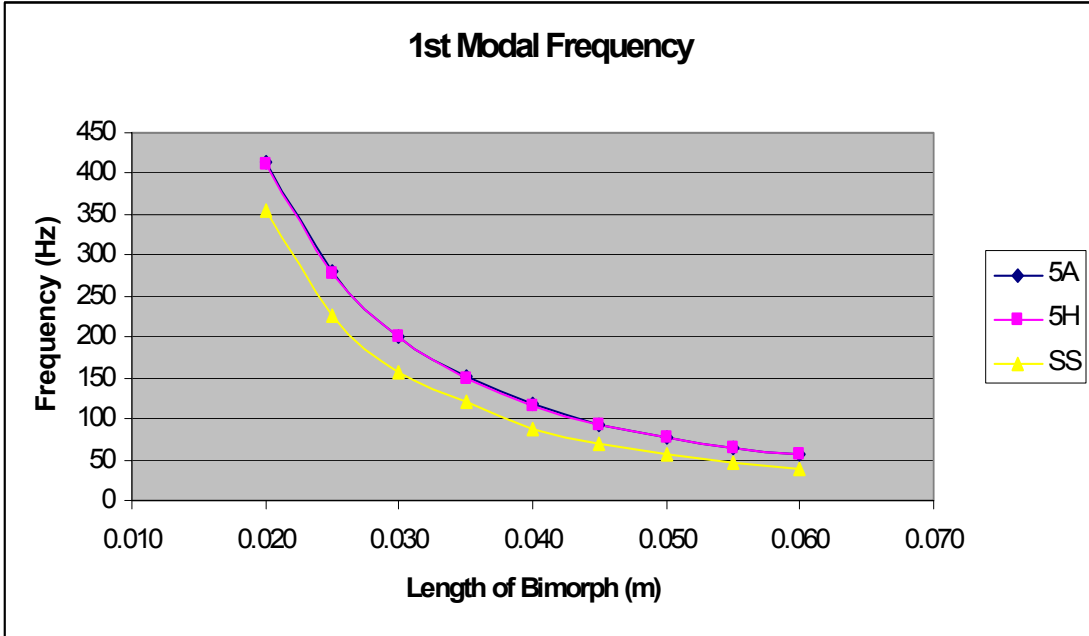


Figure 2.33: Ansys® First Modal Frequency

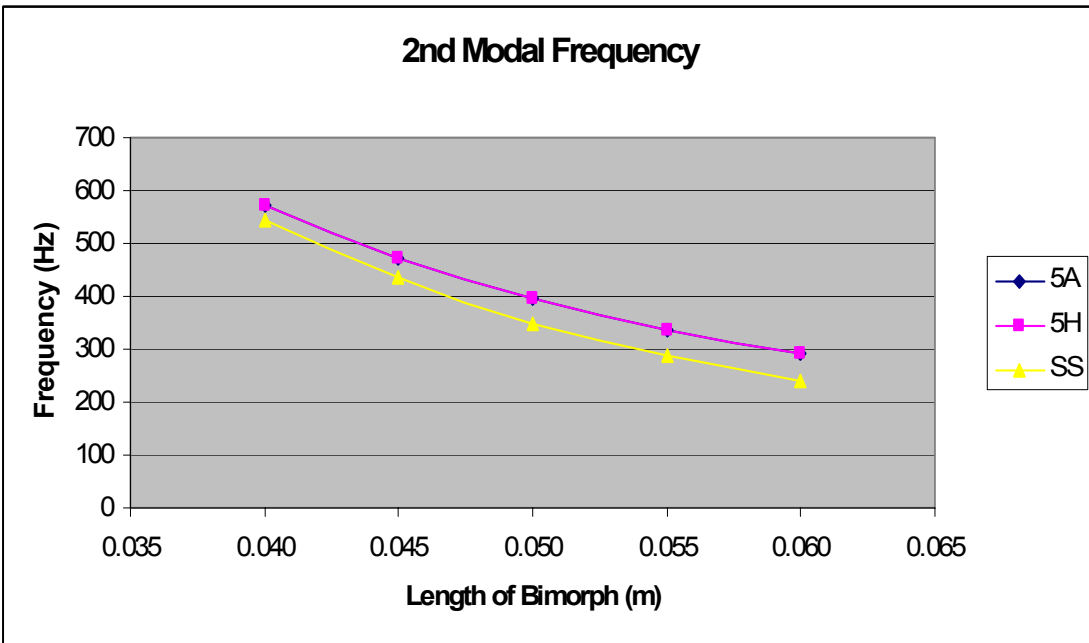


Figure 2.34: Ansys® Second Modal Frequency

Dynamic Amplitude and Tip Deflection

The deflections at the modal frequencies of the three bimorphs for different lengths can be seen in figures 2.35 and 2.36. The deflection at any other voltage can be found by multiplying the +/-1V deflection by the desired voltage.

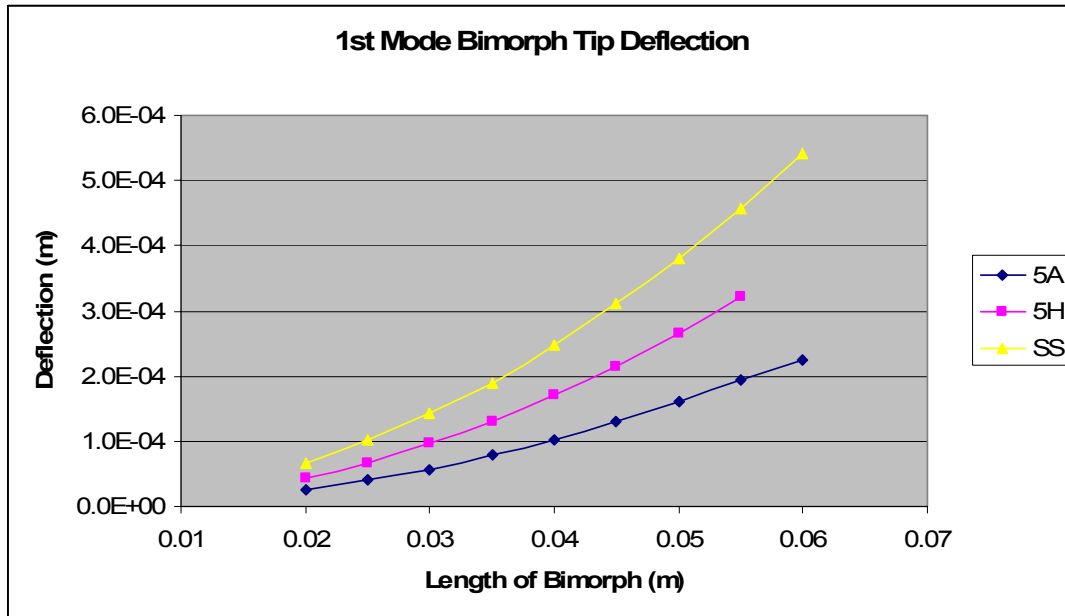


Figure 2.35: First Mode Bimorph Tip Deflection (+/-1V)

From figures 2.35 and 2.36, it can be seen that the SS bimorph has the largest deflection. The reason for this, as was mentioned before, is because this bimorph is the thinnest of the three (table 2.9). The 5H bimorph follows closely behind the SS bimorph because they are both made with the same piezoceramic material (table 2.5 and 2.6). The bimorph with the smallest deflection is the 5A bimorph. Since the material properties of the 5H and 5A bimorph are essentially the same, the reason for the smaller deflection is because of the lower d_{31} constant associated with the 5A piezoceramic material (table 2.6, 2.7 and 2.8). In fact the d_{31} constant of the 5A piezoceramic is about 41% smaller than the 5H piezoceramic, which is exactly the same difference between the deflection of the 5A and 5H bimorphs.

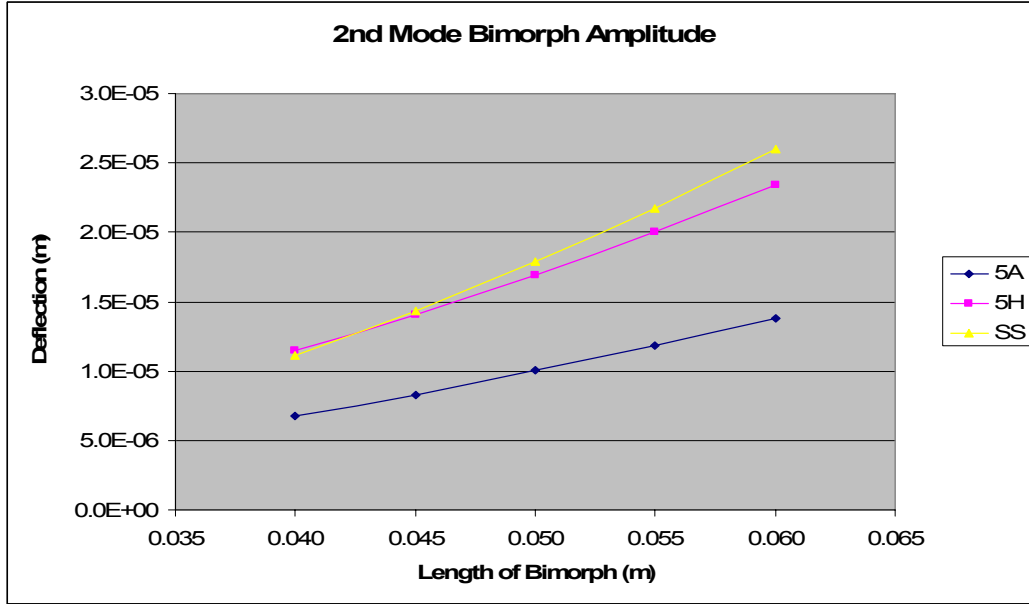


Figure 2.36: Second Mode Bimorph Amplitude (+/-1V)

Analytical vs. Ansys® Comparison

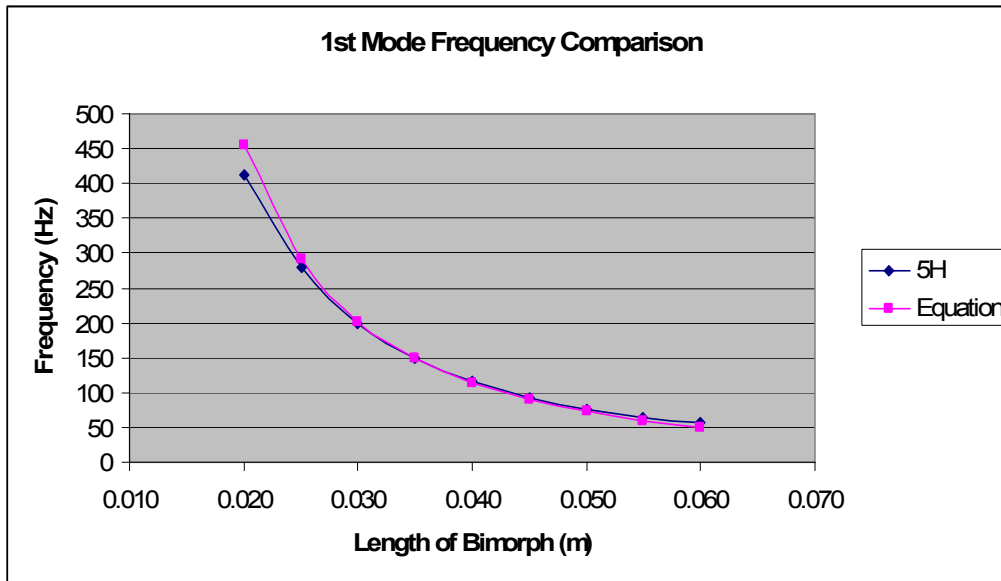


Figure 2.37: Ansys® vs. Equation 2.2 First Mode Frequency Comparison

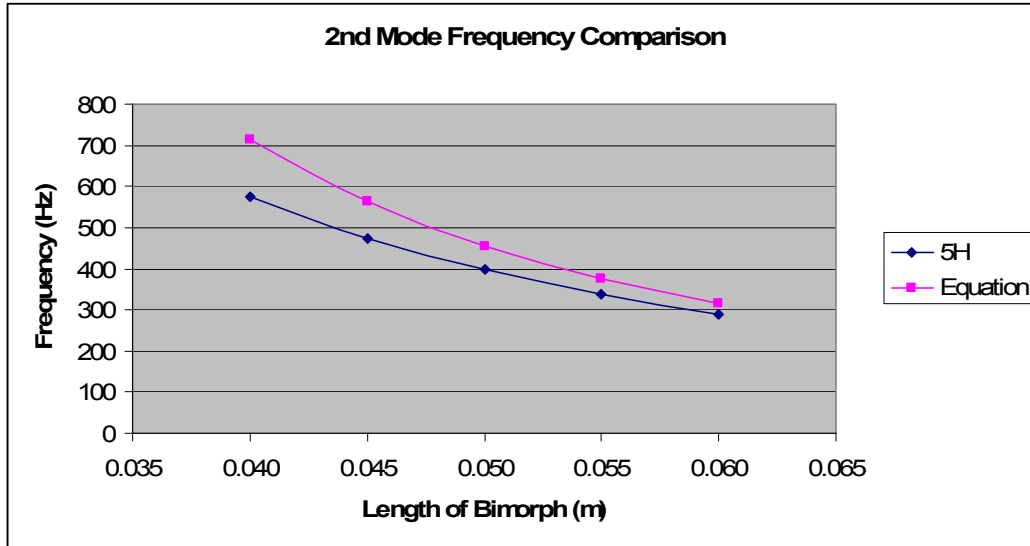


Figure 2.38: Ansys® vs. Equation 2.2 Second Mode Frequency Comparison

When comparing the first modal frequencies in figure 2.37, it can be seen that equation 2.1 is able to accurately predict the Ansys® result. However, as the bimorph becomes shorter and the resonant frequency goes up the error between the two results increases. This is most likely due to the d_{33} constant of the piezoceramic becoming more prevalent in the shorter bimorphs. The d_{33} constant is not taken into account in equation 2.1. As for the second modal frequencies in figure 2.38, the error between the two results is between 8% for the longest bimorph and 19% at the shortest length. The cause of this discrepancy is likely due to dynamics that do not show up in equation 2.1 such as internal damping.

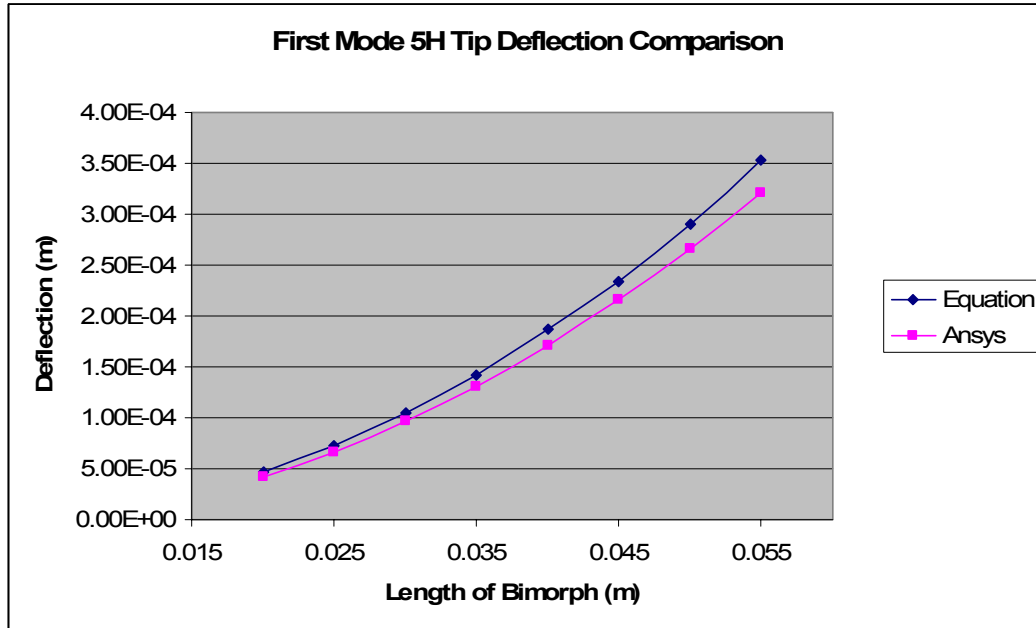


Figure 2.39: First Mode 5H Tip Deflection Comparison (+/- 1V)

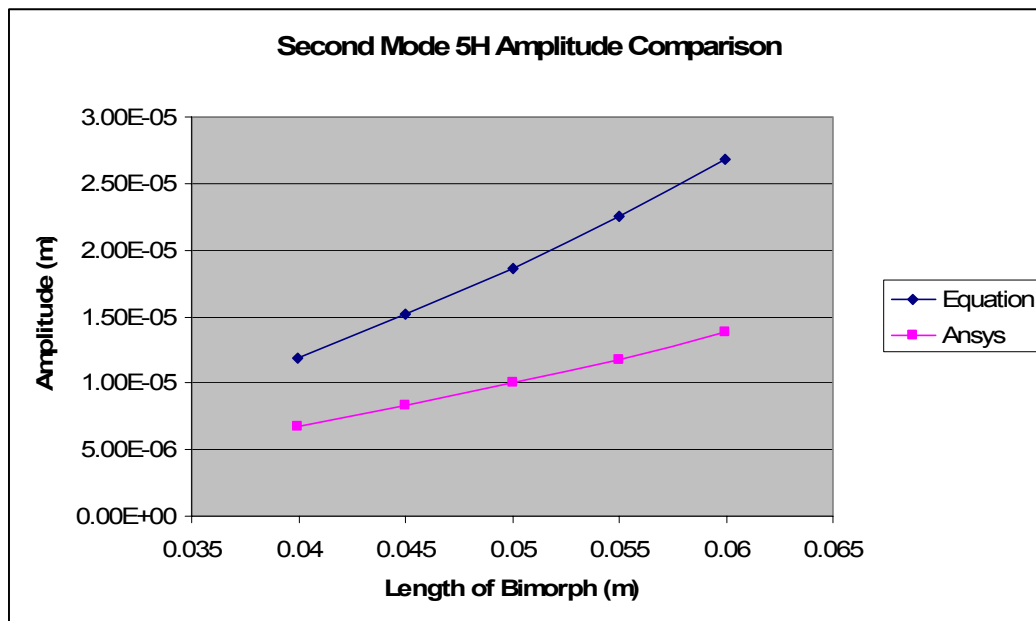


Figure 2.40: Second Mode 5H Amplitude Comparison (+/-1V)

The Ansys® tip deflection results and equation 2.2 results are compared in figures 2.39 and 2.40. In figure 2.39, it can be seen that equation 2.2 seems to follow the Ansys® results with relatively low error at the first mode. However, it should be noted that this error would be

magnified when looking at higher excitation voltages. For the second mode of vibration, figure 2.40 displays significant differences between the two results. The reason for the large increase in error is unknown.

2.2.4 Volumetric Flow Rate

In order to determine the volumetric flow rate, the volume of air displaced by the bimorph in the first and second modes had to be determined. It is known through beam theory that a single free end beam's modal shape is described by equation 2.4. The first and second mode shapes can be seen in figures 2.41 and 2.42.

$$W(x) = C[\sin(\beta x) - \sinh(\beta x) + \alpha(\cos(\beta x) - \cosh(\beta x))] \quad (2.4)$$

$$\alpha = \frac{\sin(\beta l) + \sinh(\beta l)}{\cos(\beta l) + \cosh(\beta l)}$$

where:

C : amplitude scaling factor

x : distance along the beam

l : length of the free end of beam

βl : constant dependent on mode

1st mode: 1.875104

2nd mode: 4.694091

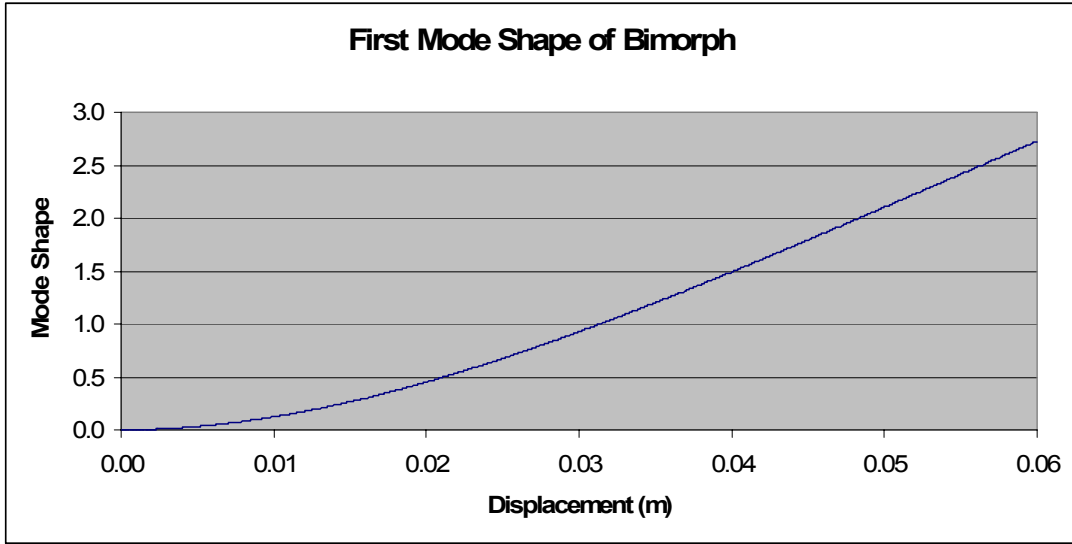


Figure 2.41: First Mode Shape of Free End Beam

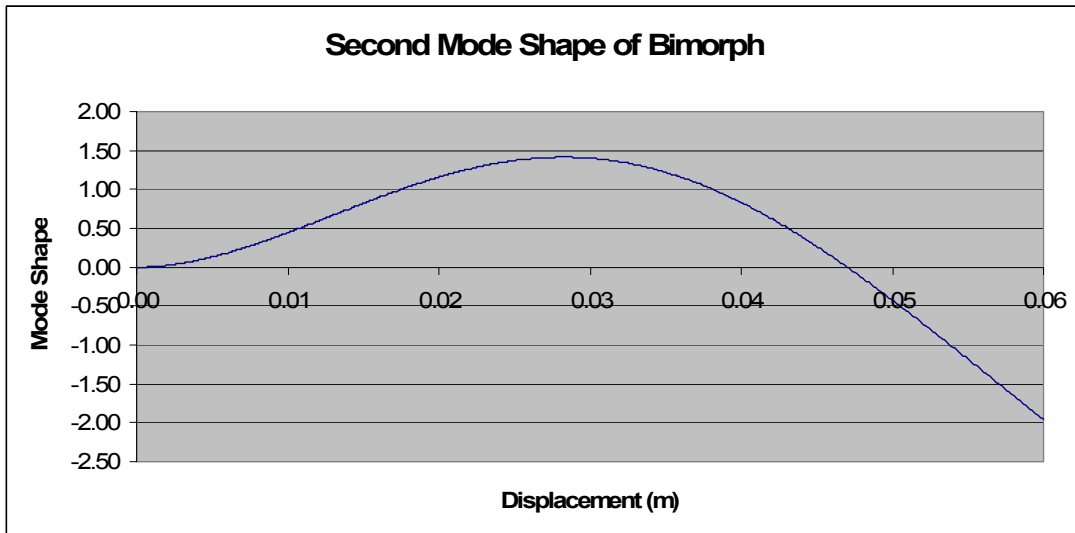


Figure 2.42: Second Mode Shape of Free End Beam

The area under these shapes can be found by integrating equation 2.4 over the length of the beam for the first mode and between the two nodes for the second mode. The volume displaced after the second node of the second mode shape will be considered insignificant compared to the area between the two nodes and therefore will be ignored. The actual area underneath the bimorph in each mode can then be derived by scaling the mode shape to the

bimorph's amplitude (2nd mode) or tip deflection (1st mode) derived from Ansys® (section 2.3). The flow rate is easily obtained by multiplying the area by the width of the bimorph (0.03175m) and its modal frequency (section 2.3). The volumetric flow rate for the first and second modes can be seen in figures 2.19 and 2.20 for an excitation voltage of +/-1V. The flow rate for any other voltage can be obtained by multiplying the +/-1V flow rate by the desired voltage.

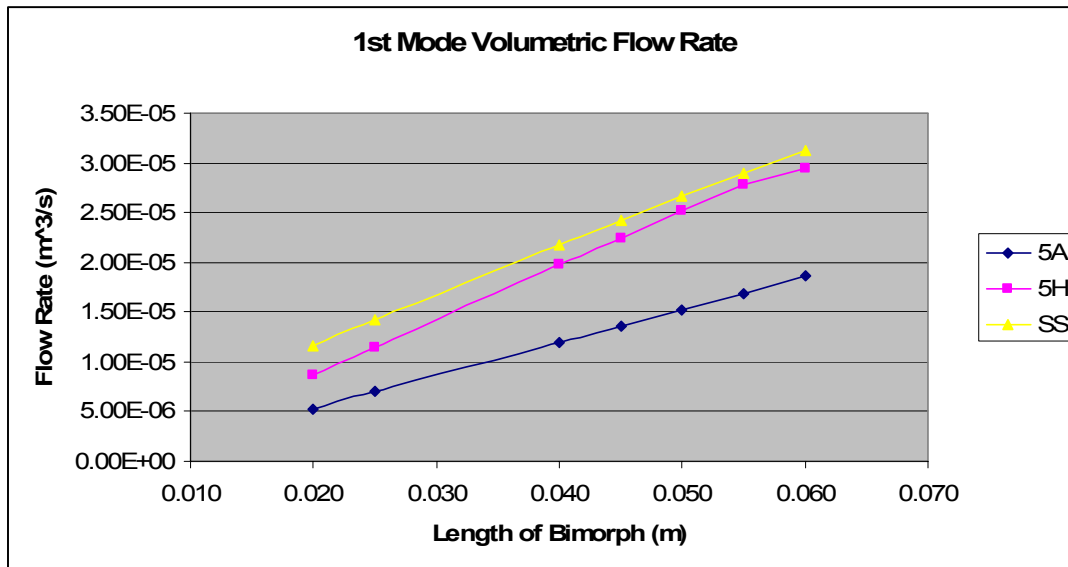


Figure 2.43: First Mode Volumetric Flow Rate (+/-1V)

From figures 2.43, it can be seen that the SS bimorph produces the highest flow rate in the first mode. The reason for this is because the SS bimorph has the largest deflection (figure 2.35). However, the 5H bimorph produces a flow rate that is relatively close to the SS bimorph. This is because the 5H bimorph has a higher modal frequency (figure 2.34), which means that even though the 5H is moving less air in one cycle than the SS, it is moving it faster. The higher frequency contribution can be seen more readily in figure 2.44 where the 5H has the highest flow rate for the second mode. The 5H over took the SS because for the second mode, the amplitudes of the two bimorphs are much closer to each other than they

were in the first mode (figure 2.36). Of the three bimorphs the 5A has the lowest flow rate for both the first and second modes due to having the smallest amplitude and tip deflection.

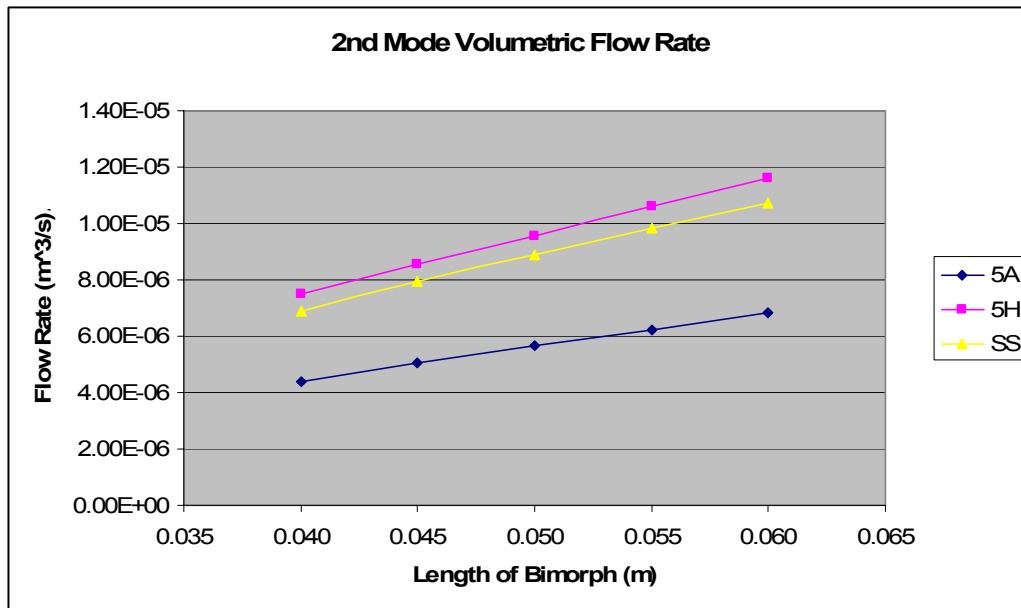


Figure 2.44: Second Mode Volumetric Flow Rate (+/-1V)

2.2.5 Flow Velocity

Once the volumetric flow rate is known the air flow velocity can be easily derived by dividing the flow rate by the exit area. However, for a vibrating bimorph beam, the exit area is dynamic. It changes as a function of the deflection over time. The minimum exit area would be when the bimorph is closest to the heat source and maximum when it is furthest away. For the first mode, half of the minimum exit area (figure 2.45) is found by taking the area of the gap between the bimorph and heat source, which is the length of bimorph times its tip deflection, minus the area under the bimorph curve found from integrating equation 2.4. Half of the maximum exit area (figure 2.46) is found by adding the area of the gap, the area underneath the bimorph curve and the end area, which is twice the tip deflection of the

bimorph times its width. The second mode minimum (figure 2.47) and maximum exit (figure 2.48) areas are found in the exact same method as the first mode except that now equation 2.4 is integrated for the second mode and the gap area is the distance between the vibration nodes times the bimorph amplitude.

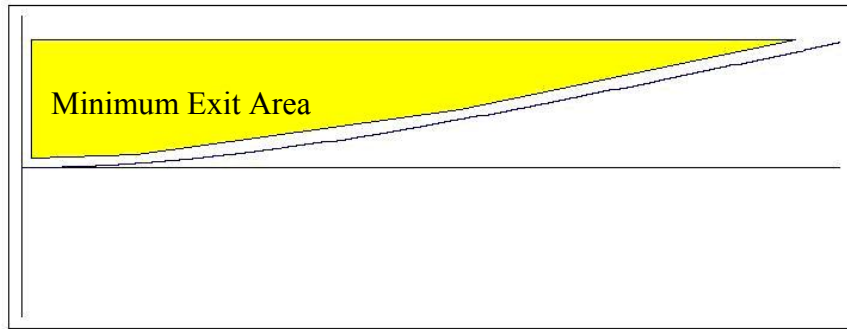


Figure 2.45: Minimum Exit Area for First Mode

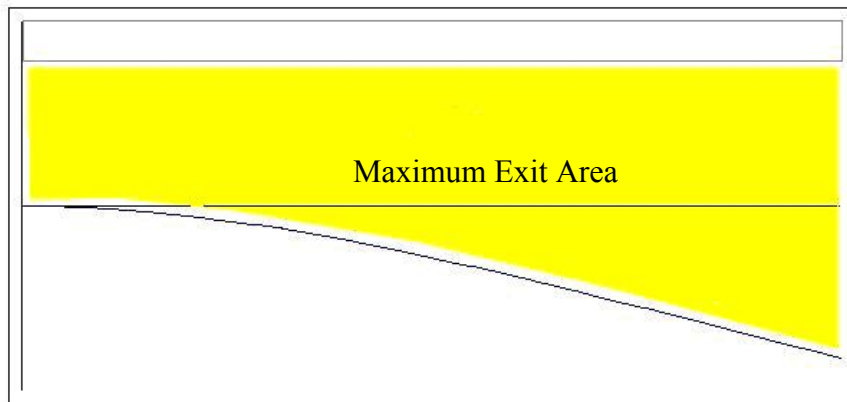


Figure 2.46: Maximum Exit Area for First Mode

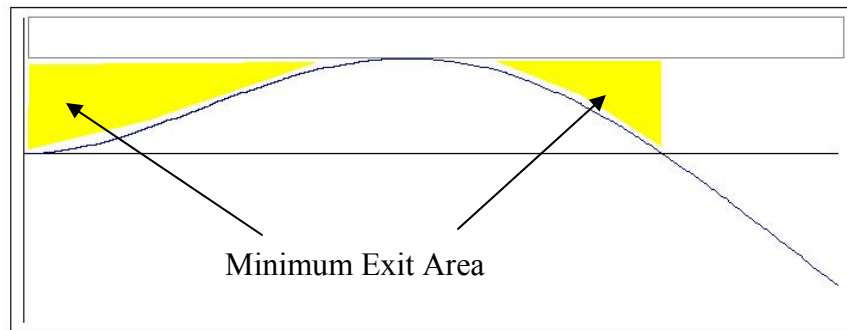


Figure 2.47: Minimum Exit Area for Second Mode

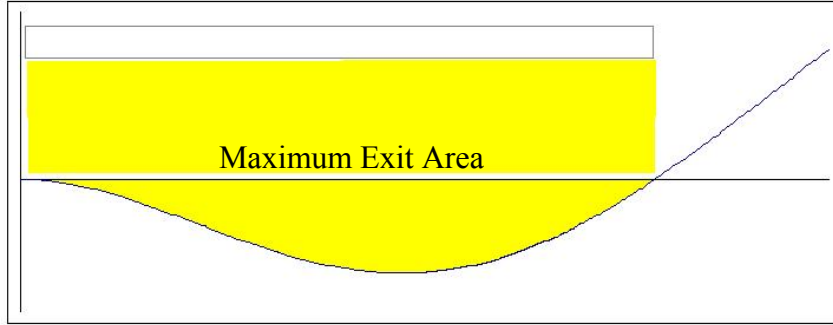


Figure 2.48: Maximum Exit Area for Second Mode

Using the known maximum and minimum exit areas the dynamic area over time can be written as equation 2.5. The flow velocity is then, as mentioned before, just equation 2.6.

$$A_{exit} = 2(l_b x_b + A_{ub} \cos(2\pi f t)) \quad (2.5)$$

where:

- l_b : length of bimorph (1st mode)
distance between nodes (2nd mode)
- x_b : maximum tip deflection (1st mode)
maximum amplitude (2nd mode)
- A_{ub} : Area under bimorph (integrating equation 2.3)
- f : modal frequency

$$v_{flow} = \frac{\dot{V}}{A_{exit}} \quad (2.6)$$

When equations 2.5 and 2.6 are combined, it can be noticed that the flow velocity is independent of the amplitude of vibration, but is mainly dependent on the modal frequency.

A comparison of the three different bimorph flow velocities can be seen in figure 2.49. It can be seen that the 5A and 5H bimorphs have the same velocity profiles and are in phase

because they have the same modal frequencies. The SS bimorph, which has the lowest frequency, also has the lowest flow velocity and lags behind the other two bimorphs in terms of when its peak velocity occurs.

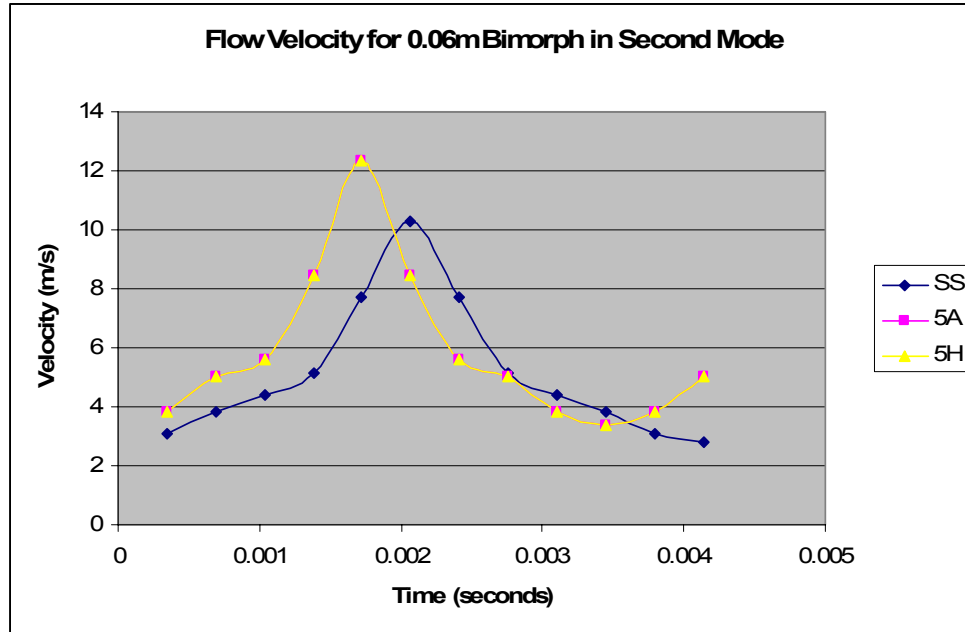


Figure 2.49: Flow Velocity Profile of Bimorphs

The maximum flow velocity for the first and second modes can be seen in figure 2.50 and 2.51 respectively. When these figures are compared to the frequency plots in figures 2.33 and 2.34, it can be seen that the flow velocity follows exactly the same trend as the frequency that was noted previously. If the amount of cooling provided by a bimorph is considered to be only dependent on the flow velocity, then the data below says the shorter the bimorph and vibration in the second mode the more cooling. Of course, there is a limit to this because as the bimorph's length goes to zero the flow velocity will go to infinity.

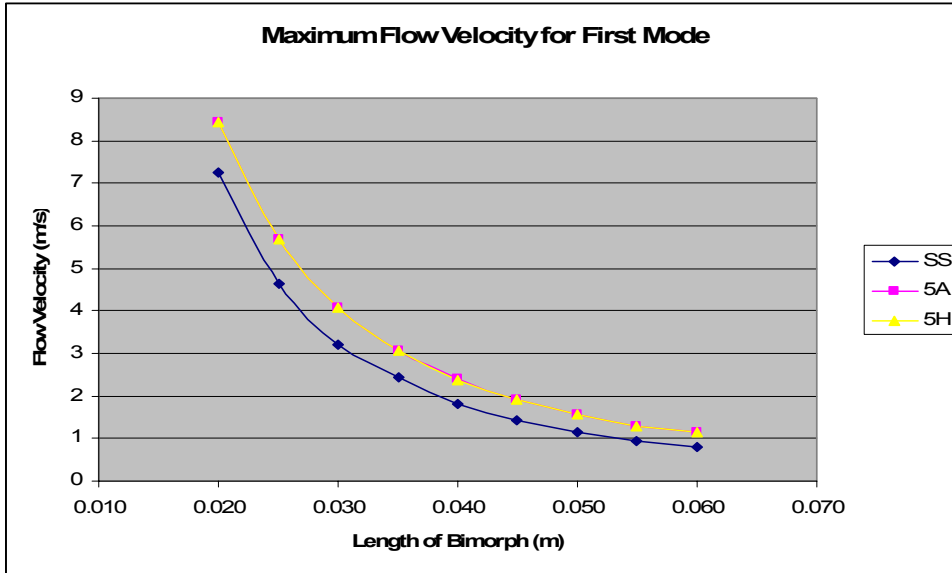


Figure 2.50: Maximum Flow Velocity for First Mode

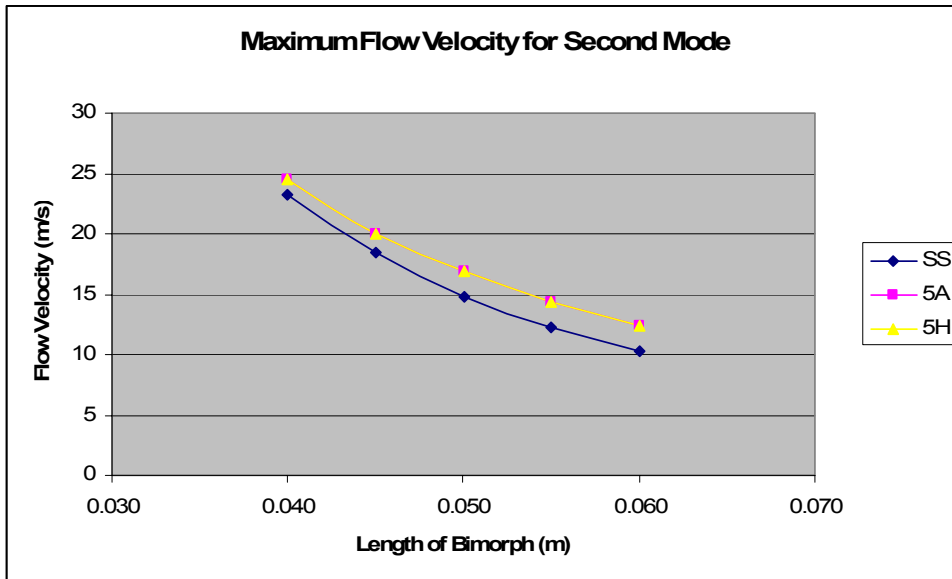


Figure 2.51: Maximum Flow Velocity for Second Mode

CHAPTER 3

TEMPERATURE PROFILE PREDICTION

3.1 Power Resistor System

A power resistor system was analyzed since the power output of the system can be easily regulated. The system, which can be seen in figure 3.1, basically consists of a heat source that is setup to be cooled by bimorph beam.

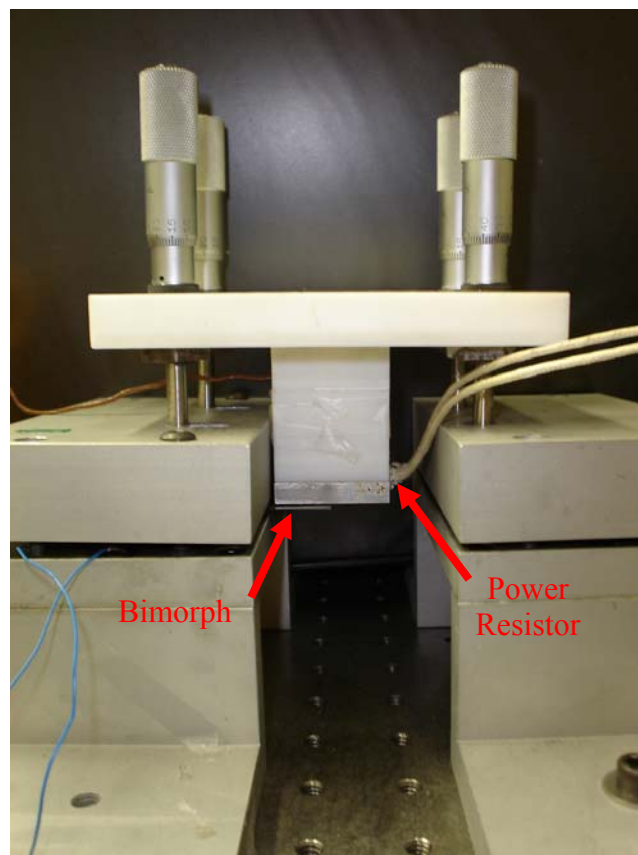


Figure 3.1: Power Resistor Cooling Physical Setup

The heat source is an aluminum plate with a cylindrical power resistor inserted into it (figure

3.2).

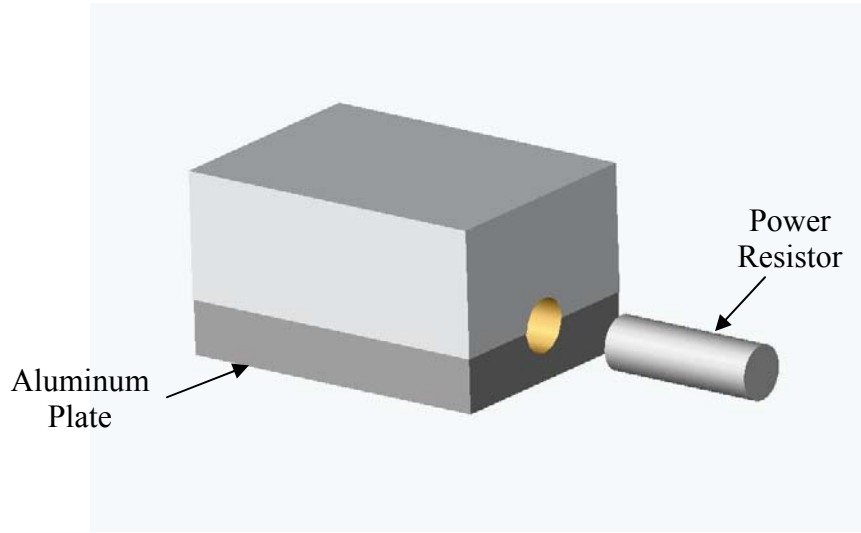


Figure 3.2: Power Resistor Setup Heat Source

The properties of the aluminum plate and power resistor can be seen in Tables 3.1 and 3.2.

Specific Heat (C_p)	875 J/kg · K
Thermal Conductivity (k)	W/m · K
Density (ρ)	2770 kg/m ³
Dimensions	35.5x25.5x6.5mm

Table 3.1: Properties of Aluminum Plate

Resistance	180 Ohms
Maximum Power Output	75 Watts
Radius	3mm
Length	30mm

Table 3.2: Properties of Power Resistor

Voltage is applied across the resistor using a KEPCO Voltage Regulator, which has a maximum output of 45V. The temperature of the aluminum plate is measured using a FLUKE® 80PK-1 bead thermocouple embedded in the aluminum and a FLUKE® 84II Series thermometer. The thermocouple has a range of 0-260 °C with an accuracy of +/- 1.1 °C. The FLUKE® thermometer displays the temperature as a digital reading with 0.1 °C precision. The gap between the bimorph beam and heat source is adjustable using four micrometers.

The temperature profile of the heat source without forced cooling due to a bimorph can be seen in figure 3.3. If this profile can be predicted, then the forced cooling profile should also be predicted because it will only change the convection portion of the prediction. Leaving out the forced cooling initially allows the system to be more simple and easier to predict.

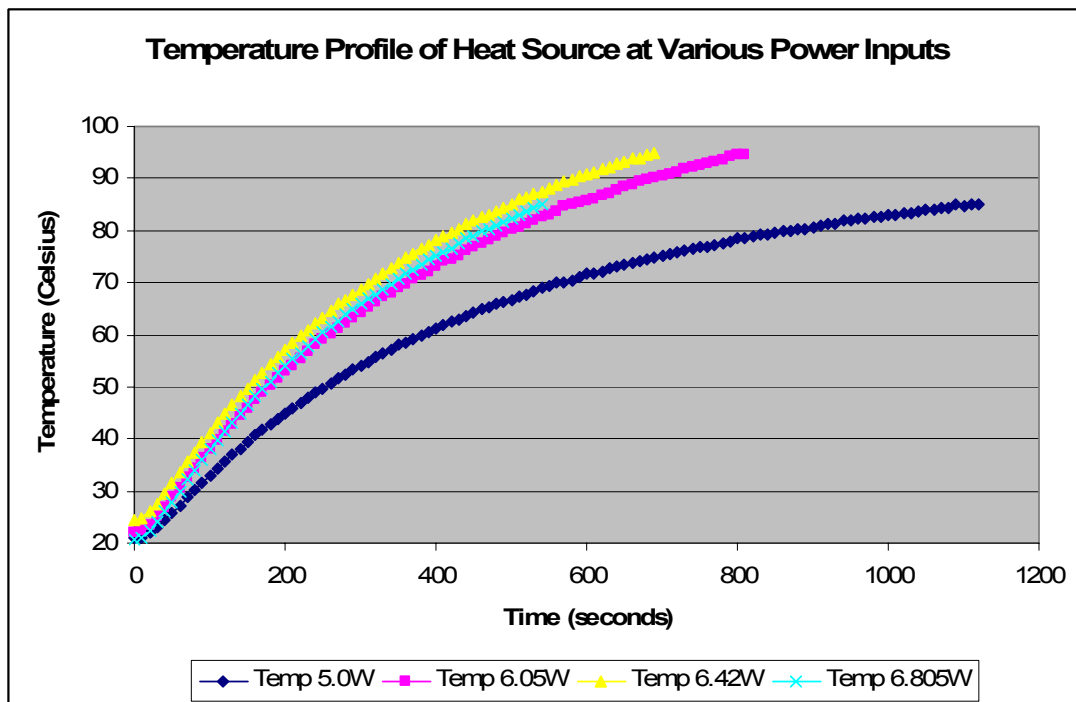


Figure 3.3: Temperature Profile of Heat Source with Various Power Inputs

3.2 Least Squares Approach

The first approach that was used to determine an equation to predict the temperature profile of the power resistor system (figure 3.3) was to perform a least squares fit of the data to a predetermined equation. Then, using the known characteristics of the system, try and derive the constants in the predetermined equation that allow for the best fit. Upon inspecting the experiment temperature data (figure 3.3), the following equation was chosen.

$$T(t) = T_0 e^{-\lambda_1 t} + A \ln(\lambda_2 t + 1) \quad (3.1)$$

Equation 1 was chosen based on the following assumptions. It was thought that during the heating process the logarithmic term would be dominate. Whereas during cooling, the decaying exponential term would become dominate. It was thought that this dominance would be primarily determined by the amount of cooling or the convection coefficient that existed in the system.

When the least squares fit was performed for three separate temperature curves at different power inputs, the constants listed in table 3.3 were derived for equation 3.1 along with the standard deviation from the experimental results.

<i>Power Input</i>	<i>T₀</i>	<i>λ₁</i>	<i>λ₂</i>	<i>A</i>	<i>Standard Deviation</i>
5.0 Watts	20.9	1/41.58	0.03	28.85	0.52
6.05 Watts	21.9	1/34	1/48.6	33	0.47
6.42 Watts	24.4	1/35	1/50.17	35.5	0.42

<i>Power Input</i>	T_0	λ_1	λ_2	A	<i>Standard Deviation</i>
6.8056 Watts	20.8	1/33.6	1/58.75	36.6	0.35

Table 3.3: Least Squares Constants

From the data it appears that as the power input into the system increases the standard deviation decreases. The reason for this is unknown. Looking at a comparison between the least squares fit and actual profile in figure 3.4 shows equation 3.5 has the largest error in prediction the logarithmic portion of the profile between 100 and 400 seconds.

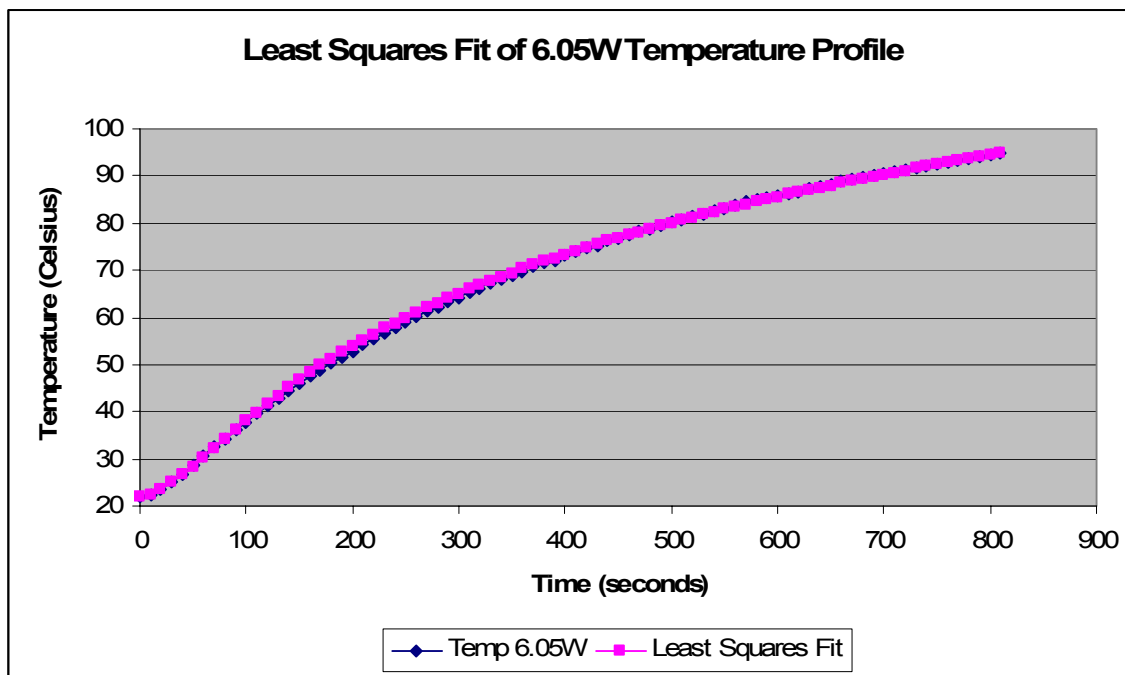


Figure 3.4: Least Squares Fit of Temperature Profile at 6.05 Watts

An attempt was made to derive the constants in table 3.3 using the known properties of the system in table 3.1 and 3.3. The properties that were used are the power input into the system, and several properties of aluminum (density, thermal conductivity, and specific heat). The convection heat transfer coefficient was also included in the derivation because it is known to be a part of the system even though its actual value is unknown. The method

used for obtaining the constants was based on the dimensional analysis. For instance, the lambda coefficients were derived to have units of 1/time thereby ensuring the exponential and logarithmic terms were dimensionless. The ‘A’ coefficient was derived to have units of temperature. However, in the end no successful combination could be found.

After further inspection of the system, it was determined that equation 3.1 can not accurately represent a thermal system because when the exponential term takes over during the cooling of the system, the system would be able to cool to a temperature lower than the ambient temperature. This could be easily remedied by changing equation 3.1 to the following equation where T_∞ is the ambient temperature.

$$T(t) = T_\infty + (T_0 - T_\infty)e^{-\lambda_1 t} + A \ln(\lambda_2 t + 1) \quad (3.2)$$

However, another flaw was found in the use of a logarithmic function in both equations 3.1 and 3.2. It was determined that a logarithmic function does not accurately portray a thermal system because the system would never reach thermal equilibrium. The logarithmic function would allow the temperature to continue to increase indefinitely.

3.3 First Law of Thermodynamics

3.3.1 Conservation of Energy Theory

The second approach that was used to predict the temperature profile of a thermal system was the 1st Law of Thermodynamics or the Conservation of Energy (equation 3.3). The system was considered to be the aluminum block in which the power resistor and thermocouple were located. Since there is no mass transfer, the system is considered closed.

$$E_{in} - E_{out} = \Delta E_{system} \quad (3.3)$$

The energy into the system would be the thermal energy from the power resistor, and the energy out of the system would be the heat transfer due to convection to the surrounding air and conduction to the plastic block to which the aluminum is attached. The change in energy of the system should then be equal to the change in the internal energy of the aluminum block. This results in equation 3.3 being transformed to equation 3.4.

$$W_{res} \Delta t - \beta(T_{Al}(t + \Delta t) - T_{\infty}) \Delta t = mC_p (T_{Al}(t + \Delta t) - T_{Al}(t)) \quad (3.4)$$

where:

W_{res} : power input from resistor

$T_{Al}(t+\Delta t)$: temperature of aluminum block at next time step

T_{∞} : ambient air temperature

$T(t)$: temperature of aluminum at current time step

C_p : specific heat of aluminum

m : mass of aluminum block

β is a constant that is dependent on the conduction and convection coefficients (equation 3.5). Since these coefficients are not known for this system, β will become the tunable variable that will allow the best fit. The accuracy of β will then be verified by using it to predict temperature plots for various power inputs.

$$\beta = hA + \frac{kA}{L} \quad (3.5)$$

where:

h : convection heat transfer coefficient

A : cross-sectional area

k : thermal conductivity

L : thickness of conductive layer

Equation 3.4 can then be rearranged to solve for the temperature of the aluminum block over time, which is seen in equation 3.6. A particular characteristic that might be noticed about this equation is that it is based on time iterations. Basically, the temperature at the next time step is based on the temperature from the previous step. The smaller the time step the more accurate the solution.

$$T_{Al}(t + \Delta t) = \frac{W_{res} \Delta t + \beta T_{\infty} \Delta t + m C_p T_{Al}(t)}{\beta \Delta t + m C_p} \quad (3.6)$$

Equation 3.5 resolves the two main problems that arose from equations 3.1 and 3.2. First, the system will now be able to reach thermal equilibrium, which can be seen in Figure 3.5. This figure represents a system that has a power input of 13W and a convection coefficient of 101 $\text{W/m}^2 \cdot \text{K}$ with no conduction present.

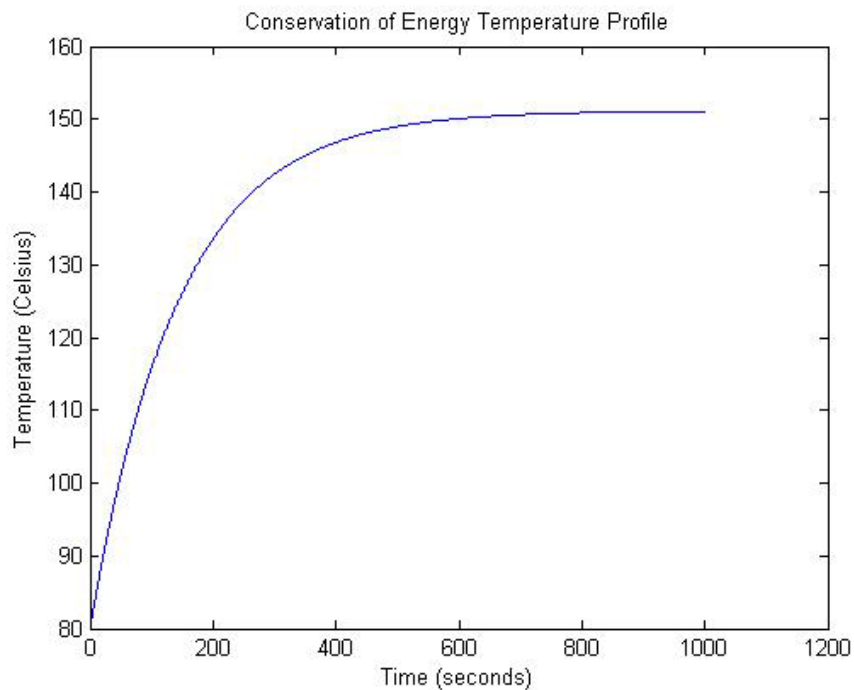


Figure 3.5: Temperature Profile Plot during Heating (13W)

The conservation of energy equation also solves the second problem that arose in equation

3.1 and 3.2. It prevents the temperature from falling below that of the ambient temperature. This can be seen in Figure 3.6 where the convection coefficient was increased ten times. The ambient temperature is 20.6°C for this system.

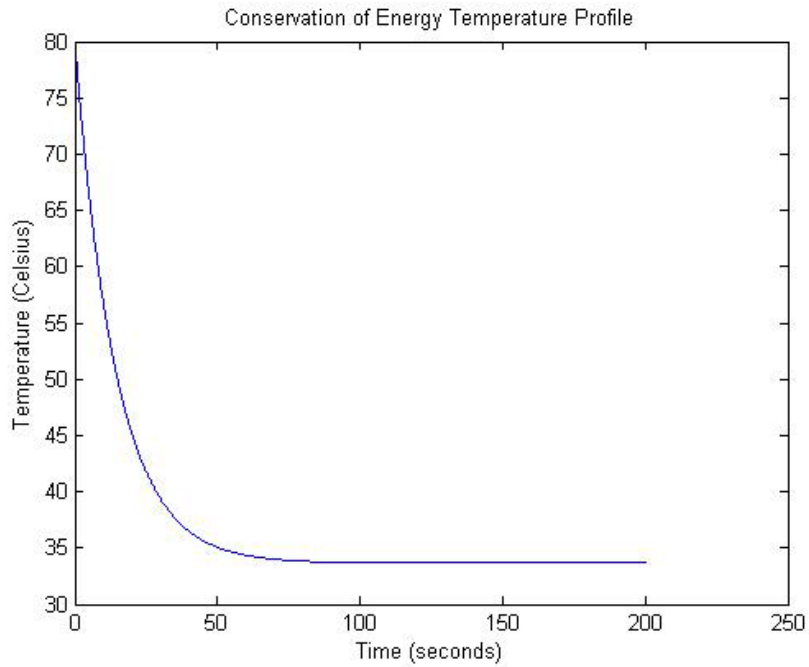


Figure 3.6: Temperature Profile Plot during Cooling (13W)

3.3.2 Temperature Profile of Power Resistor Prediction

While this method is able to get cooling and heating curves, the data does not fit very well with the experimental results (Figure 3.7). Figure 3.7 displays the temperature profile during heating with a W_{res} of 6.05W. The β term used to fit the energy equation is 0.11 W/K.

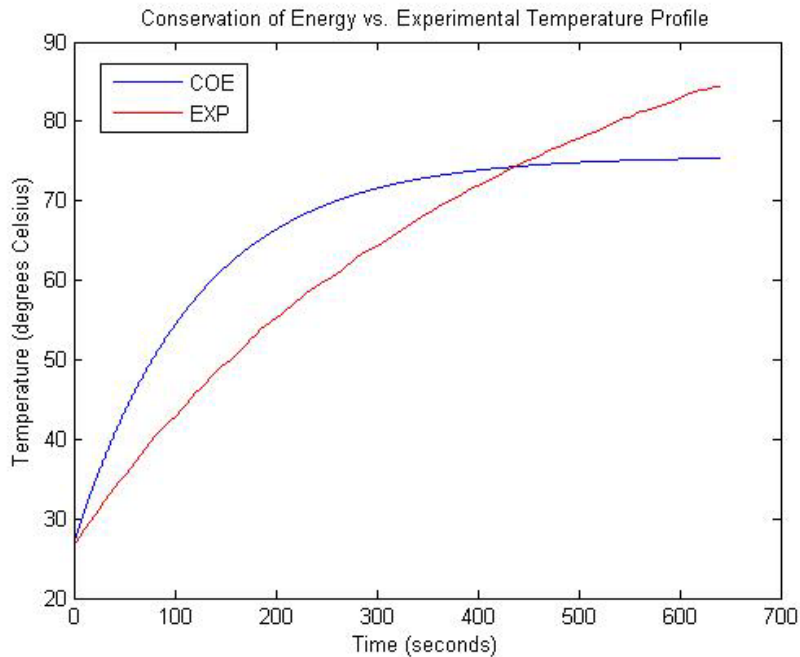


Figure 3.7: Conservation of Energy Method (6.05W)

This insinuates that some factor of energy is not being taken into account, or the energy that is being looked at is not represented accurately. One possibility is with the convection heat transfer coefficient. With natural convection this coefficient changes with temperature so as the aluminum block's temperature increases so does the coefficient as was noted in the Chapter 2 section 2.1.2. Therefore, the convection coefficient in the β term (equation 4) was substituted for a dynamic value. The thermal conductivity portion of equation 4 becomes the only tunable portion of β . The coefficient was calculated using equations 2.4 to 2.9. The characteristic length was also found in the same manner as the copper contact plate in section 2.1.2 with a value of (7.42mm). The temperature used to calculate the coefficient is from the energy equation itself, meaning that the temperature from a previous iteration of the energy equation was used to calculate the convection coefficient for the next iteration. The resulting convection coefficient values over the temperature range are seen in figure 3.8. From this figure it can be seen that the coefficient has the most change in the first 100 seconds.

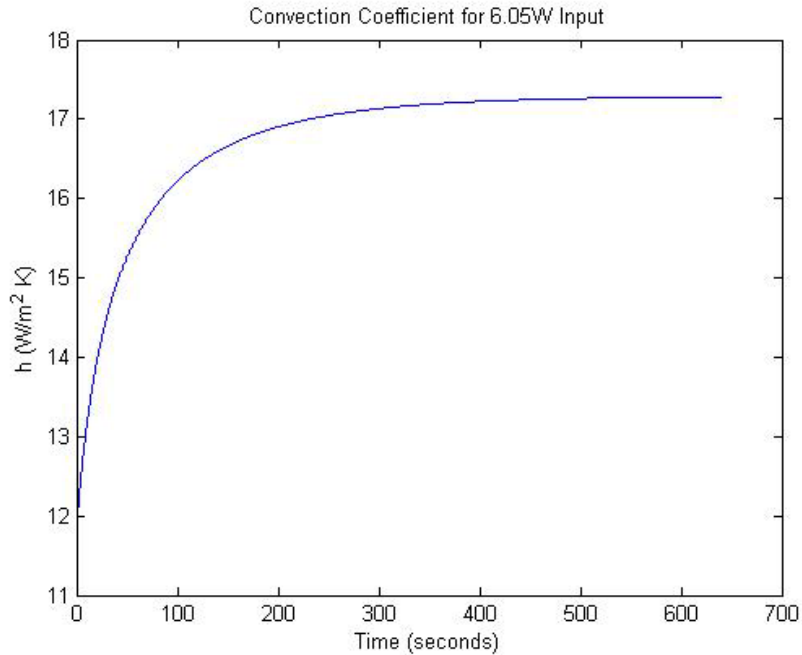


Figure 3.8: Convection Coefficient for 6.05W Input

From Figure 3.9, this change in the coefficient had very little impact on improving the energy equation fit. The thermal conductivity portion of the β term came out to be 0.095 W/K. This shows that the convection from the surface is only a small portion of the heat transfer occurring in the system. The bulk transfer appears to be due to conduction from the plastic spacer to which the aluminum plate is attached (figure 3.2).

Another more likely reason as to why the theoretical model does not match up with the experimental was determined to be due to the fact that the thermal resistor is not entirely surrounded by the aluminum block (figure 3.2). Only about half of the resistor is touching the block with the other half in contact with the plastic spacer. Due to this configuration all of the power being output by the resistor is not only going to the aluminum. With this configuration it is not known how much of the heat energy from the resistor is actually being transmitted to the aluminum plate.

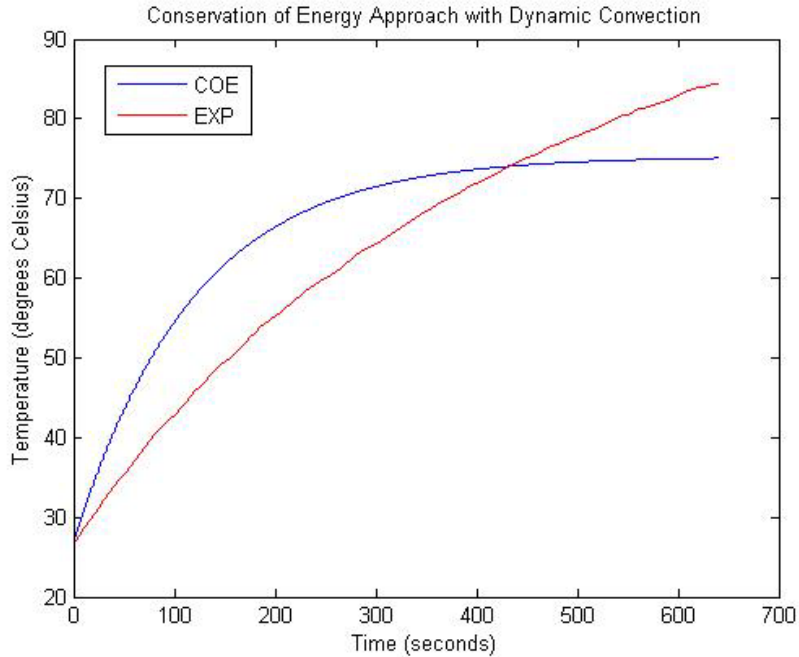


Figure 3.9: Conservation of Energy Approach with Dynamic Convection (6.05W)

This results in the creation of two unknowns in equation 3.6 (W_{res} and β). The only way to accurately obtain either of them is to obtain an equation where one does not depend on the other. The most obvious choice would be a cooling system that does not have a power input. This would result in a modified equation 3.6 to look like equation 3.7.

$$T_{Al}(t + \Delta t) = \frac{\beta T_{\infty} t + m C_p T_{Al}(t)}{\beta t + m C_p} \quad (3.7)$$

β can now be obtained by fitting equation 3.7 to an experimental cooling curve (figure 3.10). With this fit, β was found to be 0.025 W/K. It is noticeable right away in figure 3.10 that equation 3.7 does not match perfectly with the experimental data. The standard deviation for the fit is 2.01 °C. Using the new β term W_{res} can be found by refitting equation 3.6 to an experimental heating curve (figure 3.11).

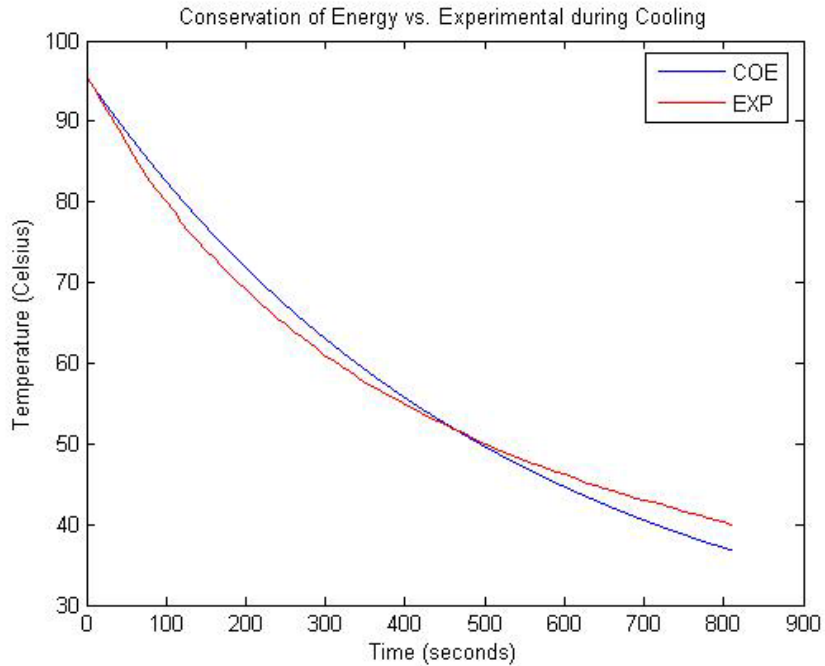


Figure 3.10: Conservation of Energy Fit to determine β

Using this method the power input into the aluminum plate was found to be approx. 2.27W, which is almost half of the total power input of the power resistor. When comparing Figure 3.8 and 3.10, it can be seen that the error between the Conservation of Energy equation and the experimental data was greatly reduced by several factors of magnitude. The standard deviation for figure 3.11 is 1.18 °C. The remaining error in the equation could be due to the convection coefficient as was mentioned earlier and perhaps to ignoring the effects of heat transfer due to radiation.

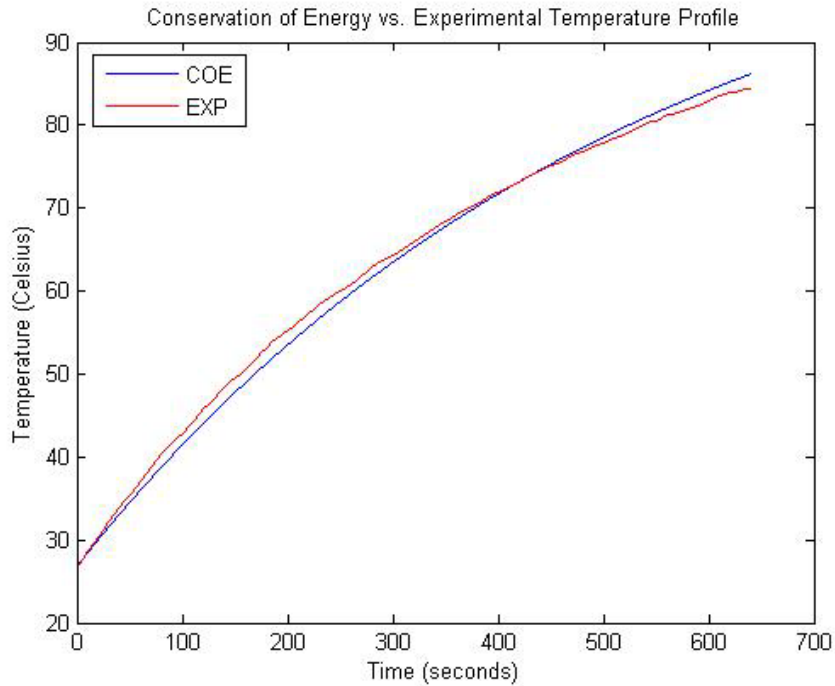


Figure 3.11: Conservation of Energy Fit to determine W_{res}

3.2.3 Temperature Profile of Celeron® Processor Prediction

Using the same setup mentioned in Chapter 2 section 2.1.1, a temperature profile of the heating of the Celeron® processor was attempted. The same method for obtaining the β and W_{res} terms were used as above. The β term was found by fitting equation 3.12 to the experimental data from the natural cooling of the processor (figure 3.12).

It is quite obvious from the figure that the conservation of energy is unable to accurately predict the processor cooling. The standard deviation of the fit is 5.86 °C.

As before, the Beta term was used to find the W term. The fit can be seen in figure 3.13. With a standard deviation of 4.2 °C, equation 3.6 is not capable of predicting the temperature of the Celeron® processor. The likely reason for this large error is because the computer

cooling system is more complex than equation 3.5. Also, it is possible that the power output of the processor was not constant but a function of time.

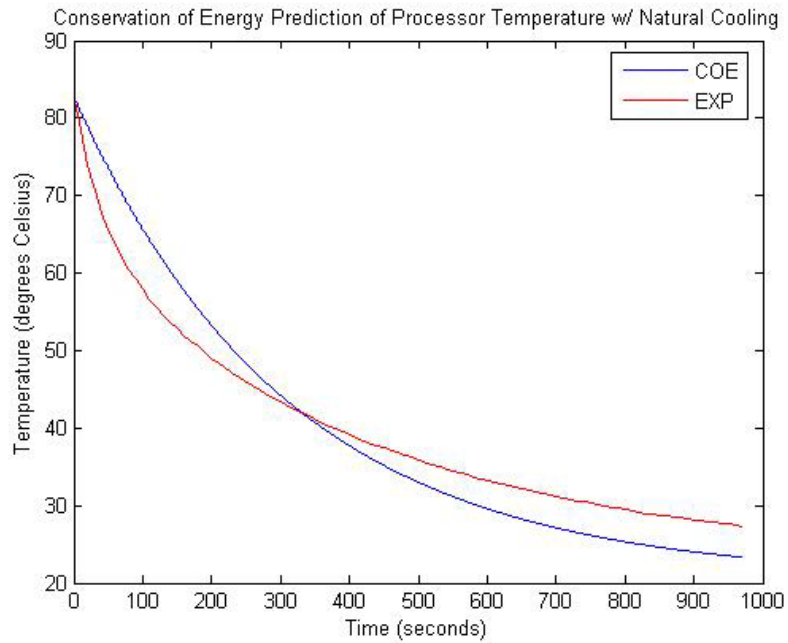


Figure 3.12: Conservation of Energy Prediction of Processor Temperature w/ Natural Cooling

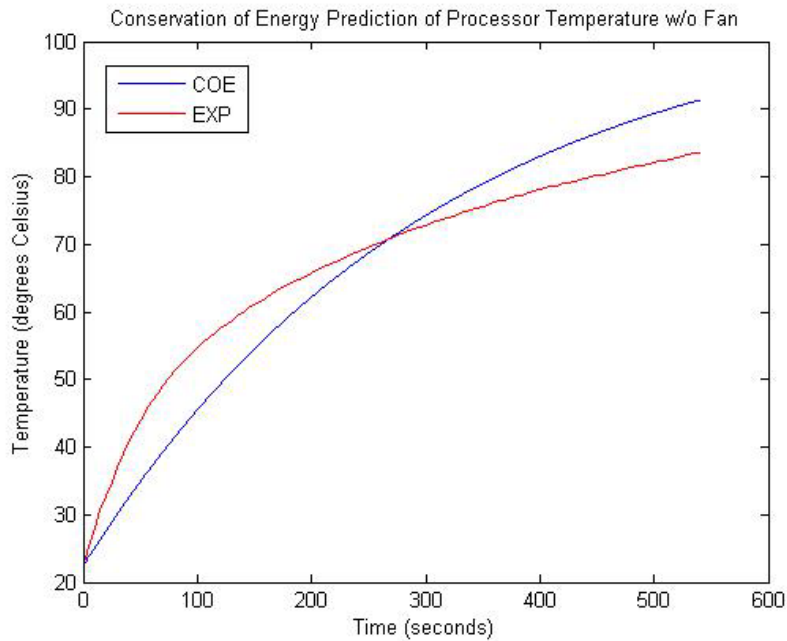


Figure 3.13: Conservation of Energy Prediction of Processor Temperature w/o Fan

CHAPTER 4

EXPERIMENTAL RESULTS

4.1 POWER RESISTOR COOLING EXPERIMENTS

4.1.1 Experimental Setup

The experimental setup mentioned in Chapter 3 section 3.1 was used to test the cooling capabilities of the bimorph. The setup for the bimorph can be seen in figure 4.1. The bimorph was excited using a sinusoidal signal from a function generator, which was amplified by a Trek® 603 series power amplifier. The gain of the amplifier is 25 with a maximum output of 250 Volts. The excitation frequency and voltage was monitored using a Tektronix® 2430A digital oscilloscope.

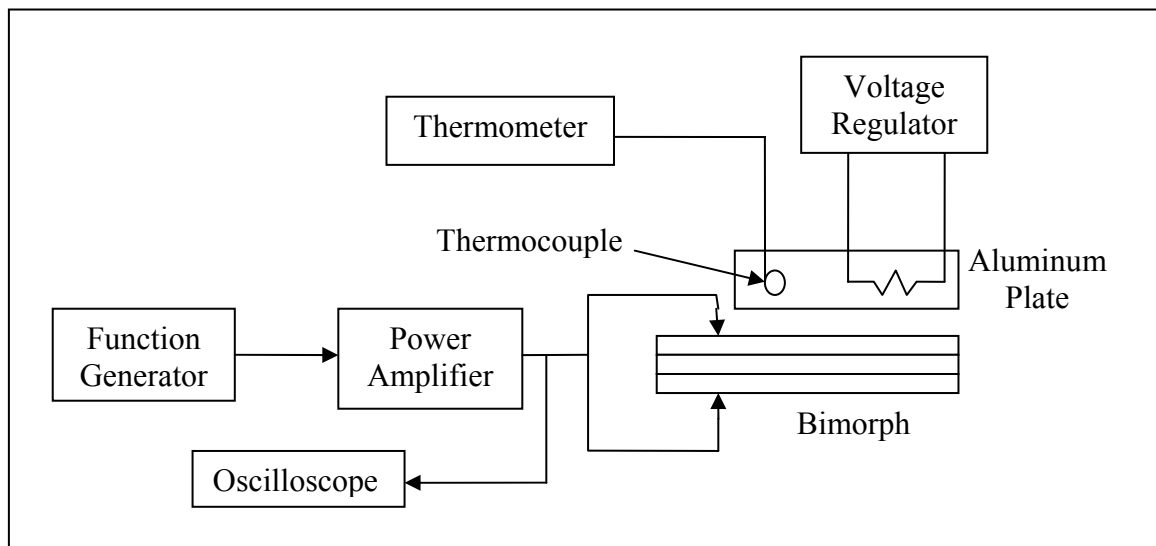


Figure 4.1: Power Resistor Cooling using Bimorph Setup

The only portion of the setup that had to be calibrated is the gap between the bimorph and the heat source. This calibration was achieved by performing a touch off using the four micrometers. The heat source was adjusted such that its entire surface was just touching the bimorph. This would ensure that the heat source was parallel to the bimorph. Contact of the heat source with the bimorph was determined visually. When light could no longer be seen between the bimorph and heat source, it was assumed that a contact has been made. The error from this calibration is considered to be +/- 50 microns. From this zeroed position the desired gap would be set.

4.1.2 Defining Optimal Gap

In order to have the bimorph provide the maximum amount of cooling, it would have to be placed at an optimal gap from the heat source. Through experimentation the optimal gap was analyzed for different vibration amplitudes of the 5H bimorph. Figure 4.2 displays the steady-state temperatures that were reached for various gaps and amplitudes with the power resistor outputting 6.05 Watts.

From figure 4.2, it can be seen that there initially appears to be an optimal gap for each of the amplitudes with the larger the amplitude, the larger the gap. The data also seems to show that the optimal gap does not necessarily have to be larger than the amplitude as seen with the 0.6mm and 0.7mm amplitudes. However, if the errors in the calibration of the gap and the errors between the theoretical and actual amplitudes are taken into account, an optimal gap of approximately 0.6mm is plausible. Another effect that could be showing up in the

above data is a transition between acoustic streaming and bulk air flow cooling. It has been shown from previous research that the optimal gap for acoustic streaming is greater than the amplitude of the vibration [41]. This would correlate with the 0.5mm and 0.4mm amplitudes. In terms of bulk air flow, the maximum amount of cooling should occur when the amplitude is at least the same as the gap which would support the results for the 0.7mm amplitude.

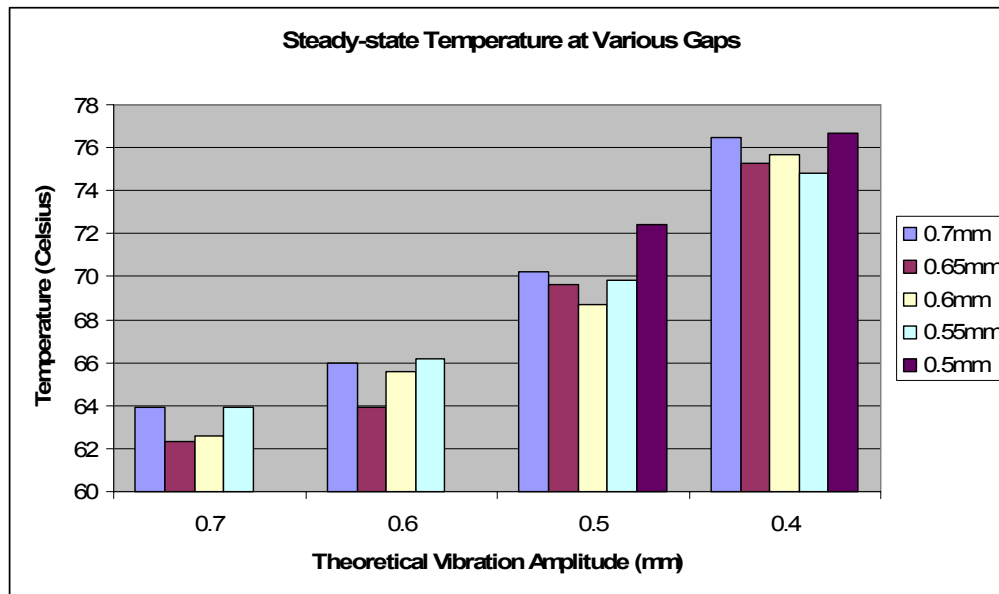


Figure 4.2: 5H Bimorph Cooling at Various Gaps and Amplitudes

B.1.3 Defining Optimal Length

According to figures 2.19 and 2.20 in Chapter 2, the volumetric flow rate of air induced by a bimorph is linearly related to the length of the bimorph with the longer the bimorph the larger the flow rate. It might be assumed that the same would be true in terms of the amount of cooling that is provided. This means that a longer bimorph would cool a heat source to a lower temperature due to the higher flow rate than a shorter bimorph. However,

experimentation does not support this conjecture. Cooling experiments were performed with several different lengths of the 5A (figure 4.3) and SS (figure 4.4) bimorphs that were excited in the second mode.

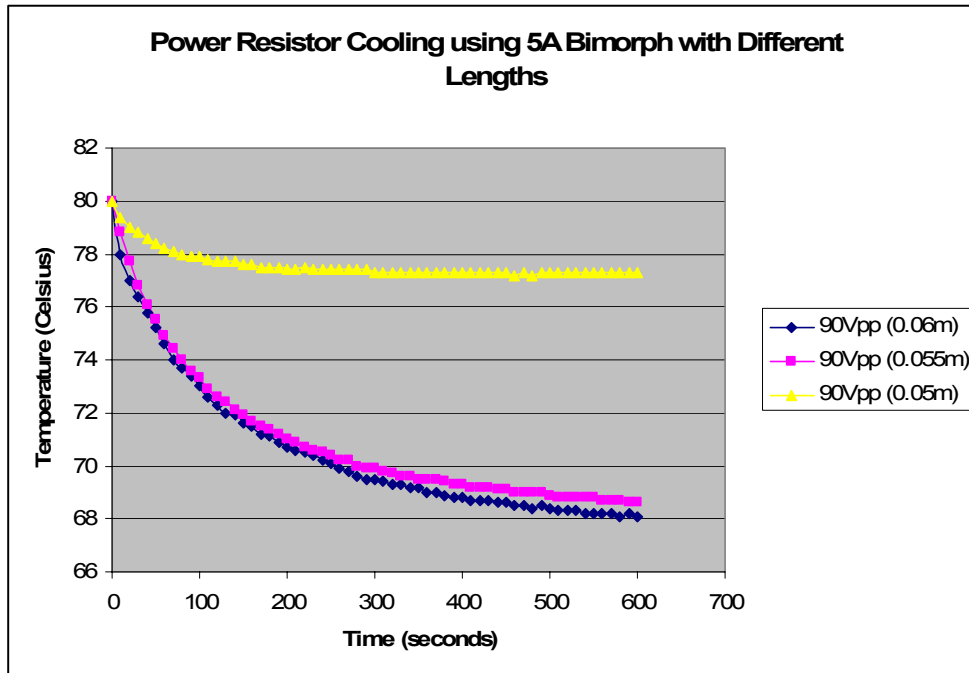


Figure 4.3: Power Resistor Cooling using 5A Bimorph

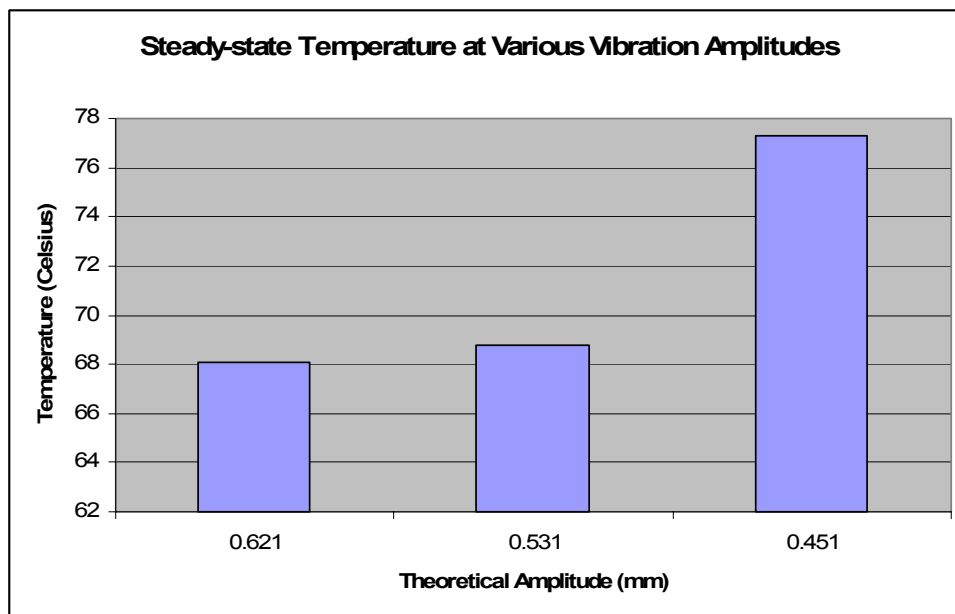


Figure 4.4: Steady-state Temperature of Power Resistor System

From figure 4.3, it can be seen that the cooling provided by the 5A bimorph is not linearly related to the length of the bimorph. In fact the 0.06m and 0.055m length bimorphs provide essentially the same cooling curve. Figure 4.3 also shows that when the length of the bimorph becomes less than 0.055m, the amount of cooling drops significantly. One possible reason for this nonlinear relationship is due to a transition between bulk air flow and acoustic streaming that was brought up in section 4.2.2. When looking at the steady-state temperature in figure 4.3 compared to the amplitude for the corresponding length in figure 4.4, it can be seen that an amplitude of approximately 0.5mm would begin the transition between bulk air flow and acoustic streaming. This is the same transition amplitude that was found from figure 4.2. The trend in figure 4.3 that is consistent with the volumetric flow rate in figure 2.19 is that when the bimorph is longer the cooling is greater. However, this trend does not show up in the testing of the SS bimorph.

Figure 4.5 displays that there exists an optimal length for the SS bimorph which is not the longest length. The optimal length is in the regime of 0.05m. Lengths longer and shorter than this provide less cooling. Unlike the 5A bimorph this can not be explained using the transition between bulk air flow and acoustic streaming. First, the 0.06m bimorph, which has the largest amplitude, has also the lowest amount of cooling. Secondly, the amplitude of each of the different length bimorphs is at least the transition amplitude of 0.5mm.

Therefore, since this transition region can not be used to explain the results, it must be assumed that the volumetric flow rate is not the only criterion which determines the amount of cooling. The next significant contributor to the cooling is most likely the velocity with which the air is flowing. From the section 2.2.5, it was shown that as a bimorph gets shorter;

it produces a higher air flow velocity due to the increase in the modal frequency. This explains why the cooling increases as the length decreases. The reason why the cooling does not continue to increase with increasing frequency is because the amplitude of the bimorph is also getting smaller. Eventually, the bimorph transitions into acoustic streaming and the bulk air flow velocity no longer has any contribution. The amplitude of the 0.05m bimorph is approx. 0.6mm with the amplitude of the 0.045m bimorph being 0.5mm, which is at the transition region.

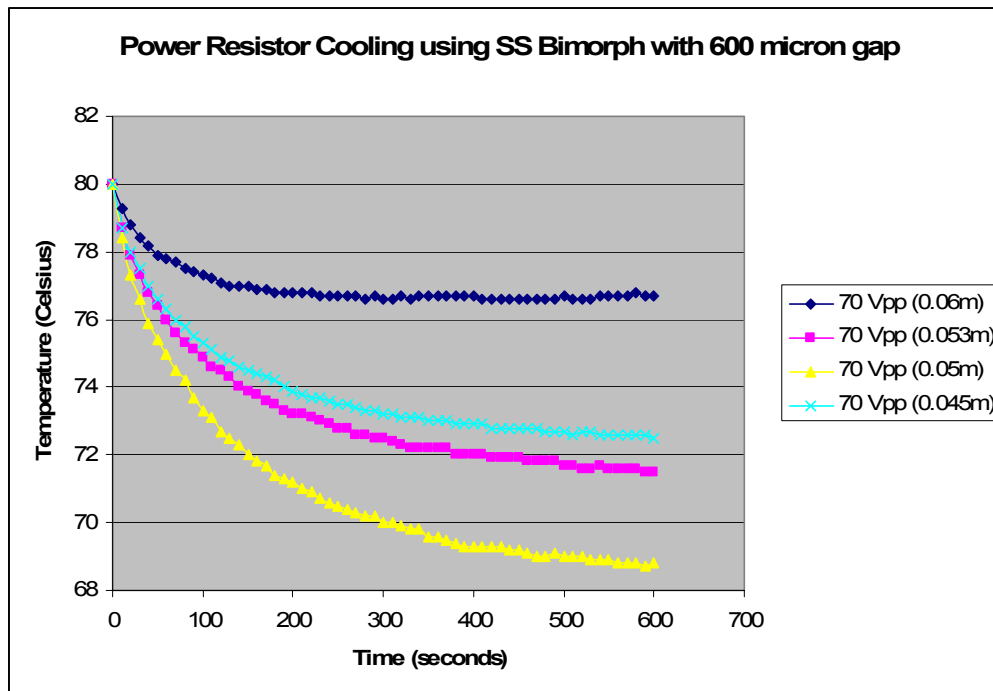


Figure 4.5: Power Resistor Cooling using SS Bimorph

4.1.4 Flow Rate Comparison

With the optimal gap and length factors taken into consideration it can be shown experimentally that the cooling provided by the bimorph is linearly related to the volumetric

flow rate being provided. Cooling tests were performed with the SS, 5H and 5A bimorphs in order to obtain the steady-state temperature with which the bimorphs could cool a 6.05W heat source. The volumetric flow rate for each test proved to be linearly related to the steady state temperature reached, as seen in figure 4.6.

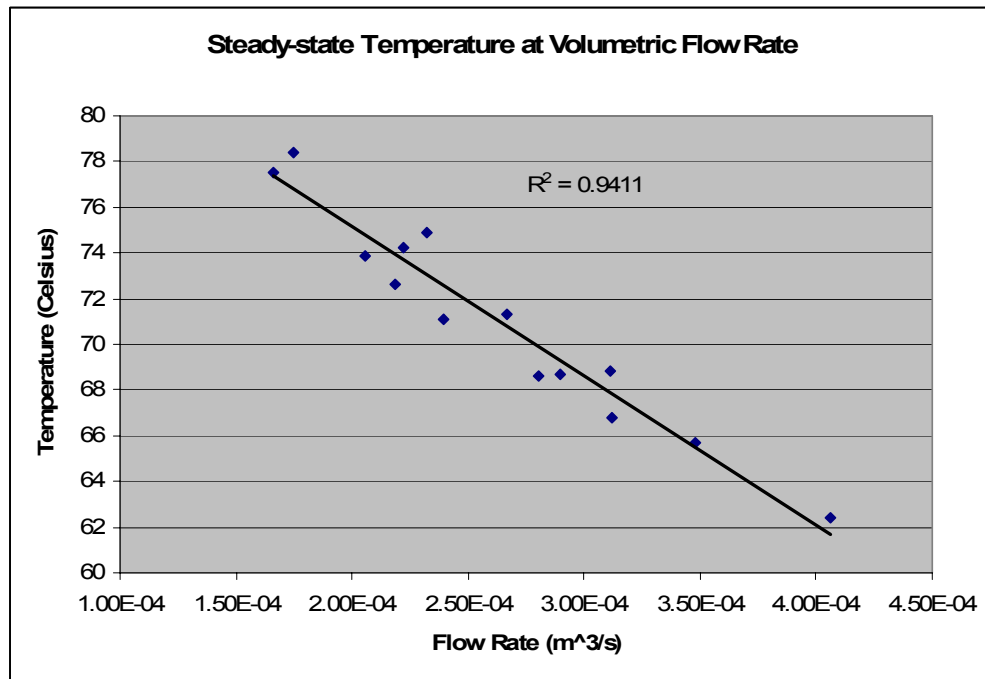


Figure 4.6: Volumetric Flow Rate vs. Steady-state Temperature

4.2 PROCESSOR COOLING EXPERIMENTS

4.2.1 Bimorph and Aluminum Plate

The same experimental setup that is listed in Chapter 3 section 2.1.1 was used for cooling experiments using a bimorph. An additional setup was manufactured such that the bimorph is situated directly above the Celeron® processor (figure 4.7). With this setup the bimorph

could be moved up and down and rotated in two axes. The setup also made the bimorph detached from the computer such that any vibrations from the bimorph would not be translated to the entire computer. These unwanted vibrations can cause the computer to operate unreliably, particularly the hard drive.

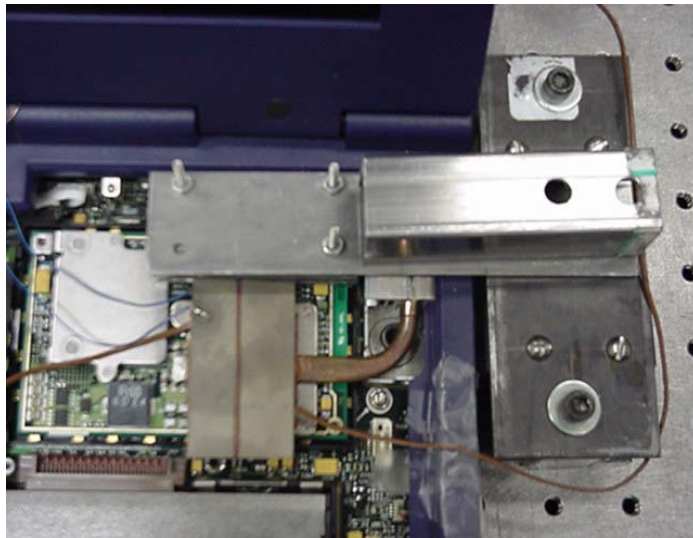


Figure 4.7: Bimorph Cooling Setup

Experiments were performed to determine whether a bimorph would be able to dissipate all of the heat emitted by the processor. This was studied by disabling the computer's cooling system. The copper contact plate from the cooling system was replaced by an aluminum plate as seen in figure 4.8. The reason that an aluminum plate was used instead of cooling the processor directly is due to physical constraints. There is not enough room for the bimorph to be lowered close enough to the processor for cooling purposes and also the two thermocouples on the processor would deter any vibrations from a bimorph.

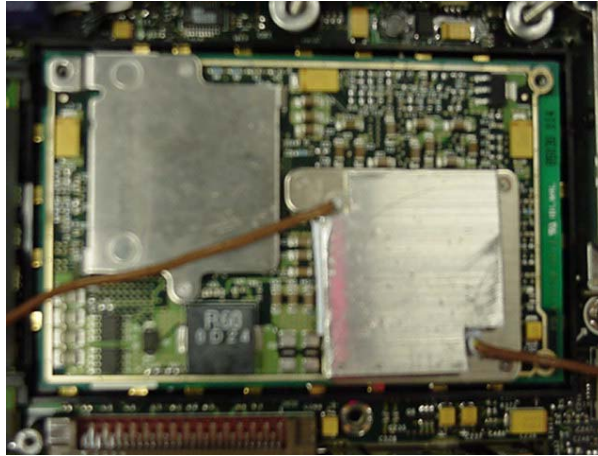


Figure 4.8: Aluminum Plate Cooling Setup

Cooling data was obtained using the 5A bimorph excited at several different excitation voltages. From the results seen in figure 4.9 it can be seen that only the highest excitation voltage could produce any cooling. Even that cooling, however, is insignificant with a drop of only 1 °C. This appears to insinuate that a bimorph alone is insufficient to cool a Celeron® processor that outputs 13W.

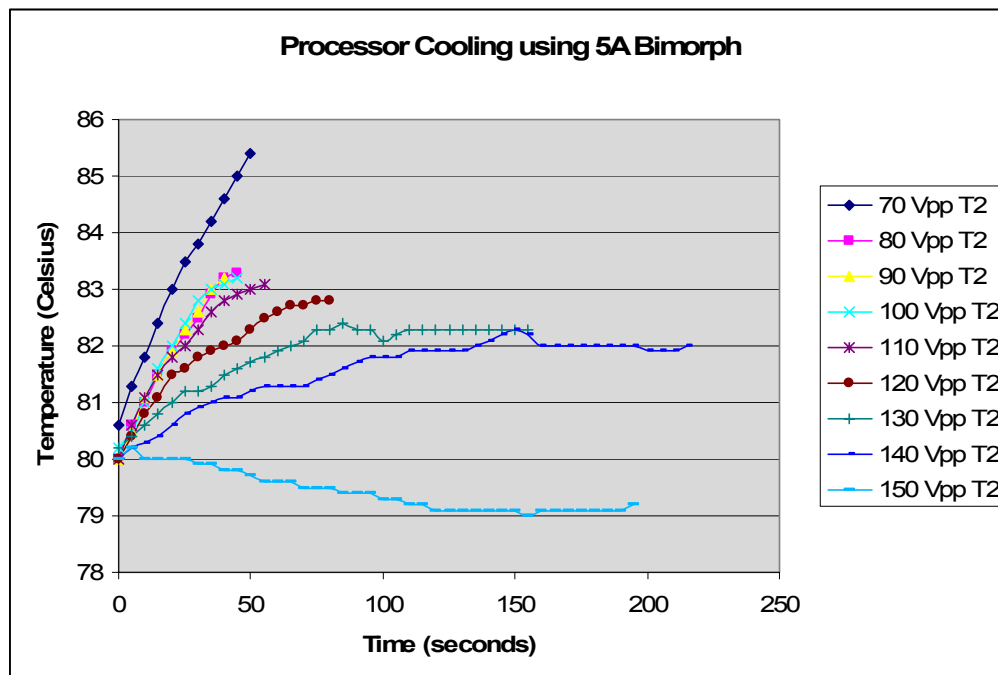


Figure 4.9: Temperature of Processor w/ 5A Bimorph and Aluminum Plate Cooling

4.2.2 Bimorph and Inspiron™ Cooling System without Fan

Since the bimorph is being studied as a possible replacement for the DC fan, experiments were performed to determine the cooling obtained when a bimorph is used in conjunction with the Inspiron™ cooling system excluding the fan. The setup would be exactly as shown in figure 4.9. The temperature data of the processor during the bimorph cooling tests can be seen in figure 4.10 along with the fan cooling data. The tests were performed with the 5A bimorph at several different excitation voltages. It is evident from the figure that the bimorph is unable to achieve the same cooling performance as the fan. Another point that can be noted is that the cooling which is achieved by the bimorph occurs at a much slower rate than with the fan.

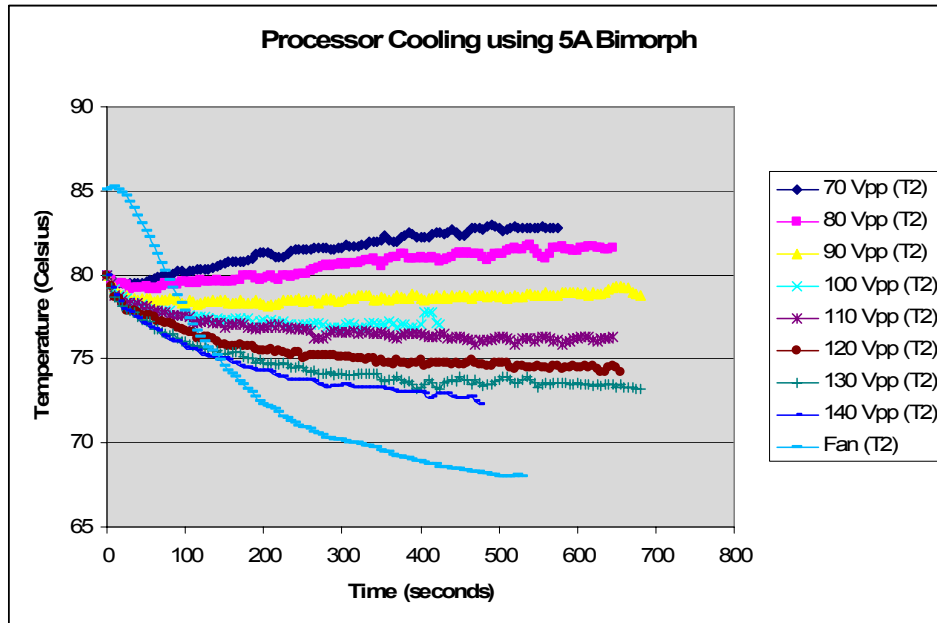


Figure 4.10: Temperature of Celeron® Processor w/ 5A Bimorph Cooling

4.3 HEAT SINK VS BIMORPH COOLING CAPABILITIES

4.3.1 Ansys® Simulation

Steady-state heat transfer analysis was performed for two different heat sinks. They are a copper folded-fin heat sink and aluminum extruded heat sink.

Copper Folded Fin Heat Sink

The first heat sink to be simulated is a copper folded-fin heat sink (figure 4.11) [48]. This heat sink is designed for the cooling of a Pentium 4® processor. The overall dimensions of the heat sink are 78x31x20mm. However, in order to reduce calculation time only a 2x2x20mm section of the heat sink was modeled (figure 4.14). The thickness of the fins was considered to be 0.25mm with the gap between the fins being 0.5mm. The heat sink was modeled with Ansys® using SOLID70 elements with a minimum element length of 0.2mm. The thermal conductivity of the copper was set to 401 W/m °C. The constraints applied to the model are a constant heat flux at the base of the heat sink and constant convection along the surface of the fins. The heat flux was set according to $\dot{q}_s = \dot{Q}/A$ where \dot{Q} is the rate of heat transfer in to the heat sink (6.05W) and A is the heat sink's base area. The convection coefficient was determined using the technique mentioned in section 2.1.2.

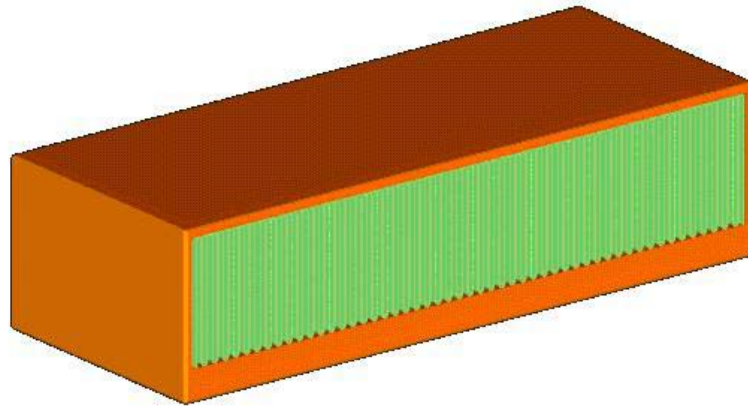


Figure 4.11: Copper Folded-Fin Heat Sink

Aluminum Extruded Heat Sink

Another heat sink that was analyzed is an aluminum extruded heat sink designed for an older Pentium® processor (figure 4.12) [49]. This heat sink, which is designed to dissipate 7-8 W, is not designed to work in conjunction with a fan. A difference between this heat sink and the previous is the type of fins. The extruded version has column fins whereas the folded-fin has vertical wall fins. The overall dimensions of the heat sink are 85x49.5x15mm. Again for ease of calculation only a 13x13x15 section was modeled with the fins being 1mm in diameter and 13mm long (figure 4.15). Due to the complexities with circular geometries the heat sink was modeled using SOLID87 elements whose size was determined based on the ‘smart size’ feature of Ansys®. The thermal conductivity of the aluminum was chosen to be 193 W/m °C. There were two constraints applied to the model, a constant heat flux along the base area and constant convection along the surface of the fins. The heat flux was chosen in

the manner as for the folded-fin heat sink (section 2.1.3). Again the convection coefficient was determined using the technique mentioned in section 2.1.2.

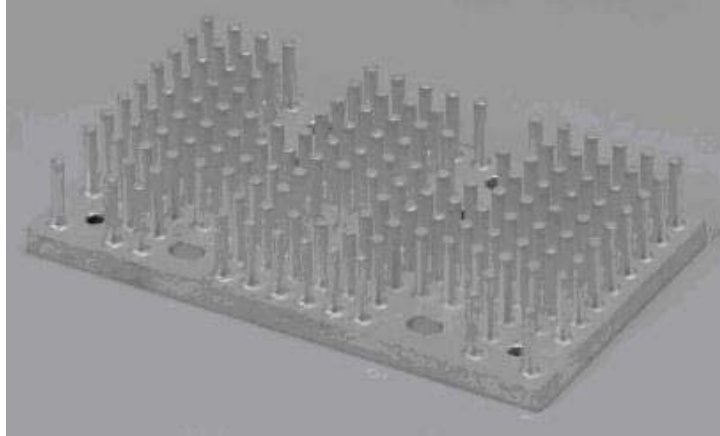


Figure 4.12: Aluminum Extruded Heat Sink

Convection Heat Transfer Coefficient and Results for Extruded and Folded-Fin Heat Sinks

It was shown previously in Chapter 2 that the convection heat transfer coefficient of a body cooling through natural convection is primarily based on the temperature of the body with the higher the temperature, the larger the coefficient. Since the Ansys® steady-state temperature of the two sinks is unknown, the convection coefficient is unknown. However, in order for Ansys® to solve for the steady-state temperature it needs to know what the convection coefficient for each heat sink is. Therefore the convection coefficient was found over a range of temperatures using equations 2.4-2.9. For these equations $\delta = 0.015\text{m}$ for the folded-fin heat sink and 0.013m for the extruded heat sink. Figure 4.13 displays the convection heat transfer coefficient for each heat sink according to the temperature of the heat sink.

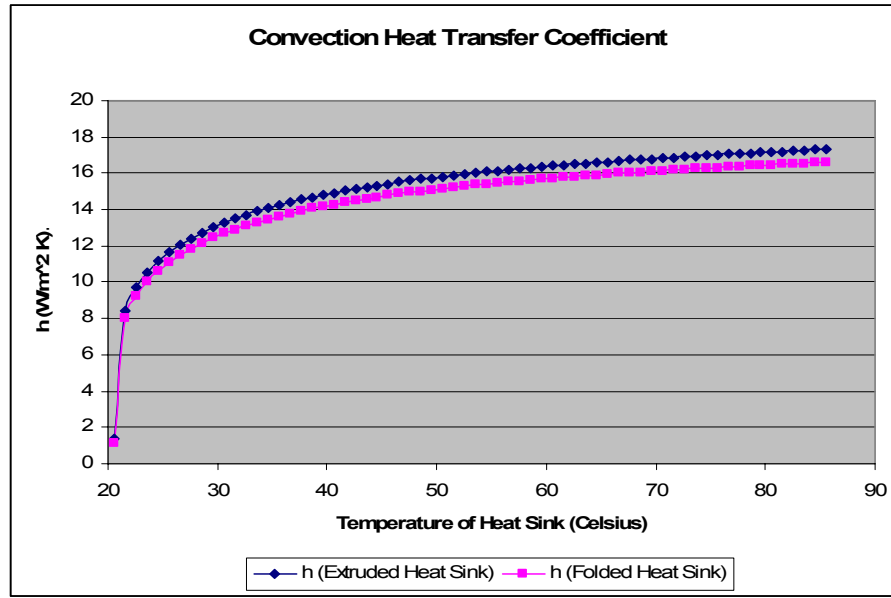


Figure 4.13: Convection Coefficient for Extruded and Folded-Fin Heat Sinks

Several steady-state analyses were performed for each heat sink; where the convection heat transfer coefficient was changed each time; until the steady-state temperature match the convection coefficient according to figure 4.13. The final steady-state temperature profile for the folded-fin and extruded heat sinks can be seen below.

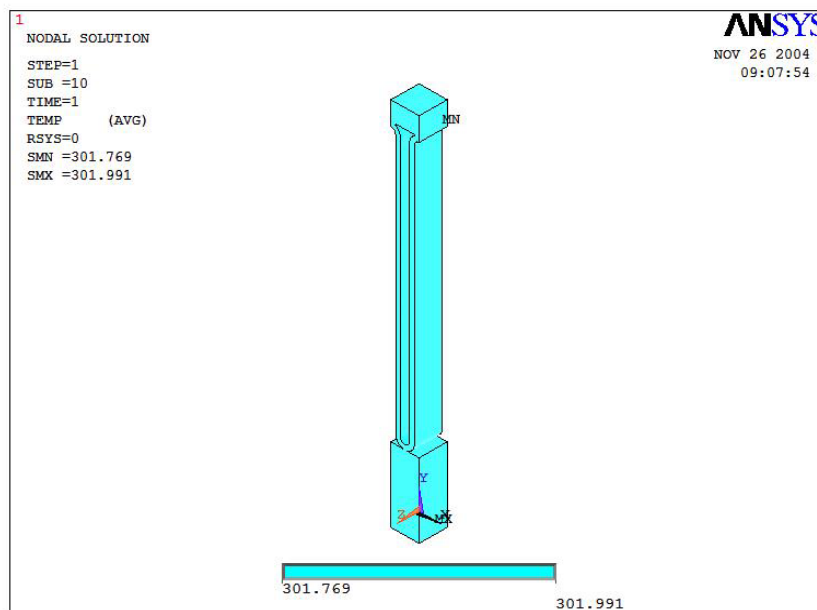


Figure 4.14: Steady-State Ansys® Analysis of Copper Folded-Fin Heat Sink

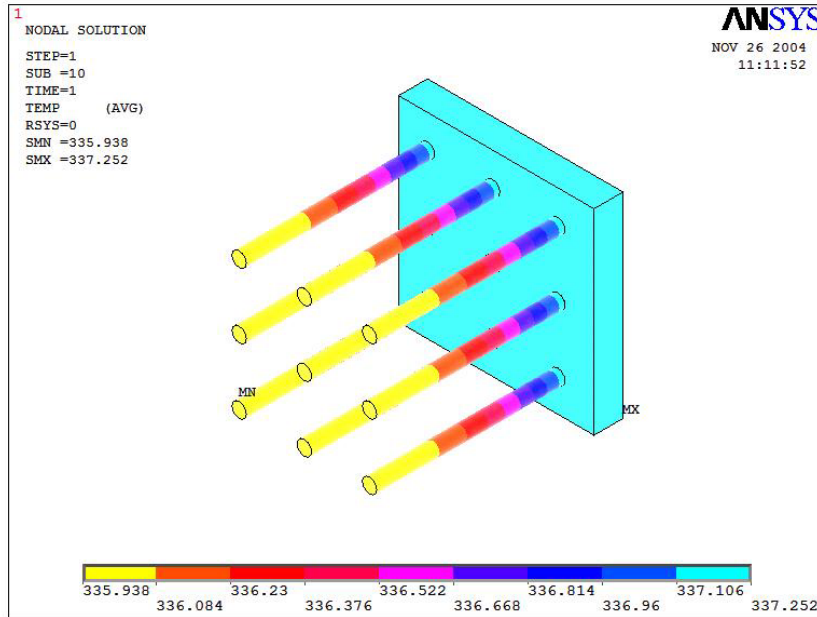


Figure 4.15: Steady-State Ansys® Analysis of Aluminum Extruded Heat Sink

4.3.2 Cooling Comparison between Heat Sink and Bimorph Results

The steady-state temperature achieved by the folded-fin heat sink, extruded heat sink and the three bimorphs when trying to dissipate 6.05 Watts of power can be seen in figure 4.16. The results for the bimorphs are in terms of the maximum cooling achieved for each bimorph according to the specified applied voltage and bimorph length. The results show that the bimorphs are not even close in achieving the cooling performance of the folded-fin heat sink, which is meant for current Pentium 4® processors. The bimorphs instead are closest to the performance of the extruded heat sink, which is meant for older Pentium® processors. From this data it can be assumed that the bimorph cannot be used as a replacement for the heat sink in cooling current high power processors.

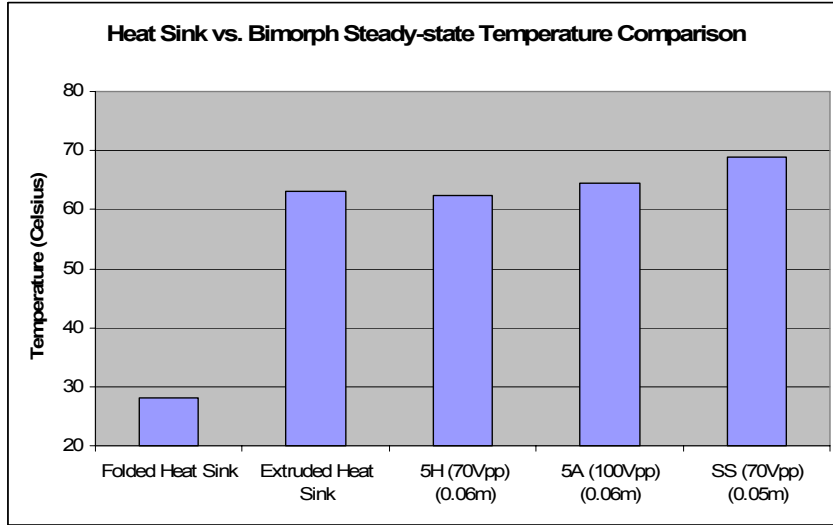


Figure 4.16: Heat Sink vs. Bimorph Steady-State Temperature Comparison

CHAPTER 5

CONCLUSION

5.1 HEAT ANALYSIS OF NOTEBOOK COMPUTER

It was found that it is possible to analyze the cooling system of a notebook computer analytically using heat transfer equations for convection and conduction. The error in this analysis is in the regime of 12%. However, if fewer assumptions are made about the system such as incorporating radiation transfer, the error should be less. It was also found that the majority of the heat dissipation occurs in the heat sink portion of the Remote Heat Exchanger. However, this dissipation does not account for all of the energy emitted by the processor. Therefore, other methods for cooling a notebook computer are just as essential as the main cooling system itself such as a stamped plate on the bottom of the keyboard.

While a cooling system can be represented analytically with some accuracy, the temperature profile of the processor cannot. Two methods for predicting the profile were used. The first method, which utilized least squares fitting, showed a temperature profile can be accurately written as the combination of a logarithmic and decaying exponential function. However, a logarithmic function cannot predict steady-state temperature. The Conservation of Energy was also shown to be not suitable to predict a temperature profile. While it can predict a simple system with conduction or convection heat transfer, a notebook computer system is too complex to be handled with this method.

5.2 COOLING CAPABILITIES OF PIEZOELECTRIC BIMORPH

It was found that the cooling capabilities of a bimorph are dependent not only on the volumetric flow rate produced, but also the flow velocity. The flow rates that are induced by a bimorph increase linearly with increasing bimorph length. While the flow velocity produced is proportional to the bimorphs modal frequency. Meaning as the bimorph length decreases the flow velocity increases. Due to this opposing effect an optimal length that will produce the most cooling can be found for a specific bimorph. A transition region was found between acoustic streaming and bulk air flow when the bimorph amplitude is around 0.5mm. Moving into the bulk air flow regime improves convective heat transfer past the limits of acoustic streaming. When acoustic streaming is in effect, there exists a gap where maximum cooling is present, which is greater than the vibration amplitude of the bimorph. For bulk air flow, the optimal gap is obtained when the amplitude is exactly the same as the gap.

In the end it was shown that a bimorph is unable to achieve the cooling requirements of current mobile processors, which require around 70W of heat to be dissipated. Instead it was shown that a bimorph is comparable to a heat sink which is designed to dissipate 7-8 Watts. While a bimorph is not applicable for high power devices, it could be for lower power devices such as personal handheld devices and cellular phones.

5.3 FUTURE WORK

Work that should be completed in the future pertains to the last statement. The applicability for using a bimorph to cool low power devices should be analyzed. A major hurdle to be overcome would be the power requirements needed to actuate a bimorph. Another area that should be addressed is the transition region between acoustic streaming and bulk air flow. This region should be better defined such that optimization for bimorph cooling can be obtained. Other research areas that affect this optimization include optimal flow rates and flow velocities. It is conceivable that when the cooling capabilities of a bimorph are being assessed the optimal volumetric flow rate and flow velocity that will produce the maximum cooling can be predetermined without having to perform experimentation.

REFERENCES

- [1] MobileMag 2004 NEC Develops Water Cooling Notebook Module
<http://www.mobilemag.com/content/100/334/C1811/>
- [2] Suzuki M and Hirano M 1998 Fan-less Cooling Technology for Notebook Computers
Fujitsu Sci. Tech. J. **34** 1.
- [3] Intel 2004 Mobile Intel Pentium 4 Processors – M Thermal Management
<http://support.intel.com/support/processors/mobile/pentium4/sb/CS-007489.htm>
- [4] Laptop Service King 2004 Internal Laptop Fans Hesperia, CA
<http://www.laptopking.com/kingfanlist.asp>
- [5] Digit-Life.com 2004 Cooling Systems. Part 1: Processor Coolers <http://www.digit-life.com/articles2/cpucoolersinquestion/cpu-coolers-inquestion-august2k2.html>
- [6] ERM Thermal Technologies Inc. 2004 Extruded Heatsinks Ontario, NY
<http://www.extrudedheatsink.com/index.html>
- [7] Aavid Thermalloy, LLC 2004 Folded Fin Assemblies Concord, NH
<http://www.aavidthermalloy.com/products/foldedfin/index.shtml>
- [8] Cheresources, Inc. 2002 What is a Heat Pipe? Midlothian, VA
<http://www.cheresources.com/htpipes.html>
- [9] Garner S D 1996 Heat Pipes for Electronics Cooling Applications
http://www.electronics-cooling.com/Resources/EC_Articles/SEP96/sep96_02.htm
- [10] Riley N 2001 Acoustic Streaming *Annual Rev. Fluid Mech.* **33** 34-65.

- [11] Hamilton M F, Ilinskii Y A and Zabolotskaya E A 2003 Acoustic Streaming Generated by Standing Waves in Two-Dimensional Channels of Arbitrary Width *J. Acoustic Soc. Am.* **113(1)** 153-160.
- [12] Wan Q and Kuznetsov A V 2003 Effect of Non-uniformity of Source Vibration Amplitude on the Sound Field Wave Number, Attenuation Coefficient and Reynolds Stress for the Acoustic Streaming *Int. Comm. Heat Mass Transfer* **30(1)** 27-36.
- [13] Lighthill A J 1978 Acoustic Streaming *Journal of Sound and Vibration* **61(3)** 391-418.
- [14] Nyborg W L 1965 Acoustic Streaming *Physics Acoustics IIB* New York 265-331.
- [15] Nyborg W L 1998 Acoustic Streaming *Nonlinear Acoustics* San Diego, CA 207-231.
- [16] Nyborg W L 1958 Acoustic Streaming near a Boundary *J. Acoustic Soc. Am.* **30(4)** 329-339.
- [17] Mitome H 1998 The Mechanism of Generation of Acoustic Streaming Electronics and Communications in Japan **81(10)** 1-8.
- [18] Nguyen N T and White R M 2000 Acoustic Streaming in Micromachined Flexural Plate Wave Devices: Numerical Simulation and Experimental Verification *IEEE Transactions on Ultrasonics, Ferroelectrics and Frequency Control* **47(6)** 1463-1471.
- [19] Bailliet H, Gusev V, Raspet R and Hiller R A 2001 Acoustic Streaming in Closed Thermoacoustic Devices *J. Acoustic Soc. Am.* **110(4)** 1808-1821.
- [20] Haydock D and Yeomans J M 2003 Lattice Boltzmann Simulations of Attenuation-Driven Acoustic Streaming *Journal of Physics A: Mathematical and General* **36** 5683-5694.

- [21] Lee C P and Wang T G 1990 Outer Acoustic Streaming *J. Acoustic Soc. Am.* **88(5)** 2367-2375.
- [22] Andres J M and Ingard U 1953 Acoustic Streaming at High Reynolds Numbers *J. Acoust. Soc. Am.* **25(5)** 928-932.
- [23] Andres J M and Ingard U 1953 Acoustic Streaming at Low Reynolds Numbers *J. Acoust. Soc. Am.* **25(5)** 932-938.
- [24] Akay A and Xu Z 1998 Experiments on Acoustic Streaming in a Fluid Layer between Vibrating Surfaces and Amplitude-dependent Damping of Vibrations *J. Acoust. Soc. Am.* **103(2)** 865-871.
- [25] Campbell M, Cosgrove J A, Greated C A, Jack S and Rickliff D 2000 Review of LDA and PIV Applied to the Measurement of Sound and Acoustic Streaming *Optics & Laser Technology* **32** 629-639.
- [26] Jackson F J 1960 Sonically Induced Microstreaming near a Plane Boundary. II. Acoustic Streaming Field *J. Acoustic Soc. Am.* **32(11)** 1387-1395.
- [27] Rayleigh L 1883 On the Circulation of Air Observed in Kundt's Tubes and Some Allied Acoustic Problems *Philos. Trans. R. Soc. London Ser. A* **175** 1-21.
- [28] Riley N 1998 Acoustic Streaming *Theoret. Comput. Fluid Dynamics* **10** 349-356.
- [29] Loh B G, Hyun S, Ro P I and Kleinstreuer C 2002 Acoustic Streaming Induced by Ultrasonic Flexural Vibrations and Associated Enhancement of Convective Heat Transfer *J. Acoustic Soc. Am.* **111(2)** 875-883.
- [30] Rife J C, Bell M I, Horwitz J S, Kabler M N, Auyeung R C Y and Kim W J 2000 Miniature Valveless Ultrasonic Pumps and Mixers *Sensors and Actuators* **86** 135-140.

- [31] Gould R K 1966 Heat Transfer across a Solid-Liquid Interface in the Presence of Acoustic Streaming *J. Acoustic Soc. Am.* **40(1)** 219-225.
- [32] Gopinath A and Mills A F 1993 Convective Heat Transfer from a Sphere Due to Acoustic Streaming *ASME J. Heat Transfer* **115** 332-341.
- [33] Gopinath A and Mills A F 1994 Convective Heat Transfer due to Acoustic Streaming across the Ends of a Kundt Tube *ASME J. Heat Transfer* **116** 47-53.
- [34] Vainshtein P, Fichman M and Gutfinder C 1995 Acoustic Enhancement of Heat Transfer between Two Parallel Plates *Int. J. Heat Mass Transfer* **38(10)** 1893-1899.
- [35] Mozurkewich G 1995 Heat Transfer from a Cylinder in an Acoustic Standing Wave *J. Acoustic Soc. Am.* **98** 2209-2216.
- [36] Mozurkewich G 2002 Heat Transport by Acoustic Streaming within a Cylindrical Resonator *Applied Acoustics* **63** 713-735.
- [37] Richardson P D 1967 Heat Transfer from a Circular Cylinder by Acoustic Streaming *J. Fluid Mechanics* **30** 337-355.
- [38] Davidson B J 1973 Heat Transfer from a Vibrating Circular Cylinder *Int. J. Heat Mass Transfer* **16** 1703-1727.
- [39] Ro P I and Loh B G 2001 Feasibility of using flexural waves as a cooling mechanism *IEEE Trans. Ind. Electron.* **48** 142-9.
- [40] Wu T 2004 Modeling and Design of a Novel Cooling Device for Microelectronics using Piezoelectric Resonating Beams *PHD Thesis* North Carolina State University.
- [41] Wu T, Ro P I, Kingon A I, and Mulling J F 2003 Piezoelectric resonating structures for microelectronic cooling *Smart Mater. Struct.* **12** 181-187.

- [42] Intel®. 2004 *Mobile Intel® Celeron® Processor on .13 Micron Process and in Micro-FCPGA Package Datasheet*, <http://www.intel.com/>
- [43] Patterson D A and Hennessy J L 1998 *Computer Organization & Design: The Hardware/Software Interface* (San Francisco, CA: Morgan Kaufmann Publishers, Inc.) 14-28.
- [44] Çengel Y A and Turner R H 2001 *Fundamental of Thermal-Fluid Sciences* (New York: McGraw Hill) 604-814.
- [45] Piezo Systems, Inc. 2004 Catalog #5 Cambridge, MA <http://www.piezo.com>
- [46] Wang Q M and Cross L E 1998 Performance analysis of piezoelectric cantilever bending actuators *Ferroelectrics* **215** 187-213.
- [47] Wu T and Ro P I 2003 Dynamic peak amplitude analysis and bonding layer effects of piezoelectric bimorph cantilevers *Smart Mater. Struct.* **13** 203-210.
- [48] Novel Concepts, Inc. 2004 *Microelectronic Thermal Management* Las Vegas, NV <http://www.novelconceptsinc.com/heat-sinks.htm>
- [49] PFU A Fujitsu Company 2004 *Technology & Reliability* <http://www.pfu.fujitsu.com/en/prodes/product/cardpc/pd2200/option.html>